2009

# Integration of a magnetic bias field coil in a plasmoid thruster

Kjell-Edmund Ims

# INTEGRATION OF A MAGNETIC BIAS FIELD COIL IN A PLASMOID THRUSTER

by

KJELL-EDMUND IMS

A THESIS

Submitted in partial fulfillment of the requirements
for the degree of Master of Science in Engineering
in
The Department of Mechanical and Aerospace Engineering
to
The School of Graduate Studies
of
The University of Alabama in Huntsville

HUNTSVILLE, ALABAMA

2009

In presenting this thesis in partial fulfillment of the requirements for a master's degree from The University of Alabama in Huntsville, I agree that the Library of this University shall make it freely available for inspection. I further agree that permission for extensive copying for scholarly purposes may be granted by my advisor or, in his/her absence, by the Chair of the Department or the Dean of the School of Graduate Studies. It is also understood that due recognition shall be given to me and to The University of Alabama in Huntsville in any scholarly use which may be made of any material in this thesis.

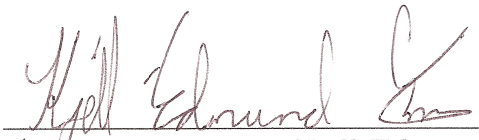

(student signature: Kjell-Edmund Ims)

12-12-2008

(date)

## THESIS APPROVAL FORM

Submitted by Kjell-Edmund Ims in partial fulfillment of the requirements for the degree of Master of Science in Engineering in Aerospace Engineering and accepted on behalf of the Faculty of the School of Graduate Studies by the thesis committee.

We, the undersigned members of the Graduate Faculty of The University of Alabama in Huntsville, certify that we have advised and/or supervised the candidate of the work described in this thesis. We further certify that we have reviewed the thesis manuscript and approve it in partial fulfillment of the requirements for the degree of Master of Science in Engineering in Aerospace Engineering.

Jason T Cassibry 12/12/08 Committee Chair
*Dr. Jason T. Cassibry* (Date)

Georgia A Richardson 12-12-08
*Dr. Georgia A. Richardson* (Date)

Adam K. Martin 12/12/08
*Dr. Adam K. Martin* (Date)

Kader Frendi 12/22/08 Department Chair
*Dr. Kader Frendi* (Date)

Phillip A Farrington 1/13/09 College Dean
*Dr. Phillip A. Farrington* (Date)

Debra M. Moriarity 3/11/09 Graduate Dean
*Dr. Debra M. Moriarity* (Date)

## ABSTRACT

School of Graduate Studies
The University of Alabama in Huntsville

Degree Master of Science in Engineering College/Dept. Engineering/Mechanical and Aerospace Engineering

Name of Candidate Kjell-Edmund Ims

Title Integration of a Magnetic Bias Field Coil in a Plasmoid Thruster

The Plasmoid Thruster Experiment (PTX) is a pulsed inductive thruster design using a conical theta pinch coil to form and accelerate plasmoids. Magnetized or Compact Toroid (CT) plasmoids have closed magnetic field structures making them naturally detached from the nozzle of a space craft as well as making them candidates for fusion fueling and confinement. In order to optimize usage of plasmoids, it is important to study the formation processes.

In this study, a method for integrating a magnetic bias field with PTX was investigated. With a magnetic bias field in place at the time of ionization of the plasma propellant, the propellant would ionize on the field lines, "freezing" the field lines into the weakly ionized gas. At that point, the main capacitor bank would be discharged into the conical theta pinch coil and the rapidly increasing main magnetic field would compress and heat the ionized gas into a fully ionized plasma. As the ringing capacitor discharge changes direction, the field would rapidly reverse, forcing the frozen field lines in the plasma to tear, either controlled at the locations of x-points, or uncontrolled (resistive tearing) and reconnect with the bias field, forming a plasmoid with a self-contained field. It would then be accelerated away from the coil by the Lorentz ($\mathbf{J} \times \mathbf{B}$) force. The purpose of adding an external magnetic bias

field is to increase the trapped magnetic flux in order to study how this would affect the formation process and final quality of the formed plasmoids.

There are various designs that could be attempted in order to produce the magnetic bias field. The main design studied herein puts the bias field coil directly underneath the main coil using loosely wrapped wires to form the bias coil. Through Finite Element Analysis (FEA) and troubleshooting of the experimental setup, it was determined that such a design interferes with the main field to the point where any plasmoid formation becomes very difficult. Additionally, the bias coil wires are so close to the magnetic probes used to characterize formed plasmoids that interpreting the probe data becomes non-trivial due to the sharp magnetic field gradients close to the probes. The gradients stem from interaction between the main coil field, the bias coil field and the material conductivity of the bias wires.

A preliminary study of an alternate magnetic bias design was carried out in which the problems with plasmoid formation and probe interference have been solved at the expense of a much weaker bias field.

Abstract Approval: Committee Chair _____
*Dr. Jason T. Cassibry*

Department Chair _____
*Dr. Kader Frendi*

Graduate Dean _____
*Dr. Debra M. Moriarity*

## ACKNOWLEDGMENTS

In any great undertaking there are always a multitude of people who directly or indirectly influence the outcome and so too is it with this thesis. The process has been a long and arduous one, and I am afraid that even as I try to list every individual and organization that has in some way helped or contributed to the effort, the list will probably be incomplete in some way. Therefore I would like to apologize in advance to any individual or group that feels like they were left out, and extend my most sincere thanks to all who helped or assisted in some way. With that said, I would like to extend a special thanks to the following people, without whom I would not have been able to complete my thesis in a timely manner.

First and foremost, my gratitude and thanks goes to my academic advisor and friend, Jason Cassibry, who supported me academically, financially (through the GRA and GTA programs) and personally. His great tutelage, enthusiasm and professional demeanor was invaluable to me during this work.

Next, Coby McColgin, my fellow graduate student and lab-partner whose high spirits and eagerness to help out with the many little things required setting up, trouble-shooting, fixing and running the experiment, for his assistance and initiative in the uncertainty analysis and numerous other tasks he did to help move the experiment along.

Also, a big "Thank You" to Peter Fimognari for his help and input both in the design, troubleshooting and writing phases of this work. His prompt replies to e-mails

and phone calls were always very much appreciated. He aided me in understanding much of the data analysis tools as well as training me on the operation and theory of the experiment.

Of great support to me during the most trying of times, I owe my deepest gratitude to Branwen, who was always supportive and who I could count on when work required me to spend long hours in the lab; you will always hold a special place in my heart. Also my family, my parents and my brother, for their selfless support of my initiative to leave my home country and seek out a degree and a career half-way across the world. Your understanding and support was crucial and I know I would have faltered long before the finish line without it.

In addition, my thanks go out to the rest of my advisors, Adam Martin at the Marshall Space Flight Center for his unsurpassed expertise on the original PTX setup and diagnostics, and Georgia Richardson for her support in the later stages of this effort.

Furthermore, my thanks go out to Jeff Richeson for the numerous circuit board layouts he milled out (and designed), Bill Accolla for his support with the Acqiris Digitizer equipment, and Jim Slemp of PWG for his generosity and trust in allowing us access to his company's resources for calibration and LabVIEW expertise. I would also like to give my thanks to Vladimir Padnov with Tera Analysis and QuickField™ for his help with the finite element modeling efforts and for providing us with 2 weeks of free use of their professional license. Also, my gratitude to the staff at the Propulsion Research Center and at the Mechanical and Aerospace Department for their help with purchases, documents and forms. Last but certainly not least, Mr. Tony Hall for his

un-wavering support in the day to day running, maintenance, fixing and wrenching in the lab as well as his expertise in vacuum systems.

## TABLE OF CONTENTS

**List of Figures** **xiii**

**List of Tables** **xvi**

**Chapter**

**1 Introduction** **1**

1.1 Electric Propulsion . . . . . 3

1.1.1 Electrothermal . . . . . 5

1.1.2 Electrostatic . . . . . 7

1.1.3 Electromagnetic . . . . . 7

1.2 Pulsed Inductive Propulsion . . . . . 8

1.3 Outline . . . . . 10

**2 Experimental Background** **11**

2.1 Overview . . . . . 11

2.2 Previous Plasmoid Thruster Research . . . . . 12

2.3 Theoretical Background . . . . . 14

**3 Experimental Setup** **19**

3.1 Overview . . . . . 19

3.2 Main Coil System . . . . . 20

3.2.1 Conical Theta Pinch Coil . . . . . 21
3.2.2 Main Capacitor Bank . . . . . 21
3.2.3 Main Spark Gap Switch . . . . . 24
3.2.4 Main Capacitor Power Supply . . . . . 25
3.2.5 Pre-Ionizer System . . . . . 26
3.3 Bias Field System . . . . . 28
3.3.1 Bias Field Coil . . . . . 29
3.3.2 Bias Capacitor Bank . . . . . 31
3.3.3 Bias Silicon-Controlled Rectifier Switch . . . . . 33
3.3.4 Bias Capacitor Power Supply . . . . . 34
3.4 Propellant Feed Sub-System . . . . . 35
3.4.1 Pressure Regulator . . . . . 35
3.4.2 Fill Valve . . . . . 37
3.4.3 Puff Valve . . . . . 38
3.4.4 Vacuum Chamber . . . . . 39
3.5 Control System . . . . . 42
3.5.1 Computer for Operation of Software Controlled Systems . . . 43
3.5.2 National Instruments FieldPoint System . . . . . 44
3.5.3 Berkeley Nucleonics Pulse Delay Generator . . . . . 44
3.5.4 Bias Coil Control . . . . . 46
3.5.5 Interlock & Safety Systems . . . . . 50
3.5.6 Fast Optical (Timing) Control System . . . . . 52
3.5.7 Slow Optical Control System . . . . . 52

3.6 Data Acquisition System . . . . . 53
3.6.1 Acqiris High Speed Digitizer System . . . . . 53
3.6.2 Computer for Data Retrieval and Archiving . . . . . 54
3.6.3 Oscilloscope . . . . . 55
3.6.4 FieldPoint Slow Analog Input . . . . . 55
3.7 Diagnostic System . . . . . 56
3.7.1 The Interferometry System . . . . . 56
3.7.1.1 Extracting the Sine and Cosine of the Phase Mixed Signal . . . . . 67
3.7.1.2 Converting from Phase-change to Density . . . . . 70
3.7.2 Bias System Pearson Probe . . . . . 77
3.7.3 Bias System Voltage Divider Probe . . . . . 80
3.7.4 Propellant Reservoir (Plenum) Pressure Sensor . . . . . 80
3.7.5 $\dot{\mathbf{B}}$ Probes . . . . . 81
3.7.6 Φ-loop Probes . . . . . 83
3.8 Chamber Volume and Plenum Volume Calibration . . . . . 83
3.8.1 Chamber Volume . . . . . 84
3.8.2 Plenum Volume . . . . . 87

**4 Results and Analysis** **94**

4.1 Overview . . . . . 94
4.2 Troubleshooting . . . . . 95
4.3 QuickField™ Transient Analysis . . . . . 98

4.4 Effects of the Main-to-bias Coupling on Diagnostic and Periphery Systems . . . . . 119

4.5 Possible Future Improvements . . . . . 120

**5 Conclusions** **129**

5.1 Overview . . . . . 129

5.2 Conclusions . . . . . 129

5.3 Future Work . . . . . 131

**APPENDIX A: Tables of data** **134**

**APPENDIX B: Figures and graphs** **146**

**REFERENCES** **149**

## LIST OF FIGURES

FIGURE PAGE


2.1 Conceptual FRC formation process with the presence of a magnetic bias field . . . . . 17

2.2 Final stage of conceptual FRC formation process with the presence of a magnetic bias field. . . . . 18

3.1 Top down view of the main coil . . . . . 22

3.2 Photograph of the main coil . . . . . 22

3.3 Main capacitor bank enclosure, seen from the side. . . . . 24

3.4 Automatic safety discharge profile . . . . . 32

3.5 The SCR device sandwiched between two aluminum plates. . . . . 33

3.6 The propellant feed system . . . . . 36

3.7 Close up of the pressure regulator, here with Nitrogen. . . . . 37

3.8 The main vacuum enclosures. . . . . 40

3.9 The roughing pump. . . . . 40

3.10 The turbo pump. . . . . 41

3.11 The NI-FP system. . . . . 45

3.12 The PDG and custom optical converter box. . . . . 46

3.13 SCR trigger and switching circuit. . . . . 47

3.14 Relay timing and bounce profile . . . . . 48

3.15 Bias current discharge profile . . . . . 50

3.16 Emergency and interlock boxes. . . . . 51

3.17 Sample of fiber optical cables. . . . . 52

3.18 The original Mach-Zehnder interferometer setup . . . . . 58

3.19 Overview of a sample AOM . . . . . 59

3.20 Interferometry path lengths with color overlays . . . . . 66

3.21 Interferometry density profiles as a function of delay times, taken from [1] 77

3.22 Pearson probe used to measure the bias system current . . . . . 78

3.23 Saturated Pearson current probe signal . . . . . 79

3.24 Closeup of fine gauge $\dot{\mathbf{B}}$ probe wire . . . . . 83

3.25 Plenum pressure calibration curve . . . . . 88

3.26 Hydrogen plenum volume curve . . . . . 89

3.27 Argon plenum volume curve . . . . . 90

3.28 Nitrogen plenum volume curve . . . . . 91

4.1 Overview of the QuickField™ model used . . . . . 99

4.2 Closeup view of QuickField™ model of PTX near the coils. . . . . 100

4.3 Magnetostatic results with a static bias and main coil current . . . . 103

4.4 Magnetostatic results with a static bias coil current . . . . . 104

4.5 Transient results with a static bias coil current . . . . . 105

4.6 Transient results of the main coil at the first peak at $1\,\mu$s . . . . . 107

4.7 Transient results of the main coil at the first zero crossing at $2\,\mu$s . . 108

4.8 Transient results of the main coil at the first negative peak at $3\,\mu$s . . 109

4.9 Transient results of the main coil at the second zero crossing at $4\,\mu$s . 110

4.10 Extreme close-up of the collapsing fields at 4 $\mu$s . . . . . 110

4.11 Transient analysis of both coils, 1 $\mu$s . . . . . 112

4.12 Transient analysis of both coils, 2 $\mu$s . . . . . 112

4.13 Transient analysis of both coils, 3 $\mu$s . . . . . 113

4.14 Transient analysis of both coils, second zero crossing of the main coil at 4 $\mu$s. . . . . 113

4.15 Transient analysis of both coils, second maxima of the main coil at 5 $\mu$s 114

4.16 Transient analysis of both coils for 750 A bias current at 0 $\mu$s . . . . . 115

4.17 Transient analysis with a bias current of 750 A at the first main coil maxima at 1 $\mu$s . . . . . 116

4.18 Transient analysis with a bias current of 750 A at the first zero crossing at 2 $\mu$s . . . . . 116

4.19 Transient analysis with a bias current of 750 A at the first main coil minima at 3 $\mu$s . . . . . 117

4.20 Analysis of a scenario with only the main coil present . . . . . 118

4.21 Simulation of proposed pulsed external bias field: DC with only the bias coils . . . . . 124

4.22 Simulation of proposed pulsed external bias field at 200 $\mu$s with only the bias coils . . . . . 125

4.23 Simulation of proposed pulsed external bias field at 1 $\mu$s with all coils 126

4.24 Simulation of proposed pulsed external bias field at 2 $\mu$s with all coils 127

4.25 Simulation of proposed pulsed external bias field at 3 $\mu$s with all coils 128

B.1 Simulation of proposed pulsed, external bias field setup: DC with only the main coil active . . . . . 147

B.2 A photograph of a plasma shot using Argon propellant . . . . . 148

## LIST OF TABLES

TABLE PAGE

3.1 Results of the overall system resistance as determined using Ohm's Law and experimental data [1]. . . . . 31

3.2 Results of the chamber volume data reduction . . . . . 86

A.1 $\dot{\mathbf{B}}$ calibration data . . . . . 135

A.2 Data set 1 from 21 Nov 2007 . . . . . 136

A.3 Constants and correction factors for data set 1 from 21 Nov 2007 . . 137

A.4 Data set 2 from 21 Nov 2007 . . . . . 138

A.5 Constants and correction factors for data set 2 from 21 Nov 2007 . . 139

A.6 Data set 1 from 23 Nov 2007 . . . . . 140

A.7 Constants and correction factors for data set 1 from 23 Nov 2007 . . 141

A.8 Data set 1 from 26 Nov 2007 . . . . . 142

A.9 Constants and correction factors for data set 1 from 26 Nov 2007 . . 143

A.10 Data set 2 from 26 Nov 2007 . . . . . 144

A.11 Constants and correction factors for data set 2 from 26 Nov 2007 . . 145

*Til mine foreldre og min bror –uten dere ville jeg ikke vært den jeg er.*

*Education is a progressive discovery of our own ignorance.*

—Will Durant

# CHAPTER 1

# INTRODUCTION

> *A human being is part of the whole called by us "universe", a part limited in time and space. We experience ourselves, our thoughts and feelings as something separate from the rest... A kind of optical delusion of consciousness. This delusion is a kind of prison for us, restricting us to our personal desires and to affection for a few persons nearest to us. Our task must be to free ourselves from the prison by widening our circle of compassion to embrace all living creatures and the whole of nature in its beauty. The true value of a human being is determined by the measure and the sense in which they have obtained liberation from the self. We shall require a substantially new manner of thinking if humanity is to survive.*
>
> —Albert Einstein, 1954

The human race can ill afford to keep all of its citizens in the same planetary location. Just like a cancer victim who is unaware of his or her condition is not spared the effects of the illness, so too will the human race not be spared the consequences of a global disaster of epic proportions, whether it is man made or not. It is possible, albeit at significant risk and cost, to settle other planets and moons or even artificially constructed habitats in orbit or in deep space, using "only" today's technology.

Unfortunately, this is not yet happening on a scale that would be beneficial if disaster was to strike. While there are many reasons for this, it can all be argued to boil down to a question of resources. To undertake a permanent, self-sustained society located for example on Mars is an undertaking so breathtaking in scope that just seriously considering the efforts required turns into a costly study. But the fact remains the same; humanity needs to move in that direction and it possesses the technology to create such a habitat now, it is just unable to do so in the current political and economical climate. With today's rocket technology it would be prohibitively expensive for any one nation, or even a gathering of nations, to launch the required materials into orbit, let alone launch the immense amounts of material to another celestial body such as Mars. To do so would require an undertaking so big that nothing short of the complete and utter self-less cooperative work of the entire world would suffice. Unfortunately, humankind seen as a singular entity is seemingly incapable of such far reaching undertakings, constantly being pre-occupied with selfish acts of aggression and depravity towards itself. Sadly, the inability to perform is also not factored into the ramifications of a destructive, global disaster and pleas and lamentations of "not ready" and "why" will no more be heard in the imaginative "then" than the words "unity," "compassion" and "act now" are heard in the global community today.

With such dark thoughts on mind, it must be pointed out that the above does not have to be true and it does not need to happen. In fact much can be done and indeed *is* being done to prevent and diffuse as many scenarios of human destruction as is possible, from diplomacy and large alliances down to local politics and schooling steps. These are all actions taken on a daily basis to move humanity towards a better

future. Science too forms an important corner block in this work because while it is true that the creation of permanent human habitats using today's technology is an almost impossible endeavor in scope, it is also true that new and emerging technology will continue to lower the bar and make such a project more and more feasible. One such area of enabling technologies lies in the area of propulsion. Current rocket technology is close to hitting the proverbial wall. They are great mechanisms for producing huge amounts of thrust, but they are all woefully inadequate both when it comes to efficiency and when it comes to terminal velocity. This effectively makes them inadequate for manned missions to targets such as Mars. Not only would the payload carry capacity be severely limited, it would also take several months to reach the planet, even under the most favorable conditions. This is why advancements in other propulsion mechanisms are sorely needed.

## 1.1 Electric Propulsion

Electric propulsion has the potential to become the next generation in space propulsion and although it will still depend on more conventional technology to reach Earth's orbit, it has the potential to revolutionize space travel. Electric propulsion designs and concepts both currently employed, proposed and experimental, all bring the advantage of superior specific impulse ($I_{sp}$) compared to chemical alternatives. $I_{sp}$ represents the change in momentum per unit of propellant mass and as such it is linked to efficiency and can be compared to the "miles per gallon" metric of cars. The higher the $I_{sp}$, the less propellant that is needed to reach a set amount of momentum. On the flip side, even though the history of electric propulsion research now spans the

better part of a century [2], the thrust levels produced by existing electric propulsion systems are severely limited. Next to low thrust levels, the most difficult challenge in developing suitable deep space electric thrusters lies in the availability of a good power source. Close to Earth the radiated energy from the sun is still high enough (per unit of area) to be effectively used as a power source, but as a space craft travels further away from the sun, the available energy per unit area diminishes rapidly (as $1/4\pi r^2$, where $r$ is the distance from the sun) and alternate sources of electric energy become necessary. This implies that a sophisticated, on-board power supply system becomes necessary (above and beyond solar cells which for most missions provide ample power in Earth orbit). This in turn will increase the total system mass needed and can perhaps be somewhat likened to the added weight of turbo pumps, high pressure tanks and plumbing in conventional propulsion systems. Since the added mass of the power system will decrease the effective $I_{sp}$ and since thrust levels are directly linked to available power, it can be shown [3] with some assumptions that for a given system (consisting of a power plant and a thruster) there is an optimal $I_{sp}$ configuration in which the mass of the power plant needed is balanced with the wish for high thrust, high $I_{sp}$. Depending on mission parameters such as mission length and payload requirements, different optimal $I_{sp}$'s can be determined, and as shown in Jahn's "Physics of Electric Propulsion" [3], reaching for the highest $I_{sp}$ at the cost of everything else is just as undesirable as having too low of an $I_{sp}$ in the first place. This actually plays in favor of electric propulsion as it is much easier to custom tailor the $I_{sp}$ in an electric thruster. Indeed many thruster designs allow for the $I_{sp}$ to be varied dynamically by controlling various conditions such as the voltage or propellant flow

supplied to the thruster, *e.g.,* the Variable Specific Impulse Magnetoplasma Rocket, VASIMR [4].

Electric propulsion, defined as a system which can convert electric energy into kinetic energy in a propellant-medium can be divided into 3 families or categories, as suggested by Jahn [3] depending on how the propellant is accelerated in the system. Each group, as further detailed below, has its own associated advantages and disadvantages in terms of maximal $I_{sp}$ and thrust. It should be noted that these groupings are not mutually exclusive and many devices use a combination of two or more of these acceleration techniques to impart the kinetic energy to the propellant.

A summary of electrothermal, electrostatic and electromagnetic propulsion can be found in Jahn [3] and Filliben [5,6]. For completeness, these concepts are also briefly discussed in the following sections.

### 1.1.1 Electrothermal

Electrothermal devices are the simplest designs of electric propulsion. They are conceptually very similar to chemical propulsion systems in that the propellant is heated by some means and then expanded through a nozzle to convert the (random) thermal energy into directed kinetic energy. The difference between chemical and electric thrusters stems from how the heat is generated. In a chemical rocket the heat is generated through various chemical reactions and combustion processes, while in the electric version the propellant is heated electrically such as with a heating element. There are many designs that fall in this category, such as resistojets, arcjets, and various inductively or radiatively heated designs, but they all share the same fundamental

material limitations. In an electrothermal device, the thrust and $I_{sp}$ are directly related to how much heat is transferred to the propellant–the hotter the propellant gets, the higher the nozzle exit velocity. This immediately exposes one weakness of the design as there are very distinct upper limits to the temperature which the nozzle walls and structure can support. This limitation also applies, in some designs, to the heat source and heating elements. Possible ways to at least partially offset these limitations are offered by regenerative cooling of the nozzle in which cold (or even liquid) propellant is flown around the nozzle to cool it. The heat thus removed would then give a boost to the total heat added to the propellant as the propellant would be preheated by the time it reaches the heating elements/mechanism. The final wall of the (electro-)thermal design stems from fundamental properties of the propellant itself. Common propellants in electrothermal thrusters include ammonia ($NH_3$), light alkali metals, and exothermically reacting propellants (*i.e.,* hydrazine) [3]. The specific heat and thermal conductivity of the propellant also puts limitations in how much energy can be absorbed thermally by the molecules/atoms. Electrothermal designs are still in limited use today due to the simplicity and potential for low mass implementations of the designs. Typical performance values range from about 250 s to about 2120 s with a thrust range of 6.80 N to $5 \times 10^{-4}$ N [3]. The $I_{sp}$ is comparable to those of chemical systems, but the thrust produced is several orders of magnitude less than what can be achieved in a chemical rocket engine.

### 1.1.2 Electrostatic

In an electrostatic thruster, the thermal problems associated with the previous designs are avoided by directly accelerating the propellant using electric body forces. In its simplest configuration, *i.e.,* a gridded ion thruster, this is accomplished by accelerating a stream of charged particles (in this case ions) by means of a static, electric field. To avoid building up possibly damaging potentials on the space craft, electrons are introduced to the expelled stream of ions so that the net charge leaving the space craft is zero. Other electrostatic designs are colloidal ion thrusters and Field Effect Electrostatic Propulsion (FEEP) thrusters [3, 7]. These designs require very high voltages to be generated for the acceleration grids and it is more difficult to throttle the $I_{sp}$, possibly leading to sub-optimal $I_{sp}$ for a given mission. Performance values for typical electrostatic designs include $I_{sp}$ in the range of 3000 s up to 9000 s with thrust levels of $500 \times 10^{-3}$ N to $23 \times 10^{-3}$ N. Electrostatic devices are the most mature technology for use in commercial space crafts, but very focused and intense research into electromagnetic designs might change that.

### 1.1.3 Electromagnetic

The electromagnetic category is both the most promising and the most challenging category. In these devices a combination of electric and magnetic fields are manipulated to accelerate propellant and provide thrust. In so doing, it becomes possible, at least in theory, to both increase thrust levels to and beyond those of electrothermal designs and to maintain or improve the range of $I_{sp}$ available, assuming

additional power is available as well [7]. Most designs also allow for better control and variation of the $I_{sp}$ in "real-time" during a mission through various means such as varying propellant or propellant mixtures and power throttling, thus allowing the engine to run in its most efficient mode at all times. Due to the complexity of possible interactions between charged particles with magnetic and electric fields, a vast number of possible designs exists in various stages of research and experiments. Perhaps the oldest and most widely used design (in part thanks to Russia's extensive use of it in many of their space crafts) is the Hall effect thruster [8]. Examples of other designs in this category are MagnetoPlasmaDynamic (MPD) thrusters [9] and Pulsed Plasma Thrusters (PPT) [10]. For many of the electromagnetic designs, the useful lifetime of the thruster is limited by electrode erosion. One family of designs that actively attempts to deal with this problem is the inductively coupled, pulsed thrusters. However, even though inductively coupled pulsed thrusters remove the electrodes from the plasma, thus eliminating the biggest source of erosion (plasma-electrode interactions), they still have problems with erosion due to the interaction of the plasma with the (non-conducting) containment walls [11].

## 1.2 Pulsed Inductive Propulsion

In order to reduce electrode erosion and thus increase the life length of an electric thruster, the need for an electrode can be eliminated entirely. This can be accomplished by inductively coupling the energy from the power source into the propellant (plasma) in pulses. However, the insulator between the coil and the propellant does suffer from degradation to some degree from sputtering and ultra-violet expo-

sure [11]. Moreover, the thicker the separating material is, the worse the coupling efficiency between the coil and the plasma [3,7] as it decreases rapidly with separation distance. It should be noted that other design factors, such as impedance matching between the coil and the plasma, affect the coupling efficiency between the plasma and the drive coil(s) [12]. Another important consideration for many pulsed inductive designs is an effective scheme for recapturing energy from the ringing coils in order to improve overall system efficiency. This typically adds complexity and cost to the power supply of the system [13]. A recent publication by Cassibry, "Comparison of Directly and Inductively Coupled Pulsed Electromagnetic Thrusters" [14], introduces an analytical approach for comparing directly and inductively coupled concepts.

In the family of inductively coupled thrusters, different coil field geometries are possible, some common examples include inductors consisting of multiple parallel loops such as in the Pulsed Inductive Thruster (PIT) [15, 16], the Faraday Accelerator with Radio-frequency Assisted Discharge (FARAD) [17, 18], the theta-pinch & conical-theta-pinch [3], and the Magnetically Accelerated Plasmoid (MAP) [19,20] experiment. The common denominator is that the designs use the Lorentz force, $\mathbf{J} \times \mathbf{B}$, to accelerate the propellant. (The Lorentz force arise from the main magnetic field interacting with an opposite directed, induced current in the plasma which tries to oppose the externally applied magnetic field, thus producing a net force.) It is a further refinement of the basic conical-theta-pinch design which has been investigated in this thesis by adding a magnetic bias field system to the Plasmoid Propulsion eXperiment (PTX) in which plasmoids are accelerated to produce thrust as will be outlined in Chapter 2.

## 1.3 Outline

In the following chapters in this thesis, a literature review and the background to the Field Reversed Configuration (FRC) formation process and physics of plasmoid acceleration is presented in Chapter 2. A detailed look at the PTX experimental setup is given in Chapter 3 which also gives details about the various diagnostic systems and calibration efforts. In Chapter 4, results and analysis of results are presented. This is also where the QuickField™ modeling effort results are introduced and discussed along with a discussion on possible future improvements. Concluding remarks can be found in Chapter 5 where future work is also suggested.

# CHAPTER 2

# EXPERIMENTAL BACKGROUND

*Research is the process of going up alleys to see if they are blind.*

—Marston Bates

## 2.1 Overview

PTX is an inductively coupled thruster design in which a conical theta pinch coil is used to produce and accelerate plasmoids in order to create thrust. The formation process is conceptually not very difficult to understand, but it is a very challenging topic in physics due to the dynamic and interconnected nature of the various processes that take place during formation. As such, this is an area of ongoing research in both numerical simulations and laboratory experiments. M. Tuszewski's excellent "Review Paper – Field Reversed Configurations" [21] gives a thorough review on the subject of FRC- formation, equilibrium conditions, stability and confinement issues. Other works on FRC plasmas include those by Milroy [22] and by Kirtley [23]. A more recent paper by Polzin, "Scaling and Systems Considerations in Pulsed Inductive Plasma Thrusters" [24] gives new insight into the importance of pre-ionization arrangements, use of magnetic bias fields as well as considerations for optimizing the plasmoid acceleration by properly matching coil inductances. While the results in

Polzin's paper are in many cases only directly applicable to concepts using planar (flat) spiral coils, several of the concepts are equivalent in cases where the inductor is a theta- or conical theta- pinch coil.

The rest of this chapter contains a literature review on inductively coupled thrusters followed by a conceptual and theoretical background for FRC formations as related to PTX.

## 2.2 Previous Plasmoid Thruster Research

Conical theta pinches have been used in a variety of applications, including Tokamak refueling and fusion related research [22, 25–33], and propulsion research [23, 34, 35]. The discussion herein will be limited to the propulsion application due to its relevance in the current work. Included are other inductively coupled thrusters because the physics associated with them is relevant to the material presented in this thesis.

Among the first applications of the conical theta pinch was that of Bostick & Wells [36]. They set up a simple current-sheet model of hydromagnetic shock in an attempt to explain the origin of the poloidal rotation and the magnetic theta-field which had recently been observed experimentally [37]. Even using the simplified and limited model, they were able to clearly show that the vortex structure and fields were due to Hall currents. Further they showed that right handedness and left handedness (direction of rotation of the vortex) and the structure of the vortex all depend on the mass and charge of electrons and ions. The term "plasmoid" was used at least as early as in 1963 [36] and later in 1967 and 1968 in the papers by Valsamakis and

Small [38,39]. They studied the internal magnetic field geometries in plasma created by theta pinches in an experimental setup similar to that of PTX [1].

Three of the more well known types of inductive thruster designs include the Pulsed Inductive Thruster (PIT) [11,35,40–44], the Faraday Accelerator with Radio-frequency Assisted Discharge (FARAD) [17,18,45,46] and the Magnetically Accelerated Plasmoid (MAP) [19,20] experiment. In a PIT thruster, the accelerating coil is flat and the propellant is injected in towards the coil surface, as contrasted with PTX where the coil is a conical theta pinch and the propellant is passed through the coil. The FARAD design is similar to the PIT design but uses a pre-ionization scheme which together with the guide field not only helps move the propellant into position in front of the main coil [17], but also allows the thruster to operate at lower pulse energies ($44\,{}^{\mathrm{J}}/_{\mathrm{pulse}}$ versus $4\,{}^{\mathrm{kJ}}/_{\mathrm{pulse}}$ [18]). The FARAD is similar to PTX in that they both benefit from a dedicated pre-ionization scheme; however, the pre-ionization in PTX is electrostatically driven as opposed to the RF ionizing process used in FARAD. Slough's relatively new MAP concept accelerates FRC's to high velocities using a traveling magnetic wave. Since the accelerating (magnetic) field travels with the FRC, the coupling between the two does not suffer from the same rapid de-coupling as in PTX which in turn allows for much greater exit velocities and $I_{sp}$. On the flip side, due to the rapid acceleration of the FRC's in a MAP type thruster design, the magnetic coil system must be physically quite large in order for the magnetic wave to travel with the FRC for any significant time. Although PTX and MAP has some overlap in terms of usage, the MAP has the potential to scale much better with Mega-Watt power levels than that of PTX due to the possibility of keeping the coupling efficiency higher over a

longer time in the MAP design. PTX, on the other hand, would probably be a cheaper, more compact and simple solution for the kilo-Watt operating range.

## 2.3 Theoretical Background

A plasmoid consists of a self-organized plasma with internal currents and simply connected *closed magnetic field line topology*. More specifically there are mainly two categories of plasmoids–the Field Reversed Configuration (FRC) and the spheromak. The distinguishing feature of a spheromak is that the toroidal magnetic field strength is comparable to the poloidal field strength, $B_{toroidal} \approx B_{poloidal}$. In an FRC the toroidal field is negligible compared to its poloidal field, $B_{toroidal} \ll B_{poloidal}$ [21]. FRC's are typically formed either in straight or conical theta-pinch coils in a three step process wherein propellant is injected into the coil region, ionized and magnetized before a rapid field reversal in the coil forces the magnetized plasma to compress, heat and the plasma field lines to reconnect onto themselves. (The process for forming Spheromaks is typically different than for FRC's and is not covered in this discussion.) This process is conceptually illustrated in Figure 2.1 for the case where a magnetic bias field is present prior to ionization of the propellant. As seen in the upper left section of Figure 2.1, only the bias magnetic field is present. In the upper right part, neutral propellant has been injected in the Pyrex tube. In the lower left the bias field lines have been frozen into the now ionized propellant. For simplicity, the bias field lines outside of the propellant are ignored in this and subsequent frames of the figure. It should be noted that if the oscillating current, or "ringing", in the main coil starts off such that the main field is in the same direction as the bias field,

additional bias flux is available to the propellant and even more flux will be frozen into it. Alternatively, if the circuits are wired so that the first pulse of the main coil creates a field opposite to the bias field, then the process moves on to what is shown in the lower right where the field of the main coil comes on in the opposite direction to the bias field. Moving on to the leftmost part of Figure 2.2, the frozen field lines reconnect on themselves and in the right hand side of the figure, the fully formed plasmoid is accelerated out of the coil by the $\mathbf{J} \times \mathbf{B}$ (Lorentz) force until the plasmoid leaves the coil region. The $\mathbf{J} \times \mathbf{B}$ force is generated by the interaction between the main magnetic field and the induced secondary current in the plasma. A rapidly changing current in the main coil generates a magnetic field which induces an azimuthal plasma voltage described by Faraday's Law, $\frac{\partial \mathbf{B}}{\partial t} = -\nabla \times \mathbf{E}$, where $B$ is the magnetic field, $t$ is time and $E$ is the electric field. The secondary plasma current is described by Ampere's Law, $\nabla \times \mathbf{B} = \mu_0 \mathbf{J}$, where $\mu_0$ is the permeability of free space and $J$ is the plasma current. The coupling between the plasmoid and the coil rapidly diminishes as the plasmoid translates away from the coil. In fact, the mutual inductance between the coil and the plasma appears to decrease exponentially with the distance between the plasma and the coil [12, 15, 46, 47]. Because of this, efficient and strong acceleration depends on a fast coil current ($I$) rise time $^{dI}/_{dt}$ during the acceleration phase, so that as much energy as possible is imparted to the plasmoid while it is still relatively close to its place of creation. Since the plasmoid has its own self contained magnetic field, the propellant is completely detached from the thruster and thus there is no need for a magnetic nozzle to prevent backflow. Other advantages of the closed field lines of a plasmoid include reduced interaction with

the wall of the thruster and better coil/propellant coupling [21, 24]. Plasmoids can be accelerated to very high velocities, with velocities exceeding $200\,{}^{\mathrm{km}}/_{\mathrm{s}}$ achievable in certain laboratory settings [48, 49]. Such high velocities are commonly required in fusion experiments where a plasmoid is typically accelerated to high speeds and then collided into the fusion propellant (which could be another plasmoid).

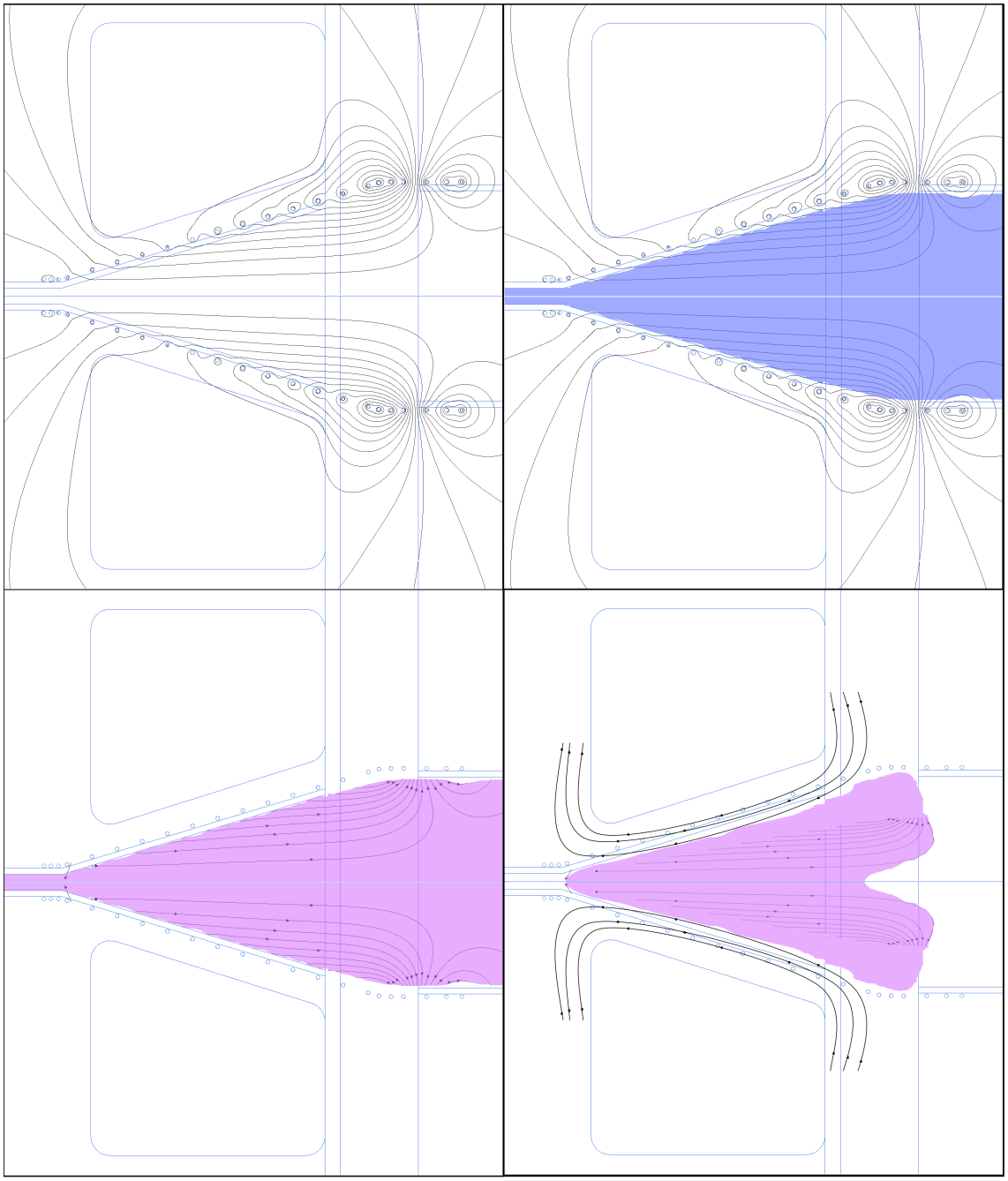

**Figure 2.1**: Conceptual FRC formation process with the presence of a magnetic bias field. [Left to right, top to bottom, the figures illustrate: –"Static" magnetic bias field with no propellant present. –Neutral propellant is injected. –The propellant is ionized on the bias field lines, freezing the field in. For reasons of clarity, the magnetic bias field outside of the ionized propellant is not drawn in this and subsequent frames. –The main coil field comes on and opposes the bias field. This causes compression of the ionized propellant.]

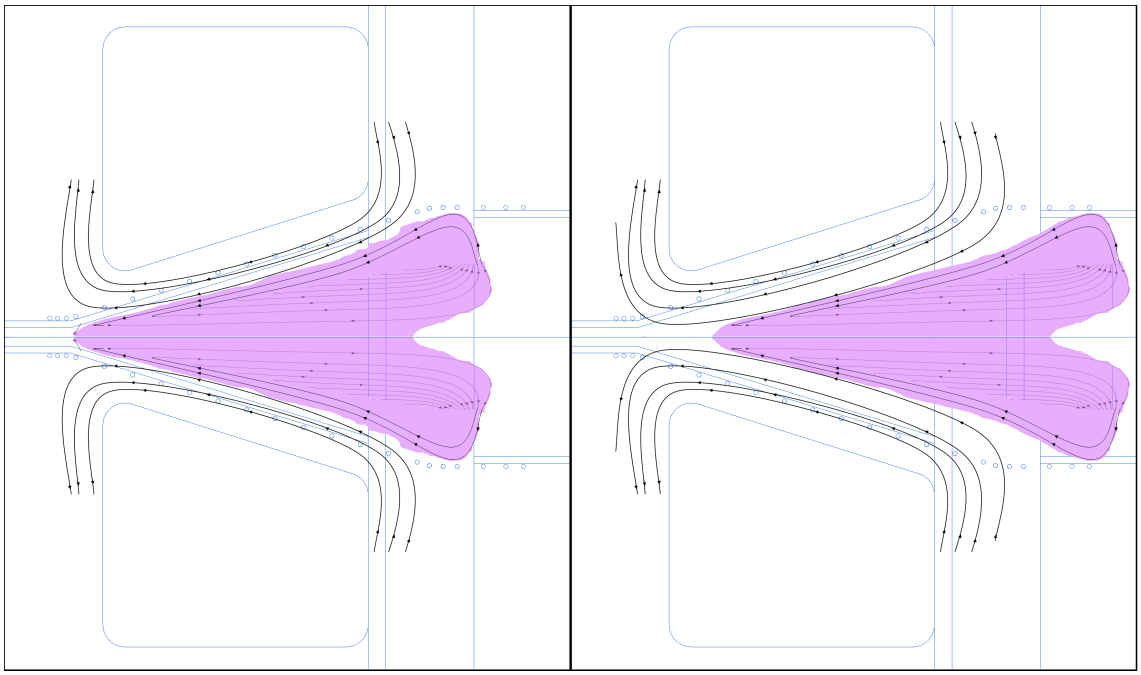

**Figure 2.2**: Final stage of conceptual FRC formation process with the presence of a magnetic bias field. [From left to right the frames show: –After radial compression, the frozen field lines tear off at the x-points and reconnect, forming a plasmoid. –In the last frame, the now fully formed plasmoid is shown accelerating away from the coil surface.]

# CHAPTER 3

# EXPERIMENTAL SETUP

*Science is organized knowledge.*

—Herbert Spencer

## 3.1 Overview

In broad terms, the experimental setup that is PTX has the following components and sub-systems which will be further detailed in this chapter:

- Main Coil System
  - Conical Theta Pinch Coil
  - Main Capacitor
  - Main Spark Gap Switch
  - Main Capacitor Power Supply
  - Pre-Ionizer System
- Bias Field System
  - Bias Field Coil
  - Bias Capacitor Bank
  - Bias Silicon-Controlled Rectifier (SCR) Switch
  - Bias Capacitor Power Supply
- Propellant Feed System
  - Pressure Regulator
  - Fill Valve

  - Puff Valve
  - Vacuum Chamber
- Control System
  - Computer for Operation of Software Controlled Systems
  - National Instruments Field-Point System (NI-FP)
  - Berkeley Nucleonics Pulse Delay Generator (PDG)
  - Bias Coil Control
  - Interlock & Safety Systems
  - Fast Optical (Timing) Control System
  - Slow Optical Control System
- Data Acquisition System
  - Acqiris High Speed Digitizer System
  - Computer for Data Retrieval and Archiving
  - Oscilloscope
  - NI-FP Slow Analog Input (for control and monitoring)
- Diagnostics System
  - Laser Interferometer System
  - Bias System Pearson Current Probe
  - Bias System Voltage Divider Probe
  - Propellant Reservoir (Plenum) Pressure Sensor
  - $\dot{\mathbf{B}}$ Probes
  - Flux Loops ($\Phi$-loop)

## 3.2 Main Coil System

The purpose of the main coil system is to create and accelerate plasmoids out of the conical theta pinch coil (main coil) as discussed in Chapter 2. The system composition is outlined in the following sub-sections and a distinction has been made between the plasmoid formation system and the bias field system to avoid confusion and to facilitate a detailed discussion of the separate components; however, they are both part of the same overlying system that is PTX.

### 3.2.1 Conical Theta Pinch Coil

The single turn conical theta pinch coil was machined out of a solid block of aluminum with an inner half-angle of 17.5 °. The coil is 3 in wide and has an outer diameter of 7 in, a throat (inner) diameter of approximately 0.75 in and a mouth (inner) diameter of approximately 1.5 in. A side cut-away view of the coil can be seen in Figure 3.1 and a photograph of it can be seen in Figure 3.2. A second coil was machined with a 8.5 ° angle, but this coil has not yet been used on the experiment. The choice of coil angle was decided by Richard Eskridge of Marshall Space Flight Center (MSFC) to conform to that of the Thermonuclear Reactor In Support Of Project Sherwood, TRISOPS, colliding plasmoid experiment [50], built by Dan Wells at the University of Miami. Later, a comparison of directly and inductively coupled, pulsed thrusters in which the effects of coil angles were considered was carried out numerically in a study by Cassibry and Wu, "Comparison of Directly and Inductively Coupled Pulsed Electromagnetic Thrusters" [51]. Aluminum was used over copper due to cost and weight considerations while having a comparable electric conductivity of $37.8 \times 10^6$ S/m (copper has a conductivity of $59.6 \times 10^6$ S/m) [52]. The inductance of the main coil was inferred to be 27 nH in a previous study [1].

### 3.2.2 Main Capacitor Bank

The main capacitor bank consists of two Maxwell model 31235 high voltage, high pulsed current capacitors with the nominal capacitance of each unit listed as 300 nF and a voltage rating of 100 kV. The capacitors form a bank with a measured

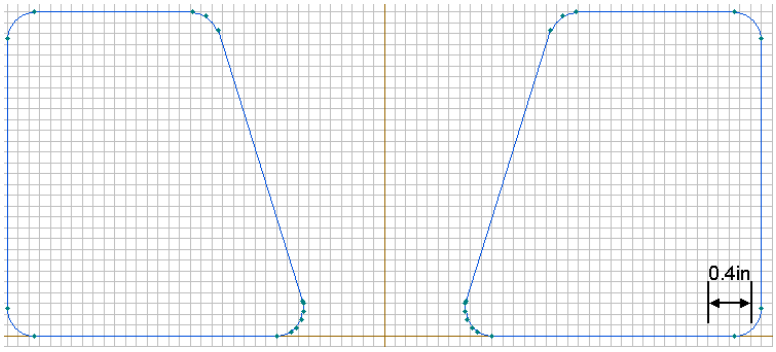


**Figure 3.1**: Top down view of the main coil. [The throat is at the bottom and the mouth at the top.]

**Figure 3.2**: Photograph of main coil. [Note the Pyrex tube in the background with the old configuration of the excluded flux array.]

capacitance of 618 nF. The bank is normally operated in the 18 to 35 kV range. The range is upward limited at 50 kV by the available power supply, a Spellman model SL1200 50kV 1200 W unit, and further limited in normal operation to 35 kV due to safety considerations. The downward limiting factor is the switch, a Perkin-Elmer model GP-32B triggered spark gap switch which does not operate at voltages below approximately 15 kV and only operates reliably at voltages at or above 18 kV. When operated at 35 kV, the peak currents in the main coil have previously been determined to be 50.4±1.3 kA [1], and the equivalent circuit values for the RLC-system consisting

of the bus bars, capacitor bank, and main coil, have previously been determined to be 55±3 mΩ, 620±30 nF (assumed) and 155±8 nH respectively [1]. The RLC circuit gives a damped sinusoidal response with a frequency of 514.7±0.5 kHz and a damping constant of 5.64±0.40 $\mu$s [1]. The energy contained in a capacitor is given by

$$E_{Capacitor} = \frac{1}{2} C V_{Capacitor}^2 \,, \tag{3.1}$$

where $C$ is the capacitance (in Farads) and $V_{Capacitor}$ is the voltage on the capacitor. If PTX is charged to 35 kV, this corresponds to $\approx$ 379 J, using the measured value of 618 nF for the bank capacitance.

Because of the high energy levels present in this system, a number of safety mechanisms have been implemented. The capacitors are contained inside an acrylic tank housed in a steel enclosure as depicted in Figure 3.3. The main purposes of the steel enclosure are to provide ballistic shielding in the event of a catastrophic failure of the capacitors, and to provide a grounded shield around them to contain accidental discharges. Both enclosures are filled with Shell Diala AX transformer oil to provide insulation and prevent arcing in the system. Additional arcing protection in the form of mylar sheets is in place at key locations where the total distance between hot and ground is at a minimum. The voltage level of the capacitors is monitored through a voltage divider made up of high-voltage rated resistors. The resistors are also submerged in the oil inside the tank for safety. The steel outer tank is hardwired to ground using a thick braided conductor going to the grounding plate and the dedicated grounding rod, a 15 ft solid copper rod driven into the earth,

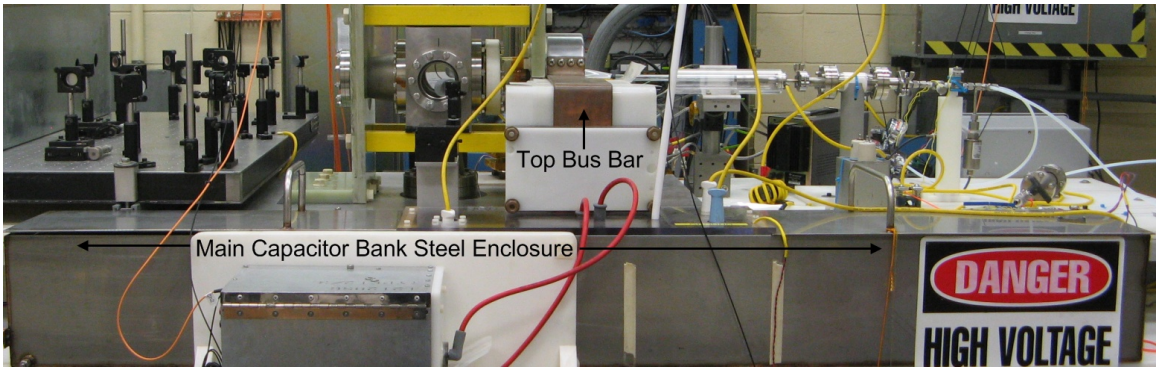


**Figure 3.3**: Main capacitor bank enclosure, seen from the side.

along with a saturated salt solution. The rod is located next to the experiment. The salt aids in providing good conduction from the copper rod and into the ground.) A manual dump mechanism exists which when activated (by pulling a string) will connect the hot terminal on the capacitor bank with earth ground. A computer controlled, normally closed (N.C.) relay provides the primary grounding mechanism and the experiment computerized controller will ground the capacitor bank using this relay shortly (a few seconds) after the spark gap switch has been activated. As such, if the spark gap switch fails to properly discharge the main bank, or if there is a residual charge in the main bank at the end of the experiment, it will be safely grounded and de-energized through a current limiting resistor. Further safety features are discussed in Section 3.2.4 about the power supply.

### 3.2.3 Main Spark Gap Switch

The switch used to close the main circuit is a Perkin-Elmer model GP-32B triggered spark gap switch. It is triggered by a fiber-optic signal which trips a high-voltage pulse on the order of 30 kV. The pulse creates a spark in the switch, creating a

conduction-path for the main bank to discharge through the spark. Timing accuracy between when the optical signal is sent and the pulse triggers the switch is on the order of 20 to 50 ns [1].

### 3.2.4 Main Capacitor Power Supply

The power supply used to charge the main capacitor bank is a Spellman model SL1200 50kV, 1200 W unit. It is remotely operated and completely isolated from building power by the use of a ProSine DC-AC inverter. The desired voltage is set by means of a battery operated, optically insulated analog output (AO) from the National Instruments Field-Point System (NI-FP) analog output module (see Section 3.5.2). The AO is converted to an optical signal, where the brightness of the optical signal is directly proportional to the AO signal. The optical signal is then converted back to an analog voltage by means of another conversion circuit located by the Spellman power supply. This particular AO link was calibrated using a Fluke 5100 multi-calibrator (hereafter referred to as the Fluke calibrator) to ensure reliable operation. For added safety, there is also a digital, optical line which acts as an interlock/arm system. If the interlock is logic low (*i.e.,* no light), the power supply is disabled regardless of the AO setting. The power supply is isolated from the capacitor bank by means of a Ross Engineering High Voltage relay which is normally open (N.O.). When the computerized experiment controller determines that it is time to charge the capacitor, this relay is closed. A manual high voltage relay also acts as a safety grounding point. The manual relay is normally closed (N.C.) and needs to be manually opened and locked in place prior to running the experiment. In the event of a critical failure,

the power supply output can be grounded by pulling the string which keeps the relay open. (A separate manual and automatic grounding system is in place by the main capacitor bank for a total of 4 possible grounding mechanisms.)

### 3.2.5 Pre-Ionizer System

In the early version of PTX, ionization of the propellant and subsequent plasmoid formations were in full facilitated by the main coil and its driving circuit. Over time, PTX stopped forming plasmoids, and the source of the problem turned out to be conditioning of the main bank spark gap switch. It turned out that the spark gap switch exhibited a very high frequency switching noise which caused the initial ionization and allowed the fields to further compress and ionize the propellant. After communicating with the manufacturer of the spark gap switch, it was determined that this switching noise was well known to exist in most switches and that it normally went away after several hundred to a few thousand switch cycling's. In order to make plasmoid creation more deterministic, it was decided to include a dedicated pre-ionizer system. In Fimognari's work [1], the pre-ionizer consisted of a Bertan 50 kV high voltage power supply connected between the puff-valve flange and the steel body of the vacuum chamber. This design had multiple problems associated with it in terms of unwanted and damaging arcing in the puff-valve region as well as potentially hazardous coupling to other systems through the shared ground. This was remedied in the new, current setup.

In the current setup, a smaller power supply, an EMCO model F40, better matched to the task was used. The F-series is an isolated DCDC power supply sim-

ilar to the one used to charge the bias capacitor bank (Section 3.3.4). This allowed the pre-ionizer to be battery operated, significantly decreasing the potential safety risks for other systems. To further reduce the risk of harmful interactions between the pre-ionizer and the other systems, a high-voltage vacuum insulation section was put between the puff-valves and the Pyrex tube. This created an isolation barrier to protect the valves from potentially harmful voltage levels. Additionally, the return in the pre-ionizer was isolated from the vacuum chamber walls by the use of a high-voltage vacuum feed-through flange with a suspended cathode hanging inside the chamber. This further forces the electron current to only take the predefined and correct path from the output (anode) of the power supply and back to the return (cathode) on the power supply. The cathode on the chamber feed-through was connected to the power supply through a spark-plug wire rated for 50 kV. The wire was run inside of a PVC tube to further mitigate the risk of accidental exposure by equipment or personnel. The power supply was current limited with high-voltage resistors to ensure operation inside of factory specifications during gas break-down. Ferrite chokes on the cathode and anode wires were used to dampen any spurious spikes during the initial breakdown and final collapse of the ionized propellant stream. The system is able to sustain constant ionization up to a pressure of several Torr at which point the gas becomes too dense, and the ions recombine too quickly to support an electron current across the entire span. A manual safety dump switch was integrated into the system so that the power supply output could be forced to ground (through the current limiting resistor) if needed.

### 3.3 Bias Field System

The purpose of the bias field system is to provide a set of (preferably static) magnetic field lines inside the main coil volume. When the main circuit is discharged through the main coil (depending on the polarity of the bias field current), the magnetic field from the main bank is antiparallel to the bias field. The preionized plasma becomes trapped on the bias field lines, and resistive tearing in the plasma at the bias/main field interface leads to plasmoid formation. The same process can be accomplished without a dedicated magnetic bias field system by the main coil at the expense of slower formation and less energy available for the acceleration phase. The bias field may permit higher energy fields and greater thrust densities by allowing the main coil to form and accelerate the plasmoid on its first half-cycle. In addition, the bias coil system was designed such that it provides two natural x-points, one on either side of the main coil. (An x-point is a region where the magnetic field gets pinched, such as between two coils with opposing fields.) It is known [21, 24] that embedding a bias field in the plasma as it is created can speed up the formation of the plasmoid by one half period and also possibly create a denser plasmoid. Speeding up the formation process by one half period makes an appreciable difference in the main magnetic field energy available since the main system exhibits an exponential decay thus rapidly diminishing the energy available to do work on the plasmoid. Additionally, a stronger internal plasmoid field would likely aid in acceleration by providing a "firmer" plasmoid for the main fields to push against.

### 3.3.1 Bias Field Coil

The bias coil consists of a high-voltage, doubly insulated, multi-stranded silvered wire wrapped around the PTX Pyrex tube (see Figure 4.2). The wrappings form 3 distinct sections in series, 2 x-point sections situated one outside of both the main coil throat and mouth, and 1 "main bias" section situated directly underneath the main coil. The x-point sections consists of 3 turns at the throat and 3 turns in the section by the mouth. Both sections are wound in the opposite direction of the main bias windings. The main bias windings consist of a total of 16 loops spread out under the main coil as evenly as the $\dot{\mathbf{B}}$ and $\Phi$-loop wires already there would permit. (The $\dot{\mathbf{B}}$ probes are inductive probes resembling tiny solenoids which are used to measure the rate of change of magnetic fields with respect to time. They are detailed in Section 3.7.5. A flux-loop is another inductive probe, typically consisting of a single loop of wire. It measures the magnetic flux bound by the wire and it is detailed in Section 3.7.6.) The transition from one section to the other consists of a sharp u-turn bend in the wire, reversing the direction of the winding as sharply as possible without compromising the insulation materials.

The resistance and inductance of the coil was measured using an RLC meter and found to be approximately $0.072\,\Omega$ and $6.8\,\mu$H respectively. Both measurements were made by shorting out the SCR switching diode using a solid copper wedge, but with the capacitor bank disconnected, since the capacitance would adversely affect the inductance and resistance measurements. Next, the capacitance of the bias bank

was measured and determined to be approximately 17.3 mF, and this measurement was made with the capacitor bank disconnected from the rest of the bias system.

It should be noted that measured resistance fails to take into account any dynamic resistance due to the SCR switch itself. Therefore, the total system resistance was estimated by analyzing data taken by charging the bias bank to a known voltage and discharging it into the bias coil through the SCR. The voltage and current during this discharge was recorded using an Oscilloscope and saved to a comma separated values (CSV) file which was then analyzed. Since the strength of the bias field is directly dependant on the current in the bias coil and since it is the field strength at the time when the propellant is pre-ionized and the main coil is fired that is of interest, only the current during the peak is considered. The average resistance, $R$, was calculated using the resistance of each data point $\pm 100\,\mu$s around the peak current. This was done for 4 different test shots ranging from 42 V to 336 V. The average system resistance for the range of charge voltages of interest was calculated (using Ohm's law, $R = {}^{V}/_{I}$, where $V$ is the voltage potential and $I$ is the current) to be $0.074\,\Omega$. The current was measured using the Pearson current monitor described in Section 3.7.2. The complete set of results is displayed in Table 3.1.

**Table 3.1**: Results of the overall system resistance as determined using Ohm's Law and experimental data [1].

| Voltage at Peak ($V$) | Current at Peak ($A$) | Min ($\Omega$) | Average ($\Omega$) | Max ($\Omega$) | Stdev ($\Omega$) |
|---|---|---|---|---|---|
| 42 | 640 | 0.063 | 0.071 | 0.077 | 0.003 |
| 124 | 1712 | 0.063 | 0.074 | 0.078 | 0.002 |
| 224 | 3040 | 0.071 | 0.074 | 0.078 | 0.002 |
| 336 | 4440 | 0.074 | 0.077 | 0.080 | 0.002 |
| | | **Average** | **Average** | **Average** | |
| | | 0.070 | 0.074 | 0.078 | |

### 3.3.2 Bias Capacitor Bank

The bias capacitor bank consists of 16 individual Mallory "CGS102T450W4C" electrolytic capacitors rated for 450 VDC (as opposed to the main bank which is not polarized) and with a rated capacitance of 1000 $\mu$F. The total *measured* capacitance of the bank is 17.3 mF which puts an upper energy limit of $E_{Bias}$ =1.75 kJ on the system. This is a factor of 4.6 times more energy than the main bank. The bias bank was intended for operation in the range of approximately 150 to 250 VDC resulting in an energy range of 0.51 to 1.4 times the maximal energy of the main bank. This expected operating range was determined in order not to totally dominate the main field energy. The impetus for having such a large bias capacitor bank stems from the need for the bias RLC system to be critically damped so as to avoid field reversal due to negative ringing voltage components during the discharge *and* to make the pulsed nature of the bias system slow (*i.e.,* "constant") on the time scale of the main bank discharge.

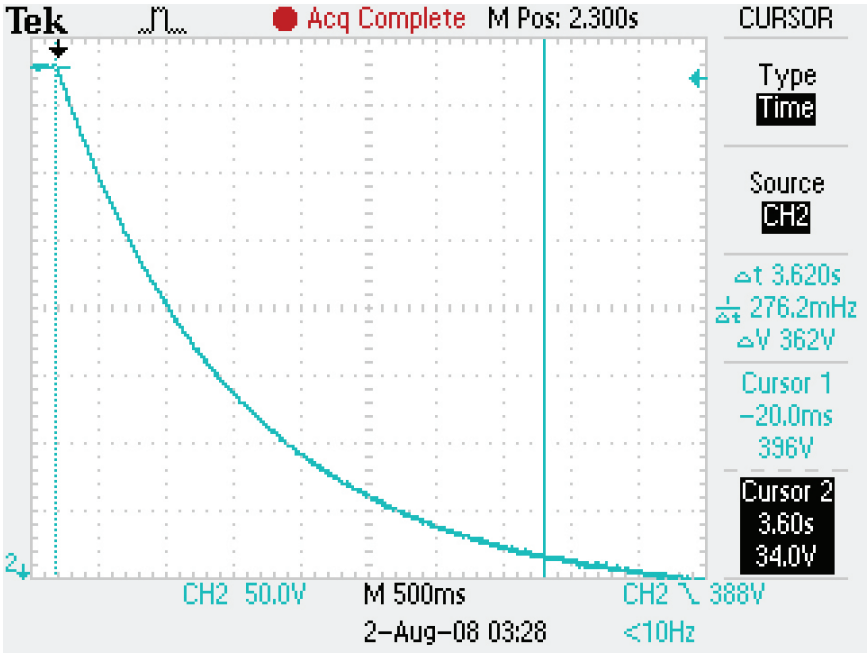


**Figure 3.4**: Automatic safety discharge profile. [This oscilloscope plot shows the voltage of the capacitor bank as it is dumped through the automatic safety dump system into a pair of high-power resistors. The initial voltage is at 396 V which reaches a safe level (defined as a DC voltage equal to or less than 36 V) after approximately 3.6 s.]

The bias capacitor bank has an automatic and a manual bleed switch for safety. From the moment the bleed resistors are applied (either automatically or manually) it will take approximately 3.6 s to bring the bank down from 392 V to less than 36 V. The manual dump takes slightly longer to reach a safe level at 3.8 s. The details of an emergency dump event can be seen on the oscilloscope plot shown in Figure 3.4. A similar case occurs in the event that the manual dump system is used. The automatic system is engaged by the computerized controller at the end of each experimental run.


**Figure 3.5**: The SCR device sandwiched between two aluminum plates.

### 3.3.3 Bias Silicon-Controlled Rectifier Switch

The Silicon-Controlled Rectifier (SCR) used to switch the bias current is an International Rectifier model SC180C12CFK0. It is a solid state device which allows a high voltage, large $\frac{dI}{dt}$ to be controlled by a (relatively) small control voltage. The principal of an SCR is basically that of a diode. The SCR was mounted in compression between two aluminum plates using 4 threaded nylon rods. A torque wrench and Belleville springs were used to assure that the mounting pressure on the SCR fell inside of the manufacturer recommended 4000 N mounting force. A picture of the SCR device sandwiched between the compression plates can be seen in Figure 3.5. The maximum (non-repetitive) forward surge current through the SCR is listed in the data sheet as 5230 A and the maximal rate of rise of the current is 1000 $^{\mathrm{A}}/_{\mu\mathrm{s}}$. The trigger input, called a "gate" should be given trigger conditions close to its maximum ratings, 10 W peak (duration <5 ms) using at most 3 A and 20 V. This is to force the SCR to turn on as quickly as possible. This is important to the longevity of

the device since partial or slow turn on times will result in extreme hot-spots inside the device as the connected capacitor bank will try to discharge its energy through a small conducting area near the gate. The stronger the SCR is turned on, the faster the conducting area will grow to encompass the maximal conducting area thus minimizing thermal stresses on the SCR dielectric. Since the SCR will only conduct for short, non-repeating pulses, and because it has been mounted between two thick pieces of aluminum, thermal dissipation in the device is not expected to be a problem. (These devices are normally used to switch loads on and off with a frequency of 50 to 60 Hz.)

### 3.3.4 Bias Capacitor Power Supply

The power supply used to charge the bias capacitor bank is an EMCO model F50H. It is a small, self-contained unit which produces a voltage output proportional to the voltage input such that a 12 V input produces a 500 V output. At the maximal rated input voltage, the unit is capable of continuously supplying 10 W to the output terminal. The output is transformer isolated from the input and the power supply is mounted on a custom made controller board. The board provides the means to optically control the power supply (to turn it on or off) by means of 2 circuit board relays, one relay to connect the power supply to its input source and one to connect the supply output to the capacitor bank. The purpose of the output relay is to isolate the power supply from the capacitor bank during a discharge. This prevents possible voltage spikes and transients from damaging the power supply. The relay on the power supply input is of course a safety mechanism in that it prevents the output

terminals from being hot while the supply is not used to charge the capacitor bank. Charge times for the capacitor bank are dependant on the charge voltage not only because of the voltage dependency in the capacitor energy Equation 3.1, but also because the power supply output power decreases as the supply is operated below its maximum input voltage. Typical bank charge times are in the single minute to a few minutes range.

## 3.4 Propellant Feed Sub-System

The propellant feed sub-system provides propellant under a variety of conditions. It is designed to accept gaseous propellants although the PTX could in theory be used with solid or liquid propellants with some modifications to the propellant delivery system and to the pre-ionizing system. The pressure regulator, fill valve, puff valve and reservoir are shown in Figures 3.6 and 3.7.

### 3.4.1 Pressure Regulator

To regulate the pressure of the propellant feed system, a manual valve and dial pressure gauge is used to bring the pressure down from the K-bottle supply (typically 2500 psi) to the range commonly used for PTX (5 to 30 psi). The low side of the regulator passes through a manual control valve and into a pressure reservoir. The reservoir has a volume of approximately 18.8 $in^3$ (about 0.31 l) which is more than 360 times larger than the largest observed plenum (puff) volume. (Due to the uncertainties associated with the determination of the plenum volume, a range of volumes was indicated and the highest value found across all the tests was $8.5 \times 10^{-7}\, m^3$.)

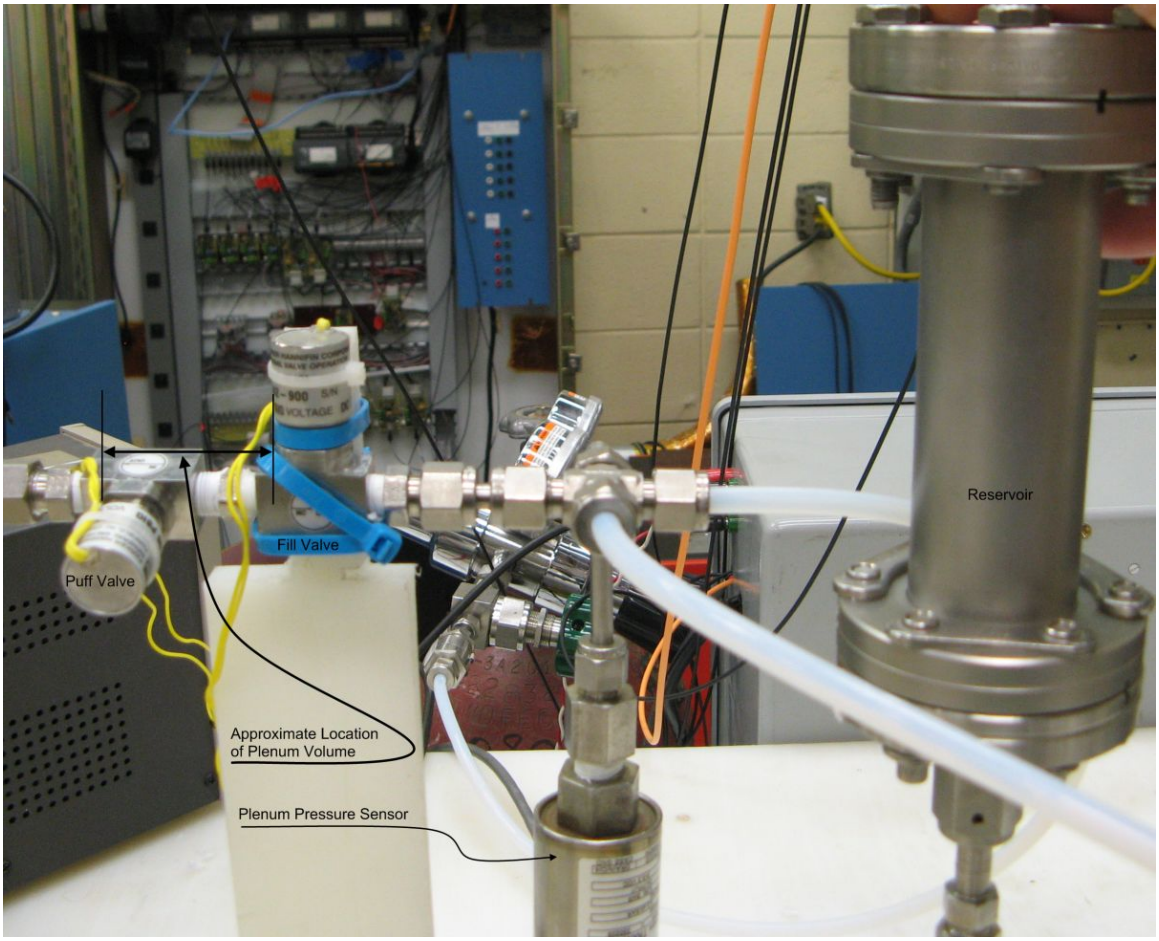


**Figure 3.6**: The propellant feed system. [It consists of a pressure regulator (background), a fill valve, a puff valve and a pressure reservoir.]

This large difference substantiates the necessary assumption that the pressure of the plenum volume (see Section 3.4.2 for details on the plenum volume) will be the same as the pressure of the reservoir after a short time of exposure. The reservoir consists of a 5 in length, 2 in diameter metal pipe fitted with a bleed-valve and connected to the first automated valve - the fill valve.

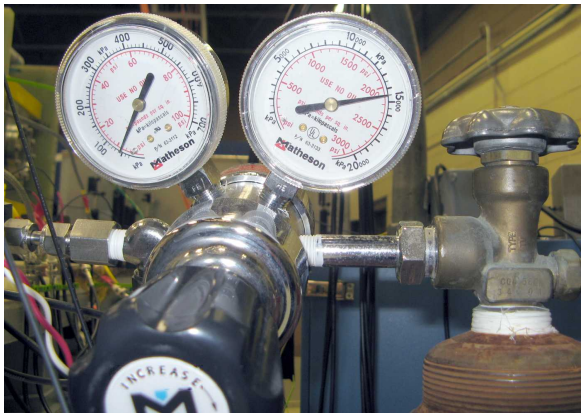


**Figure 3.7**: Close up of the pressure regulator, here with Nitrogen.

### 3.4.2 Fill Valve

The fill valve is a N.C. Parker-Hannifin Corp. 100 psig, 24 VDC valve acting as a block between the pressure reservoir and the opening of the puff valve. This allows for well defined amounts of propellant to be injected into PTX. The outlet of the fill valve is connected to the input of the puff valve using a short union pipe-fitting. The fitting was filled with epoxy and a hole (12 mil diameter) was drilled through the center of the epoxy. The purpose of filling up the void in the union fitting was to minimize the total plenum volume. Since PTX operates with minuscule amounts of propellant, a small plenum volume is essential for good control of the total injected propellant mass. The plenum volume in this system is considered to be the volume between the output of the fill valve and the output of the puff valve as indicated on Figure 3.6. As discussed in Section 3.8.2, the plenum volume has been determined to be in the range of approximately $4.5 \times 10^{-7}\, m^3$ to $8.5 \times 10^{-7}\, m^3$. (Again, it is clear that the plenum has one and only one volume, but the uncertainty in the calibration

of this volume gave rise to different values being determined depending on what gas was used and what the open time on the puff valve was.) The fill valve is operated by an optically triggered 24 V signal and is opened for 15 s prior to and 5 s after a shot. There are a couple of seconds between closing the fill valve and puffing the puff valve to guarantee the plenum is sealed prior to puffing. The exaggerated fill times allow ample time for the plenum to fill and equilibrate with the reservoir.

### 3.4.3 Puff Valve

Another N.C. Parker valve makes up the puff valve in the system. Unlike the fill valve, the puff valve is operated out of specifications. The puff-valve driver operates the valve with a several hundred volts, 250 $\mu$s pulse, as defined by the PDG. The high-voltage pulse drives the valve open rapidly to minimize effects on the propellant flow caused by the valve opening gradually. (The valve nominal rating is 24 VDC at 50 psig.)

The amount of propellant injected into PTX is controlled by one of two methods: controlling the plenum pressure or the pulse width of the puff valve driver signal. Fimognari (2008) used both methods, but it should be noted that in that setup, there was no fill valve. As such the entry side of the puff valve was exposed to the propellant source pressure with only a small pin hole to restrict flow. This meant that the total amount of propellant injected would depend on the length of time the puff valve was open, which is in contrast to the current and improved setup where there is only a finite amount of propellant available no matter how long the puff valve is left open. During testing it was observed that a 250 $\mu$s open time was sufficient to

inject approximately 94 % of the propellant in the plenum. In order to characterize the amount of propellant injected in a puff, it is necessary to know the plenum pressure, the plenum volume and the plenum propellant temperature. The temperature is assumed to be ambient since the source is at ambient and the expansion into the reservoir is slow and the mass expanded into the plenum is very small compared to the material of the plenum (which is also at ambient). The plenum volume of the puff valve must be inferred from measurements of the plenum pressure and the vacuum chamber pressure and volume, as well as how much the vacuum pressure changes when the plenum is emptied into the vacuum source. For details on determining the vacuum chamber volume and the plenum volume, see Sections 3.8.1 and 3.8.2.

### 3.4.4 Vacuum Chamber

Plasmoid creation with properties sought after in the PTX is only feasible in a vacuum environment. The vacuum does not need to be a "hard" vacuum and PTX will readily work in pressure ranges of $5{\times}10^{-5}$ Torr and lower. The nominal pressure during operation is approximately $8 \times 10^{-7}$ Torr just prior to injecting propellant. During repeated plasmoid shots, the pressure typically reaches the $10^{-6}$ Torr range prior to the next shot. The PTX vacuum system consists of two main enclosures, a Pyrex tube and a rectangular steel vacuum chamber as seen in Figure 3.8. Vacuum pressures are reached using a turbo-pump backed with a roughing pump. The roughing pump, a Leybold model D2.5E Trivac Rotary Vane pump, Figure 3.9, brings the chamber down from atmospheric to sub $250 \times 10^{-3}$ Torr before the turbo pump, a Leybold Turbovac 50 unit, Figure 3.10, is turned on to finish evacuating the chamber. Both

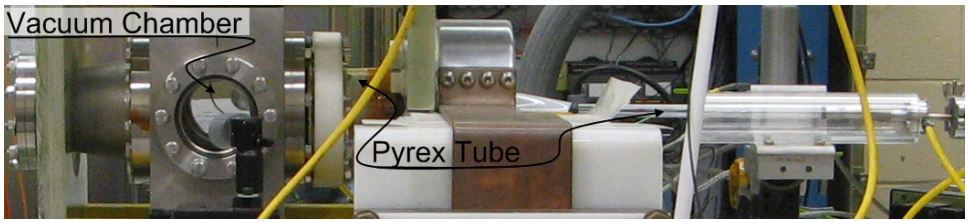


**Figure 3.8**: The main vacuum enclosures.

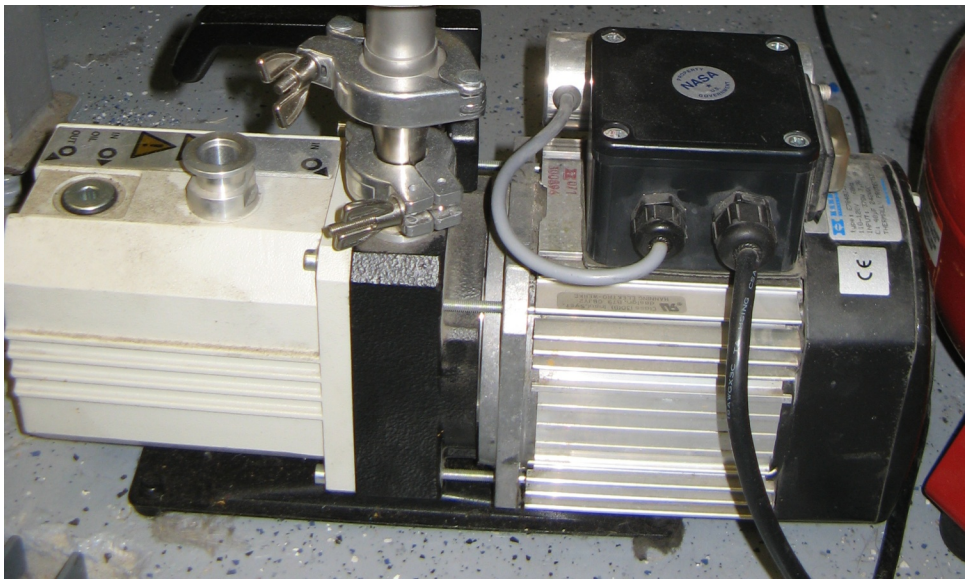

**Figure 3.9**: The roughing pump.

systems are left running during the experiment to maintain vacuum pressures and remove the spent propellant. A gate valve can be closed in the case where a static fill is wanted. The pressure is computer monitored using an MKS Instruments Baratron Gauge and a manual dial gauge readout from an ion-gauge is available for readings of pressure below the $10^{-3}$ Torr range.

The Pyrex tube consists of two main sections, a straight, thin tube and a sloped transition to a wider cylinder which attaches to the steel chamber with an o-ring flange. The small straight section has an outer diameter of 9.18 mm and the

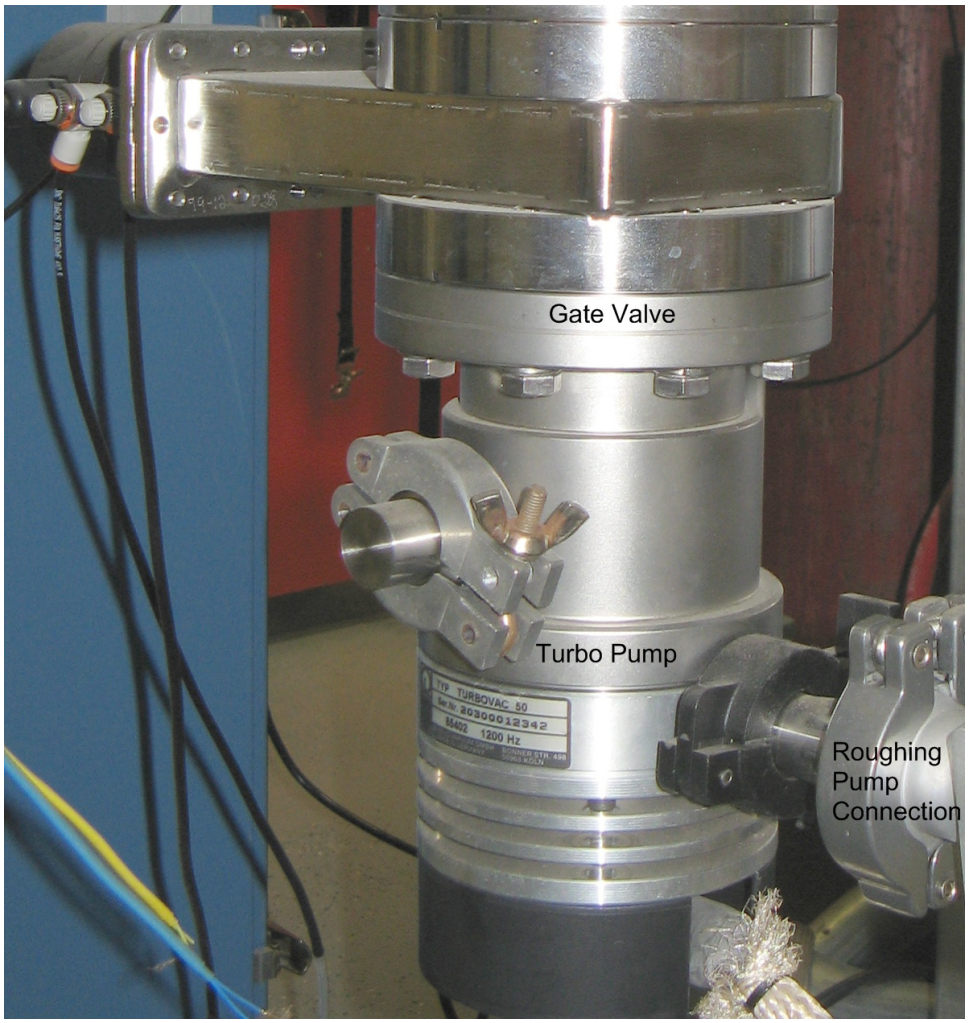


**Figure 3.10**: The turbo pump.

section is approximately 290.8 mm long. The tube wall is approximately 2 mm thick. The sloped section has a 17.5 ° half-angle to it and is conical. It transitions to a second straight section at the point where the inner diameter is 68.6 mm.

The rectangular steel chamber has outer dimensions of 8 x 8 x 5 in and the walls are 1 in thick. The steel chamber has 6 larger ports to it. The 2 side-view ports with a diameter of 4 in provide the laser interferometer with optical access to the inside of the chamber. The windows also allow visual inspection of static pre-ionization as

well as plasma or plasmoid formation which appears as a bright flash. (It should be noted that it is impossible to distinguish an arbitrary plasma formation from a plasmoid formation by visual inspection. Figure B.2 shows a photograph of a typical plasma/plasmoid shot using Argon as propellant.) The top port houses the isolated high-voltage feed-through of the pre-ionizer cathode and the bottom port interfaces to the turbo pump assembly. Of the 2 axially aligned ports, one is fitted with the o-ring seal which connects the Pyrex tube to the chamber, and the opposite side has an elongated reducer fitting attached to it to allow accelerated plasma or plasmoids to travel further downstream before interacting with the walls of the chamber. In addition, the chamber has several smaller ports used for a bleed-valve port, the ion gauge and a Convectron pressure gauge.

The volume of the vacuum system (chamber plus flanges plus Pyrex tube plus any fittings above the turbo pump gate valve) was determined to be approximately 12.92 liters using a calibrated leak as detailed in Section 3.8.1. The principle being that the calibrated leak provides a known influx of gas (atmosphere in this case) and by measuring the rate of pressure increase in the chamber as a function of time, the chamber volume can be calculated with some assumptions. The details of this procedure are given in Section 3.8.

## 3.5 Control System

The control system of PTX is more expansive than it is complicated. With 5 high speed optical control signals and over 12 low speed optical digital controls and 4 optical analog i/o nodes, the circuits for converting back and forth between electric

and optical systems is in itself expansive. In addition, a number of other custom and customized electronic circuits perform operations ranging from triggering the main spark gap switch, to engaging control relays, to measuring voltages. At the center of it all is a control computer running custom written software which monitors and controls the sequence of events that is required for PTX to operate correctly and safely. In the interest of a succinct description of the control system, many of these systems will be treated in groups where appropriate.

### 3.5.1 Computer for Operation of Software Controlled Systems

As already mentioned, PTX uses a standard computer running custom software in order to direct, control and monitor the experiment. The computer interfaces with the various electric components through the digital and analog i/o of the NI-FP system (see Section 3.5.2 for details on the NI-FP subsystem). The NI-FP and the computer in turn communicates over a fiber optical ethernet system to isolate the control room from the experiment. The software gives the operator control over the Spellman voltage levels and all the timing parameters as well as visual feedback in the form of live updating charts and computer dials on various status parameters such as main bank voltage levels, actual Spellman voltage outputs, plenum pressure and vacuum chamber pressure. The computer is connected to the PDG through a Universal Serial Bus (USB) and the PDG in turn distributes all of its timing and control signals through fiber optical connections.

### 3.5.2 National Instruments FieldPoint System

The NI-FP system is a modular system used in industry, typically for remote monitoring and control of hardware. It is designed for industrial environments and chiefly low-speed operations. As seen in Figure 3.11, the PTX lab uses an NI-FP1600 ethernet host with the following modules installed:

- 2 FP-DO-403 digital output modules, 8 channels each
- 1 FP-AI-100 analogue input module, 8 channels
- 1 FP-AO-210 analogue output module, 8 channels
- 1 FP-DI-301 digital input module, 8 channels

The digital and the analog channels interface with the rest of the experiment through optical connections. The ethernet connection to the controlling computer is provided by an ethernet to optical converter. The NI-FP runs off a dedicated Uninterruptible Power Supply (UPS) and the wall power connection to the UPS is lifted by means of a computer controlled relay prior to PTX running. This provides the safest possible environment for the control system by providing complete electrical isolation between it, the building and the rest of the experiment.

### 3.5.3 Berkeley Nucleonics Pulse Delay Generator

The PDG is used to provide timing and sequencing information by allowing pulses to be generated very accurately off of a trigger signal. The trigger signal is used to denote a "time zero" ($\tau_0$) reference and everything else is accurately timed off of this time. The temporal resolution of the PDG allows the operator to specify (positive)


**Figure 3.11**: The NI-FP system.

delays (from 0 to 1000 s) relative to $\tau_0$ as well as the width of the pulse (10 ns to 1000 s) in increments of 500 ps. The electrical outputs of the PDG in the control room are fed to a custom made, high speed electrical to optical converter which distributes the timing signals through high speed fiber optical cables. Both the custom box and the PDG can be seen in Figure 3.12. The initial trigger signal is provided (by means of a fiber optical cable) by the NI-FP at the time that the experiment should be "fired." Originally, once the trigger signal was received, the PDG would signal the puff valve to inject propellant, and after a short delay (typically 1200 to 2500 $\mu$s) depending on the experimental conditions, it simultaneously signals the Data Acquisition System (DAQ) and the spark gap switch driver. After the addition of the bias system, it was necessary to modify this sequence. Currently, when the trigger signal is received, the PDG first signals for the bias system to engage, then after waiting for $(4840 - \tau_{prop})\,\mu$s, where $\tau_{prop}$ is the time it takes for the propellant to travel from the puff valve down

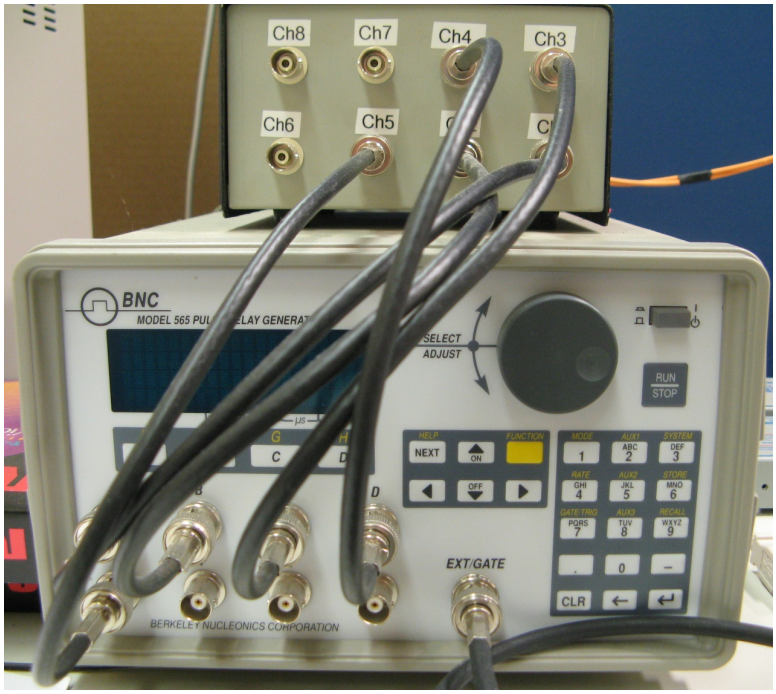


**Figure 3.12**: The PDG and custom optical converter box.

to the main coil, the PDG signals for the propellant to be injected. At $\tau_0 + 4840\,\mu$s the DAQ and main bank is fired, coinciding with the time that the pulsed bias system is at its peak and the maximal amount of propellant is underneath the main coil. For details on how the bias pulse delay times were determined, see Section 3.5.4.

### 3.5.4 Bias Coil Control

The introduction of a pulsed bias system to PTX had many and extensive effects on the experiment. From a control perspective it added complexity in terms of trying to accurately make multiple transient events line up and take place in a well coordinated manner. With the pulsed bias system, one has to accurately predict the time at which the pulse will reach its maximum and time the start of the pulse so

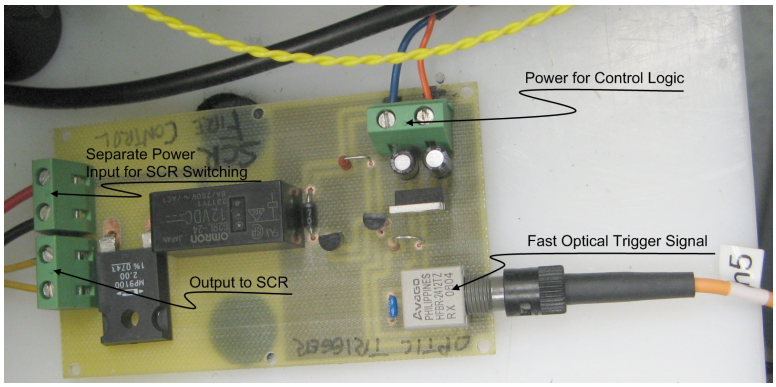


**Figure 3.13**: SCR trigger and switching circuit.

that the maximum coincides with the arrival of the propellant under the main coil. To achieve this, a new custom circuit was designed and built to trigger the SCR. The circuit can be seen in Figure 3.13. Note the various safety and control sub-systems of the bias coil system were designed and fabricated on standard FR4 Printed Circuit Board (PCB) material using Eagle CAD and an LPKF milling machine.

The bias system is switched by an SCR device, which is controlled by the above mentioned control circuit. This control circuit incorporates a mechanical relay which adds a time delay between receiving the fire-command through the fiber optic link and when the SCR actually conducts (and the bias capacitor bank is discharged into the bias coils). The time delay is not constant and was found to vary slightly between 4.80 ms and 4.82 ms. This jitter, 20 $\mu$s, is within the 200 $\mu$s window of opportunity provided by the nearly constant discharge peak. Figure 3.14 shows a representative oscilloscope plot which shows the optical trigger signal, the capacitor bank voltage, the discharge current and the relay response signal as oscilloscope channels 1 through 4 respectively. It should be noted that the bouncing nature of the relay does not seem

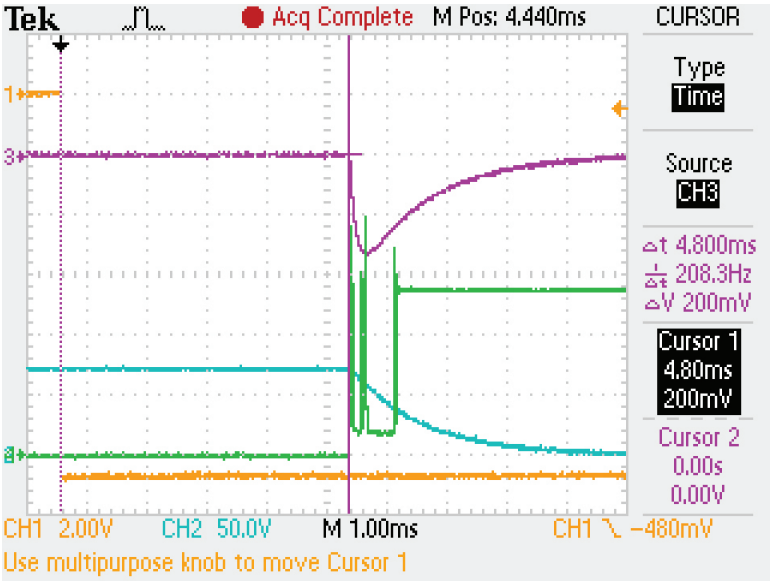


**Figure 3.14**: Relay timing and bounce profile. [A representative delay time for the system. Seen on channel 1 (orange) is the optical trigger signal, the capacitor voltage is seen as a light blue on channel 2, the current is displayed on channel 3 as a voltage (magenta, scale by 0.01 V/A to get the current) with the relay on channel 4 (green). As evidenced by the vertical cursors situated at the instant of the optical trigger and the time when current is first registered, the delay for this particular shot was 4800 $\mu$s]

to affect the discharge current profile *after* the SCR has been activated (*i.e.*, enough energy has been put into the triggering terminal of the SCR). It is suggested as a future improvement to replace the mechanical relay trigger with some other triggering mechanism. The main challenge in such an improvement lies in the conflicting need for rapid switching of a high current (several amps) medium voltage (12 to 24 VDC) while maintaining kV isolation between the triggering control, and the triggering source/SCR system.

The charging circuit consists of two relays for mechanical isolation between the primary (battery input) and secondary (capacitor bank) side of the voltage charging circuit. The voltage output depends linearly on the input voltage to the DCDC power

supply. The input is supplied by a battery and a manually adjusted rheostat prior to testing until the desired voltage is present at the output as verified by a direct multimeter measurement. The system was tested with repeated charge-discharge cycles both through the SCR switch and through the automatic and emergency safety dump systems. The maximal current peak in the bias coil depends directly on the charge-voltage on the capacitor at the time of fire and is measured during testing using a Pearson model 101 current probe. The system fires reliably for capacitor bank voltages at least down to 30 V DC and similarly no problems were observed switching voltages as high as 430 V DC. The capacitor bank itself is rated for operation as high as 450 V DC, but a safety margin was enforced to protect the capacitor bank. An example current profile for a discharge cycle (while the main PTX system was not charged nor fired and no propellant was injected) can be seen in Figure 3.15. Additionally, in Figure 3.4 the discharge profile during an automatic emergency dump is shown.

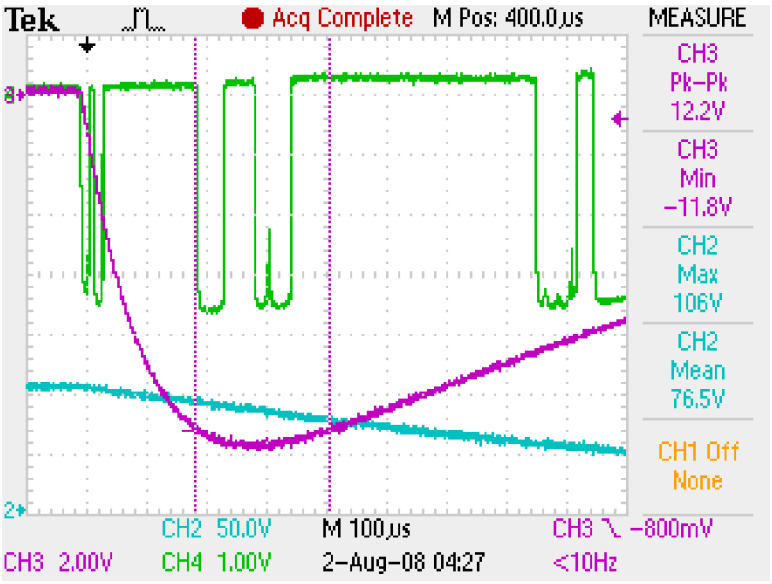


**Figure 3.15**: Bias current discharge profile. [A sample current discharge profile for the situation when the rest of the PTX experiment was not charged up and fired. As normal, Ch2 is the voltage across the capacitor bank, Ch3 is the Pearson probe measurement and Ch4 is the relay. Note that the event is zoomed in to show the relative flatness of the peak-current. The relatively flat area is indicated between the two vertical cursor markers and is approximately 220 $\mu$s wide. (The green plot of channel 4 shows the bouncing nature of the mechanical relay.)]

### 3.5.5 Interlock & Safety Systems

To ensure the safety of personnel and equipment while operating the PTX, several passive, manual and active systems are in place. The first line of defense is the pervasive use of mechanical relays arranged such that in their passive, de-energized state, they prevent power from reaching a component, from leaving a component or provide a direct path to ground, all depending on what function would provide the safest environment. Next is a group of 3 manual, spring loaded switches which need to be lifted and locked in place to allow the experiment to be operated, and finally there are the active parts, primarily the "Interlock and Emergency Abort"

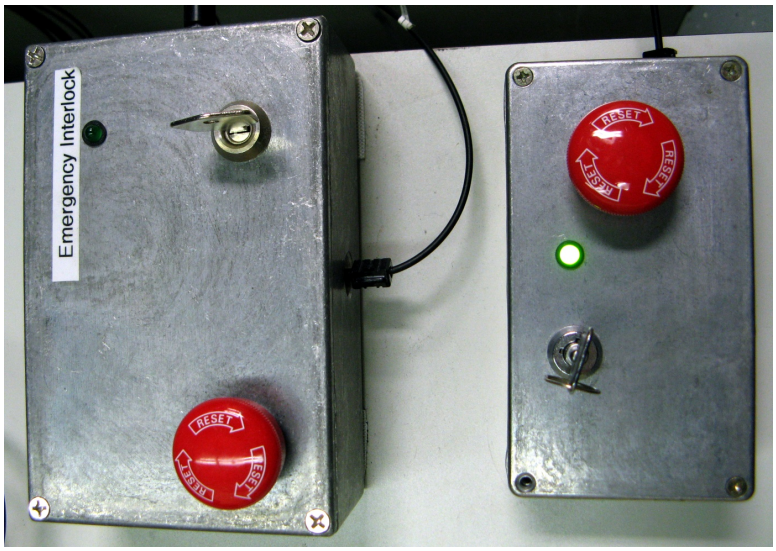


**Figure 3.16**: Emergency and interlock boxes.

boxes depicted in Figure 3.16. Both of these independent boxes have to be activated using keys before the NI-FP control lines become active. If the keys in both boxes are not turned on, or one box is missing, broken or disconnected, the NI-FP control is disabled resulting in a failure to energize the safety relays or run any part of the system. In addition to the keys, each box has a big red emergency stop button which if activated disables all NI-FP controls forcing all relays to their de-energized states thereby stopping the experiment with brute force no matter what part of the control sequence the experiment is currently in. The last line of defense is not as comprehensive nor as fool proof and is simply a side-effect of the passive system in that several key relays need to be energized in a particular sequence to enable operation of any of the high voltage components.

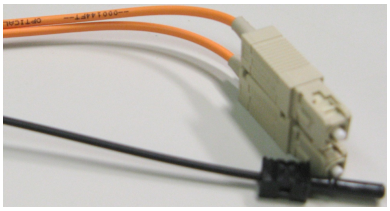

**Figure 3.17**: Sample of fiber optical cables.

### 3.5.6 Fast Optical (Timing) Control System

When it comes to time critical signals in the PTX, these are distributed using a mono-mode glass fiber optic cable. The optical transmitter and receiver for these cables have been carefully designed to provide maximal slew rate and the smallest response time possible. They can be used to accurately transmit sub-micro second pulses. The length of these cables is kept as close to identical as possible to ensure that signals are not skewed with respect to each other due to travel time. (At the speed of light, a difference of 1 ft corresponds to roughly 1 ns in travel time.) The type of fiber optical cables used are shown in Figure 3.17 in which the orange (top) cable is a "fast" glass fiber and the black (bottom) cable is a "slow" plastic fiber.

### 3.5.7 Slow Optical Control System

Any signal that is not time critical (*i.e.,* that is not required to be synchronized on a sub-millisecond scale) is transmitted with a cheaper (and more flexible) plastic fiber optic cable. These are used both for low speed, low resolution transfer of analog data and for transmitting and receiving digital (on/off) signals. The digital signals control the state of the various relays by opening or closing them as needed during the

experiment while the analog lines transmit data relating to the state of the experiment such as main bank voltage, plenum pressure and chamber pressure.

## 3.6 Data Acquisition System

The PTX DAQ system has several hardware platforms for digitizing analog data with sampling rates ranging from approximately 1 kHz for the analog input (AI) module of the NI-FP to rates of 1 GHz for the Acqiris DC270 modules. Counting the two bench top oscilloscopes normally used for troubleshooting and diagnostic, the lab has a total of 34 analog inputs available.

### 3.6.1 Acqiris High Speed Digitizer System

Of the 34 analog inputs in the lab, 20 can be found in the Acqiris box in the form of 4 modules of DC270's each with 4 inputs, and 2 modules of DC440's, each with 2 inputs. The DC270 modules digitize data at a rate of 1 billion samples per second with a resolution of 8 bits. The input range of each channel is software selectable from $\pm 0.25\,\mathrm{V}$ up to $\pm 2.5\,\mathrm{V}$ and the inputs can be configured to be AC or DC coupled with a $50\,\Omega$ or $1\,M\Omega$ input impedance. The DC440 modules have a maximum sampling rate of 400 million samples per second and a resolution of 12 bits. The coupling of the channel must be chosen in hardware and input impedance is fixed at $50\,\Omega$, but the input range is software selectable and covers a range from $\pm 0.125\,\mathrm{V}$ up to $\pm 5\,\mathrm{V}$.

The Acqiris modules are used to collect data during a normal experimental run. The Acqiris hardware is located very close to the experiment and is therefore

located inside a steel rack to electrical noise. Furthermore, since there is no optical isolation between the probes (located on the experiment) and the equipment, the Acqiris is powered by a UPS which gets disconnected from building ground prior to operation, same as the NI-FP system. This makes the instrument "floating" and reduces the chance of any spurious high voltages trying to reach ground through the instrument.

The Acqiris system is triggered by 2 independent (one for each group of modules, the DC270 and the DC440) high speed optical triggers. Normally both triggers are configured to be delivered at the same time to the Acqiris cube.

### 3.6.2 Computer for Data Retrieval and Archiving

The Acqiris system is connected to the PCI bus of a dedicated computer through a high-speed fiber optic data link. The computer has software which allows the operator to set and configure each input channel in the system as well as sampling rates, where the data is logged and with what file name. When data is acquired on the hardware, it gets stored locally on the hardware in a buffer. After the buffer is filled up, the data gets transferred over to the acquisition computer where it is saved to a mirrored pair of hard drives. The mirrored drives provide data redundancy in case of hardware failure in one or the other drive and is part of the data loss prevention system. (In addition, data is backed up to removable media at regular intervals during experimentation.)

### 3.6.3 Oscilloscope

The lab has 2 oscilloscopes which are primarily used for design debugging, troubleshooting and system characterization and calibration tasks. One of the oscilloscopes has an ethernet interface which allows it to be optically isolated (through an optical ethernet converter) and remote operated in the event that the oscilloscope is used during live operation of the experiment. Both oscilloscopes have the option of running on battery to further increase safety.

### 3.6.4 FieldPoint Slow Analog Input

The analog inputs on the NI-FP system are all optically isolated by converting the voltage to be measured into an optical signal proportional to the source signal. Because of the analog conversion from electrical to optical and back again, the system is more prone to inaccuracies and requires that the optical converters are calibrated in order to provide accurate results. Furthermore the NI-FP system is not designed to be a high speed digitizing system and as such the system overall is more suitable for relatively slow speed DAQ operations such as chamber pressure and other operational parameters of PTX.

The NI-FP system has been used successfully for various calibration options when the calibration procedure in question called for accurate relative time as well as multiple measurements. In these cases, the NI-FP analog input module was hard-wired to the probes and signals in question so as to avoid adding any uncertainty due to the optical conversions. Examples of such calibrations where the determination of

chamber volume and plenum volume as well as calibration of various pressure sensors. (The pressure sensors were calibrated on the NI-FP to ensure that any system specific biasing were properly included in the calibration.) Details of these operations can be seen in Section 3.8 and its sub sections.

## 3.7 Diagnostic System

The PTX used to have 3 types of main diagnostic probes: the $\dot{\mathbf{B}}$ and $\Phi$-loop array and the laser interferometer. With the addition of the bias field system, 2 new sensors were needed to fully characterize a shot with PTX, namely, the bias coil voltage and the bias coil current. The plenum pressure is a secondary measurement that is collected but this data is still acquired through the NI-FP adding some extra uncertainty due to the optical conversions.

### 3.7.1 The Interferometry System

To estimate plasma densities, the PTX experiment uses a Two Chord Quadrature Heterodyne Laser Interferometer hereafter referred to simply as the interferometer. This is a common instrument in the field of plasma diagnostics; it uses the Mach-Zehnder configuration, named after Ludwig Mach and Ludwig Zehnder who first invented it more than 100 years ago [53].

The Mach-Zehnder interferometer in its most fundamental configuration consists of a source of *collimated* light passing through a beam splitter (a beam splitter is also known as a half-silvered mirror). The two resultant legs are named "scene" and "reference," designated in Figure 3.18 as "SB" and "RB" respectively. When light

traveling in air hits the silvered surface of a mirror backed with glass, the reflected wave incurs a $1/2\lambda$ phase shift, where $\lambda$ is the wavelength of the light. Similarly, if $\gamma$ is the phase shift incurred by traveling through the optically denser medium of the mirror-glass, then if the light travels through glass before hitting the silvered surface, reflecting back out, the light will incur a total of $2\gamma$ phase shift, $\gamma$ going in and another $\gamma$ going out. So in the case shown in Figure 3.18 [54] but without the sample, "SB" at detector 1 will have incurred a total of $\frac{1}{2}\lambda + \frac{1}{2}\lambda + \gamma$ at the exit of the beam splitter. "RB", traveling a similar path incurs a phase shift of $\gamma + \frac{1}{2}\lambda + \frac{1}{2}\lambda$. As such there is no net phase difference between SB and RB at detector 1 and the light combines in perfect constructive interference. At detector 2, SB and RB have a $\frac{1}{2}\lambda$ phase difference and the two beams combine in perfect destructive interference. (To get to detector 2, SB adds up its phase shift as $\frac{1}{2}\lambda + \frac{1}{2}\lambda + 2\gamma$ while RB adds up as $\gamma + \frac{1}{2}\lambda + \gamma$.) When a sample is introduced in the path of SB, an unknown phase shift will be introduced and detector 1 will no longer have perfect constructive interference and detector 2 will not have perfect destructive interference [53]. By looking at how the sensor outputs change in the case with a sample compared to without the sample, it is possible with some difficulty to deduce the phase change incurred by the sample. The main drawback to this method is that the measurement is based off of the intensity of the light arriving at the detectors. This imposes a serious limitation on the sensitivity and accuracy of the setup, as the source of the collimated light (such as a laser) will have both random and systematic variances in the output intensity (amplitude), the detectors could have slightly different sensitivities, one detector could be

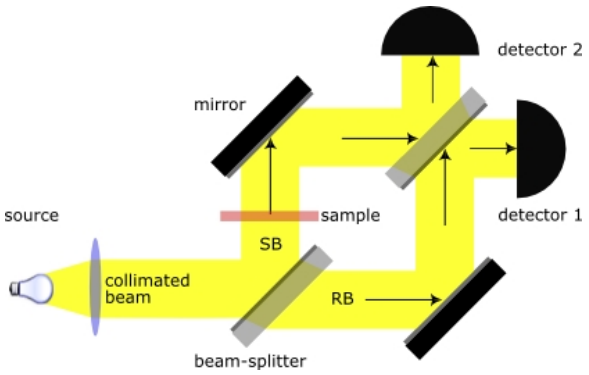


**Figure 3.18**: The original Mach-Zehnder interferometer setup. [Using collimated light [54].]

better aligned with the incoming light than the other and so on and so forth. These effects could degrade the sensitivity and accuracy of the setup.

To get around the most severe limitations of the Mach-Zehnder interferometer, several changes were made to the original arrangement [55]. The enabling technology to make these modifications is the acousto-optic modulator (AOM).

An example of an AOM is shown in Figure 3.19 [56]. The AOM works by applying a Radio Frequency (RF) signal to a piezo-electric transducer which is bonded to a suitable crystal or other optical medium. The piezo-electric transducer will thus induce an acoustic wave which travels through the crystal. This traveling wave will cause the local density in the crystal to change with time, in effect acting like a "phase grating" at the acoustic velocity of the material and with an acoustic wavelength dependant on the frequency of the RF signal. Incident laser light will be diffracted by this grating, which generally (depending on the type and construction as well as the positioning of the AOM) gives a number of diffracted beams [57].

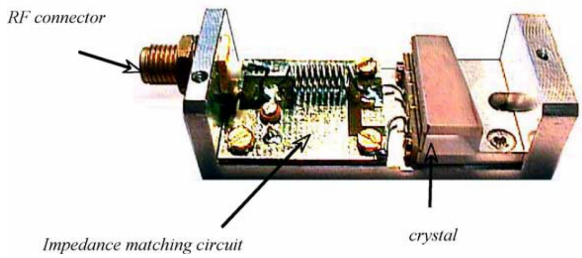


**Figure 3.19**: Overview of a sample AOM. [This is a labeled picture of an AOM. Taken from AA Opto-Electronic with permission [56].]

Depending on the design and engineering choices made during the construction of an AOM, it can have the following properties:

- Deflection -The angular deviation of the diffracted beam is proportional to the acoustic frequency. Deflectors are based on this principle.
- Amplitude modulation (Intensity) -The diffracted beam intensity is a function of the acoustic power. Modulators (q-switches) use this property.
- Frequency shifting -A frequency shift is introduced by the acoustic interaction ($\pm$ the acoustic frequency). So, any acousto-optic device can be used as a fixed or variable frequency shifter.
- Tunable Wavelength Filtering -Wavelength selection can be carried out with large spectral band sources since only one wavelength will match the Bragg condition, $2d\sin(\theta) = m\lambda$, $d$ is the distance between the planes in the media, $\theta$ is the angle of the diffracted wave and $m$ is the order of diffraction integer. The Bragg condition depends on the wavelength of the transmitted light, the incident angle and on the RF signal. This property is used in acousto-optical tunable filters wherein the frequency of the applied RF determines which wavelength passes through, while the amplitude determines the intensity of the transmitted light [57].

The Bragg interaction has four basic properties (as listed above) which are used in an AOM. Some of these properties are coexisting in all types of AOM's, *e.g.,* a modulator is also a fixed frequency shifter, a deflector can also be used as a variable shifter or modulator. What separates these devices from one another are various design

decisions and the resulting design strategies which are often contradictory to one another [57]. In the case of the PTX interferometer, the frequency shifting property of an AOM is used to create the reference and scene beam where the reference and scene beams are offset by a frequency $\Delta f = 40\,\text{MHz}$.

The reason for introducing this frequency shift into one of the laser beams is so that when the reference and the scene beam are mixed together, the difference (and the sum) of the two frequencies can be extracted. This is known as the heterodyne technique [58]. (The two resultant frequencies, the sum and the difference of the two mixed signals are called the "beat" frequencies.) This is done since it is far easier and actually practically possible to measure and quantify phase shifts on a 40 MHz signal compared to the frequency of the He-Ne laser light, $473\times10^{12}\,\text{Hz}$ which is far outside the range of modern equipment. This mixing technique is fundamentally the same as the one used in superheterodyne radio receivers. By choosing a lower AOM frequency, a cheaper DAQ or RF mixing system could be used at the expense of temporal density resolution while a higher frequency AOM can be used to get finer temporal resolution (on the changing densities) at the cost of more expensive DAQ or RF mixer equipment.

Through the AOM interaction and the heterodyne (the mixing of two frequencies to get the beat frequencies [58]) process, this allows the reference and scene beams to be combined into one beam and the phase information from both to be deduced from the output of only 1 sensor [58, 59]. The term "quadrature" refers to the fact that prior to analysis, $\frac{\pi}{2}$ is added to the Intermediate Frequency (IF, the AOM driver frequency) signal electronically or in post-processing. Then the IF (both the shifted and unshifted) is mixed with the detector signal. It is this shift that allows unambigu-

ous determination of the phase during 0 crossings as further discussed below [55, 58]. It should be noted that this phase change can be introduced *after* the mixed phase signal has been split up in its sine and cosine components during computerized data reduction, see Section 3.7.1.1 for more information on this. Alternatively, this can be done with analogue RF circuits prior to digitizing. In the case of the early version of PTX, the sine, cosine and phase shift signal processing was all done in analogue RF circuitry before the sine and cosine outputs were digitized. However, the experiment has since been modified to digitize the AOM reference frequency and the mixed phase signal directly, eliminating the electronic pre-processing and allowing the full analysis to be done digitally on a computer. This has some drawbacks associated with it in terms of increased complexity of the data reduction code, as well as the need to modify the code if either the cosine or sine term has a zero crossing, but it reduces the overall number of parts in the system thereby reducing the number of components that can fail. This approach is related to the one discussed by Weber in "He-Ne interferometer for density measurements in plasma opening switch experiments" [59].

In more detail, the drawbacks of the Mach-Zehnder setup have all been eliminated as outlined below. There are chiefly four drawbacks to the original design [55]:

1. Sensitivity nulls: the measured signal varies as the cosine of the phase difference $\phi$ between the scene and reference wave fronts at the surface of interference. As a direct consequence the measured signal will go to 0 when $\cos(\phi)$ goes to 0.
2. Ambiguous interpretation: As the signal passes through a maxima (*i.e.,* $\cos(\phi) = 1$), it is not possible to determine the sign of the derivative $\frac{d\phi}{dt}$ without additional information.
3. Calibration difficulties: environmental changes (vibrations, temperatures, drifts in the lasing source *etc.*) makes accurate calibration (determination of the

constant $k$ in $k\cos(\phi)$) very challenging and the calibration would need to be made within a few milliseconds of the actual experimental event in order to be of any value [55].

4. Competing effects of refractive bending: when the laser light passes through steep density gradients, the beam will be deflected, in some cases taking on a circular path profile. This changes the actual path-length traveled by the beam as well as possibly moving the beam off of the sensing axis, causing a drop in signal strength which would be impossible to distinguish from a variation in density.

The above difficulties and shortcoming have all been minimized or removed in the quadrature heterodyne interferometry setup by the following mechanisms [55]:

1. The zero-crossings are no longer a problem because there are two output signals in the setup, $C_1 = k\cos(\phi)$ and $C_2 = k\sin(\phi)$. As seen, when $C_1$ approaches a minimum, $C_2$ will be in its mid-range moving towards a peak and vice-versa. This allows the data to be analyzed using $\phi = \arctan\left({}^{C_2}/_{C_1}\right) + {}^{n\pi}/_{2}$.

2. By the same mechanism as above, the sign of the derivative $\frac{d\phi}{dt}$ can always be determined unambiguously.

3. The modified arrangement ensures that the constant $k$ has the same time variation in both signals when the signal amplitude is decreased due to refractive bending and other effects. Since the data analysis equation contains the fraction of $C_1$ and $C_2$, $k$ cancels out with itself and it is no longer necessary to determine its value through calibration.

4. Since refractive bending affects $k$ equally in both signals, the variations cancel out as stated above. The error introduced by the difference in path-length is normally less than the uncertainty of the beam-position in the plasma [55]. Additionally, in the PTX setup, the path-length is not likely to be significant enough to bring the scene and reference beams out of the coherence length which further decreases the error contribution from refractive bending.

The coherence length of a laser is given by

$$x = \frac{\lambda^2}{N\Delta\lambda} \tag{3.2}$$

and depends on the center wavelength $\lambda$, the refractive index $N$ of the transmission media and the spectral width $\Delta\lambda$ of the lasing source. The lasing source used in the PTX experiment is a Coherent™ He-Ne laser model 31-2108-000 (serial 1867DT) with a center wavelength of 632.8 nm and a spectral width of approximately $2 \times 10^{-12}$ m which with (3.2) results in a coherence length of $x \approx 7$ in rounded down. In actuality, it has been observed that the difference in path lengths needs to be less than about $x = 1$ in. (More modern laboratory grade diode lasers *can* have exceptional coherence lengths depending on their design. Traditionally, coherence length (through the center frequency parameter) have depended on the physical length of the lasing cavity, which for early diode lasers resulted in coherence lengths in the sub-millimeter range. More recent production techniques have apparently found a way around this and the Indigo DUV laser by Coherence™ claims coherence lengths $> 3$ m [60]; however, this particular model would be difficult to work with as it resides in the UV spectrum and thus is invisible to the naked eye and thus potentially dangerous. Additionally, longer wavelengths are better for interferometry, as will be seen in Section 3.7.1.2.)

In order to facilitate taking the measurement at two separate locations at the same time, the scene and reference beams are both split in beam splitters, giving 2 reference and 2 scene beams. This reduced the intensity in each beam by driving up the number of beam splitters from 1 (to recombine the scene and reference) to a total of 4. Of these, 2 were needed to produce the additional scene and reference beam, and 2 more were needed to recombine the two pairs of scene and reference beams. It should be noted that it *is* possible to set up heterodyne interferometers with unequal

path lengths, as long as the path lengths differ by some integral multiplier of the lasing cavity [61]. This concept could be very powerful in certain experimental setups in which the physical dimensions of the experiment require a long travel distance from the lasing source to the experiment sensing area. As the travel distance of the scene beam increases, the complexity of routing the reference beam in such a way that it matches the scene beam travel distance increases. Allowing the reference beam travel length to be independent of the sensing travel length could thus decrease the complexity and number of optical components required to meet the conditions of coherence. This technique is not currently used in the PTX setup because the current optical setup already works and the transmitted power in the reference section is sufficient. Another possibility for reducing the complexity of the optical setup is to acquire a laser with coherence lengths long enough that the path difference between the scene and reference beam falls well within the coherence length of the laser anyway, in which case the reference beam can be routed back to the mixing beam splitter in the shortest and most efficient way possible. Recent developments in continuous wave diode lasers such as the Indigo DUV by Coherence™ [60] and similar could provide a lasing source for an easy and effective interferometer setup.

The relative path-lengths of the two scene-beams and the two reference beams, hereafter referred to by $S_1$, $S_2$, $R_1$ and $R_2$ respectively, were initially measured using a high-resolution digital picture taken normal to the table surface. The picture shown in Figure 3.20 illustrates the beam-outlines, with additional color overlay added in postprocessing. The picture was analyzed and post processed using the software "Able Image Analyser" by Mu Labs™. By performing a spatial calibration using

the ruler (seen in picture) as a reference length, the software allows paths to be traced out and measured on the picture. The spatial calibration was determined by repeatedly performing the software calibration routine until the resulting conversion factors converged. The calibration was verified by measuring the distance between edges of the mount-holes on the optical table which are fixed in a 1 in grid pattern and also by measuring various distances on the reference ruler. Unfortunately, due to lens effects ("barrel effects") and other contributing factors such as the relative angle between the surface and the camera sensor, the accuracy decreases towards the edges of the picture. Because of these limiting factors, the approach was used to get the setup to have a path difference within a few inches. After this was accomplished, the traditional (and slower) method using rulers was used to bring the path differences as close to 0 as possible. The traced out and measured path lengths are shown with color overlays on the red beam. The $S_1$ overlay is yellow, $S_2$ is cyan, $R_1$ is green and $R_2$ is magenta. Again, attention should be given to the review given by Kumar on interferometry setups in which the path lengths do not need to be equal [61].

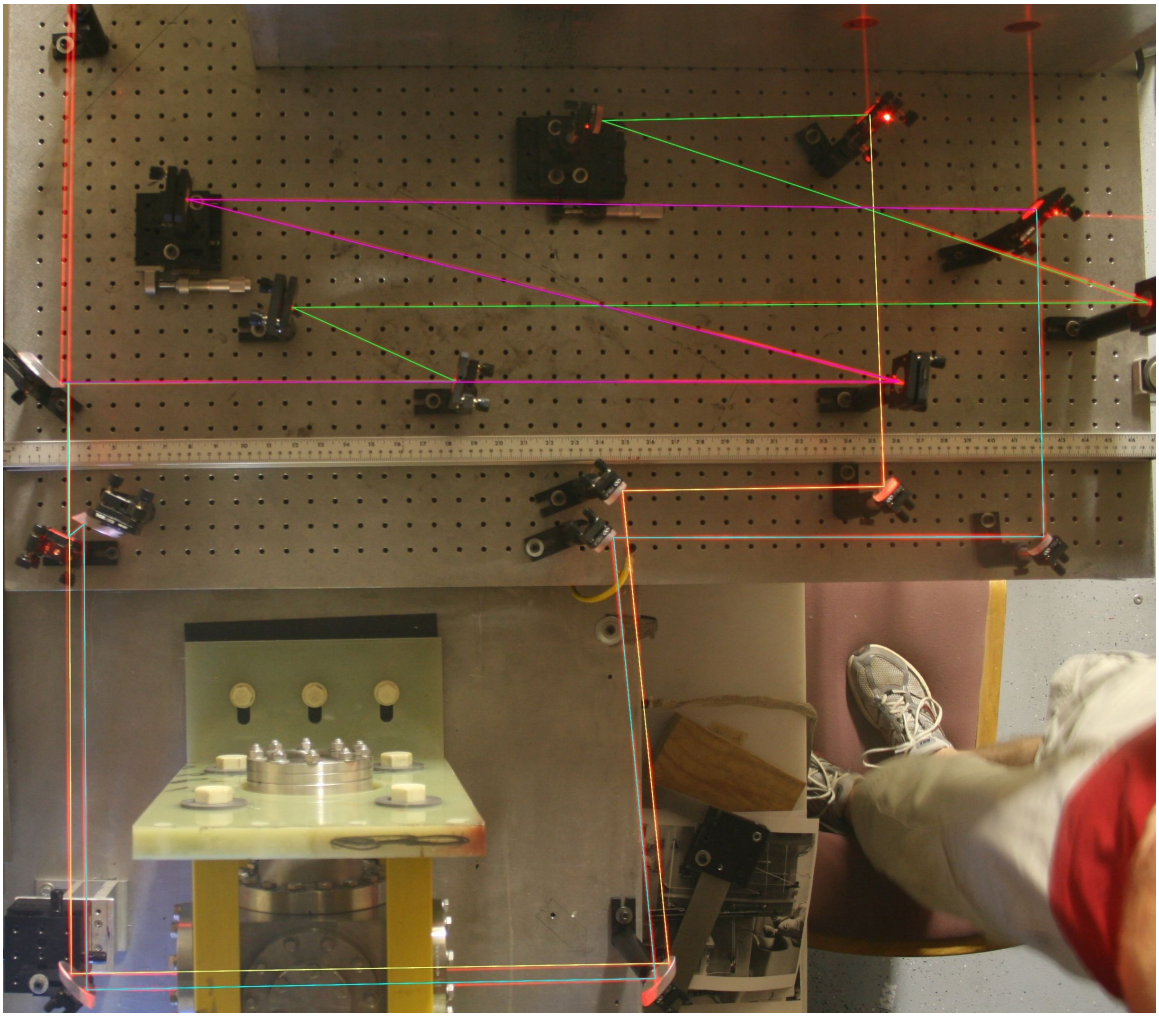

**Figure 3.20**: Interferometry path lengths with color overlays. [Measured path lengths using "Able Image Analyser" software. Certain sections of the laser have no overlay (and were not measured). These sections were not measured because the respective scene and reference beams both travel those sections together, and as such they travel the same distance. Since it is the path length *difference* that is of interest, these sections may be omitted from the measurements.]

#### 3.7.1.1 Extracting the Sine and Cosine of the Phase Mixed Signal

As mentioned in the previous section, the improved design relies on measuring a change in phase. At the detector level, this is represented by a time varying analogue voltage, $V_D$,

$$V_D = V_{D0} \cos\left(\omega t + \phi_{noise} + \varphi(t)\right) + V_{D1}\,, \tag{3.3}$$

where $V_{D0}$ is the base amplitude of the waveform, $\omega$, $phi_0$, $\varphi(t)$ are phase parameters and $V_{D1}$ is a dc-offset. Subtracting the vacuum baseline and rewriting using trigonometric identities then gives

$$V_D - V_{D1} = V_{D0} \cos\left(\omega t + \phi_{noise}\right) \cos\left(\varphi(t)\right) - V_{D0} \sin\left(\omega t + \phi_{noise}\right) \sin\left(\varphi(t)\right)\,. \tag{3.4}$$

The reference signal can be easily fitted to a simple cosine function,

$$R_0 = \cos\left(\omega t + \phi_{noise}\right)\,. \tag{3.5}$$

Shifting this 90° (since this was not done optically or with RF circuitry) then gives

$$R_{90} = \cos\left(\omega t + \phi_{noise} + \frac{\pi}{2}\right) = -\sin\left(\omega t + \phi_{noise}\right)\,. \tag{3.6}$$

Multiplying Equation 3.5 and Equation 3.6 by the baseline subtracted voltage given by Equation 3.4 then gives

$$M_0 = V_{D0} \cos^2\left(\omega t + \phi_{noise}\right) \cos\left(\varphi\left(t\right)\right) - V_{D0} \cos\left(\omega t + \phi_{noise}\right) \sin\left(\omega t + \phi_{noise}\right) \sin\left(\varphi\left(t\right)\right)\,, \tag{3.7}$$

and

$$M_{90} = -V_{D0} \cos\left(\omega t + \phi_{noise}\right) \sin\left(\omega t + \phi_{noise}\right) \cos\left(\varphi\left(t\right)\right) + V_{D0} \sin^2\left(\omega t + \phi_{noise}\right) \sin\left(\varphi\left(t\right)\right)\,. \tag{3.8}$$

Assuming that $\varphi(t)$ is a slowly varying function compared to $\omega$, where $\omega$ is the frequency of the lasing source, $473{\times}10^{12}$ Hz, integration of Equation 3.7 and Equation 3.8 over one period gives

$$\begin{aligned} I_0 &= \int_0^{2\pi/\omega} M_0 dt \\ &\cong V_{D0}\cos\left(\varphi(t)\right)\int_0^{2\pi/\omega}\cos^2\left(\omega t+\phi_{noise}\right)dt \\ &- V_{D0}\sin\left(\varphi(t)\right)\int_0^{2\pi/\omega}\cos\left(\omega t+\phi_{noise}\right)\sin\left(\omega t+\phi_{noise}\right)dt \\ &= \frac{\pi V_{D0}}{\omega}\cos\left(\varphi(t)\right) \end{aligned} \tag{3.9}$$

and

$$\begin{aligned} I_{90} &= \int_0^{2\pi/\omega} M_{90} dt \\ &= V_{D0}\sin\left(\varphi(t)\right)\int_0^{2\pi/\omega}\sin^2\left(\omega t+\phi_{noise}\right)dt \\ &- V_{D0}\cos\left(\varphi(t)\right)\int_0^{2\pi/\omega}\cos\left(\omega t+\phi_{noise}\right)\sin\left(\omega t+\phi_{noise}\right)dt \\ &= \frac{\pi V_{D0}}{\omega}\sin\left(\varphi(t)\right)\ , \end{aligned} \tag{3.10}$$

where $I_0$ and $I_{90}$ simply denote "integrated" 0 degree and 90 degree versions of Equation 3.7 and Equation 3.8 respectively. Assuming a small, compact plasmoid with a structural scale length of 1 cm traveling at 50 km/s, the rate of change in phase due to the plasmoid passing the scene beam would be on the order of $5\times10^6$ Hz which is arguably small compared to $473\times10^{12}$ Hz.

Next, divide $I_{90}$ by $I_0$ so that

$$\frac{I_{90}}{I_0} = \frac{\sin\left(\varphi(t)\right)}{\cos\left(\varphi(t)\right)} = \tan\left(\varphi(t)\right)\ , \tag{3.11}$$

then solve for the change in phase as a function of time

$$\varphi(t) = tan^{-1}\left(\frac{I_{90}}{I_0}\right). \tag{3.12}$$

If $\cos(\varphi(t))$ crosses zero during a plasma shot, Equation 3.12 would give a divide by zero discontinuity. If that is the case, one can use

$$\varphi(t) = \frac{\pi}{2} - tan^{-1}\left(\frac{I_0}{I_{90}}\right). \tag{3.13}$$

Long term noise from building vibrations and random density fluctuations in the air (due to thermal gradients from for example an AC duct) could potentially skew the measurements. To compensate for these and other unknown effects such as the *constant phase shift* introduced by the mirrors, beam splitters and Pyrex windows, a second order polynomial baseline is fitted to the surplus data captured prior to and after the plasma passes the interferometer chords. (It is thus implicitly assumed that there are negligible amounts of neutral gas in the scene legs during those time periods.) This baseline is then subtracted from Equation 3.12 or Equation 3.13, so that the final expression used to calculate the change in phase is

$$\Delta\varphi(t) = \varphi(t) - \varphi_{noise}(t). \tag{3.14}$$

It is this subtraction which does away with the need to know all the various but constant (on the time scale of the plasmoids, *i.e.,* $f \ll 5\,\mathrm{MHz}$) phase shifts introduced by the optical components.

Armed with this expression, it is time to take a look at how the change in phase is related to the quantity of interest, *i.e.,* the electron density $n_e$.

#### 3.7.1.2 Converting from Phase-change to Density

The diagnostic is a measurement of the phase change between the scene and reference beam. This is useful because of the interferometric property of the electrons and neutrals, namely, that the density is proportional to the index of refraction. Thus the voltage signal from each detector can be converted to a measurement of density.

To accomplish this, it is necessary to start with the "Appleton-Hartree formula for dispersion of electromagnetic waves through an ionized medium in the presence of an external magnetic field" [62] and the "Lorentz-Lorenz formula for refractive index for any gaseous mixture" [63]. From these two equations, it is possible to derive an expression for the change in phase of the light traveling through an ionized gas and similarly an expression for the change of phase created by the neutral gas. These expressions will be in the form of line-integrals and can be combined to give an integral expression for the change in phase. The Appleton-Hartree formula is given as

$$N^2 = 1 - \frac{X(1-X)}{1 - X - {}^1\!/_2 Y^2 \sin^2\theta \pm \sqrt{\left({}^1\!/_2 Y^2 sin^2\theta\right)^2 + (1-X)^2 \cos^2\theta}}, \qquad (3.15)$$

where $N$ is the index of refraction, $\theta$ is the angle between the $k$ vector of the light wave and the magnetic field, $X$ is given by $X = {}^{\omega_p^2}\!/_{\omega^2}$ where $\omega_p$ is the plasma frequency given by $\omega_p = \sqrt{{}^{n_e e^2}\!/_{m_e \varepsilon_0}}$ with $n_e$ as the electron density, $e$ as the electron charge $1.6 \times 10^{-19}\,\mathrm{C}$, $m_e$ is the electron mass $9.11 \times 10^{-31}\,\mathrm{kg}$ and $\varepsilon_0$ is the permittivity of free space $8.85 \times 10^{-12}\,{}^{\mathrm{F}}\!/_{\mathrm{m}}$. $Y$ is the ratio of the electron gyro-frequency to the lasing frequency $Y = {}^{\Omega}\!/_{\omega}$, where the gyro-frequency $\Omega = {}^{eB}\!/_{m_e}$ and $B$ is the magnetic field.

First, consider the Appleton-Hartree, Equation 3.15. The closed form solution of this equation depends on making the simplification that $\theta$ is either 0 or $\frac{\pi}{2}$. This is typically a valid assumption but should be kept in mind when setting up an interferometer. In the case of the PTX, there are two self-contained magnetic fields. One is a bias field which is $\frac{\pi}{2}$ with respect to the incident laser light, and one is a toroidal field which is assumed to be 0 rad with respect to the laser light. This assumption is valid for PTX as long as the gradient of the magnetic field is not significant over the width of the laser beam. Starting with the parallel case, $\theta = 0$ and using the above defined quantities $X$ and $Y$,

$$N^2 = 1 - \frac{X(X-1)}{1 - X - 1/2 Y^2 \pm 1/2 Y^2} = 1 - \frac{(1-X)}{(1-X)\frac{X}{1\pm Y}} = 1 - \frac{X}{1 \pm Y}\,, \tag{3.16}$$

and similarly in the perpendicular case, $\theta = \frac{\pi}{2}$,

$$N^2 = 1 - \frac{X(1-X)}{1 - X - 1/2 Y^2 \pm 1/2 Y^2} = 1 - \frac{X(1-X)}{1 - X - Y^2}\,. \tag{3.17}$$

If $Y \ll 1$, then both of the cases can be simplified into

$$N^2 = 1 - X = 1 - \frac{\omega_p^2}{\omega^2}\,. \tag{3.18}$$

Solve $Y$ with respect to $B$ using $Y = 0.01 \ll 1$ to determine the limiting value of $B$, $B_{max}$ for which Equation 3.18 will no longer hold,

$$B_{max} \leq \frac{0.01 m_e 2\pi c}{e\lambda} \approx 169\,\mathrm{T}\,, \tag{3.19}$$

using $\lambda = 632.8\,\mathrm{nm}$ and the speed of light $c$. The result in Equation 3.19 of 169 T (Tesla) is more than a factor of 100 higher than the maximal fields observed in PTX

and the approximations used to arrive at Equation 3.18 holds for PTX in its current state.

From classical electromagnetism, the wave number $k$ in an arbitrary medium is equal to $k = N\frac{\omega}{c}$. The total phase shift in the scene chord of a Mach-Zehnder type interferometer passing through an electron gas can then be described as

$$\phi = \int k\, dl = \int N\frac{\omega}{c}\, dl\,. \tag{3.20}$$

Since there will be a phase change, $\phi_{noise}$ from passing through the vacuum chamber due to the Pyrex windows in and out of the chamber as well as other more random effects, a second order polynomial baseline is fitted to the data available immediately prior to the plasma passing the interferometer chords as well as to the data available after the plasma is gone. Subtracting $\phi_{noise}$ from Equation 3.20 gives

$$\Delta\phi = \phi - \phi_{noise} = \int N\frac{\omega}{c}\, dl - \int k_{noise}\, dl = \frac{\omega}{c}\int (N-1)\, dl\,. \tag{3.21}$$

Equation 3.18 can be rewritten as

$$N^2 = 1 - \frac{n_e}{n_c}\,, \tag{3.22}$$

where $n_c = \frac{\omega^2 m_e \varepsilon_0}{e^2} = \frac{4\pi^2 c^2 m_e \varepsilon_0}{e^2 \lambda^2}$ defined as the critical density. Equation 3.21 then becomes

$$\Delta\phi = \frac{\omega}{c}\int \left[\sqrt{1 - \frac{n_e}{n_c}} - 1\right] dl\,. \tag{3.23}$$

For values of $\frac{n_e}{n_c} \ll 1$ a first order Taylor expansion of the integrand gives the following approximation

$$\sqrt{1-\frac{n_e}{n_c}} \approx 1-\frac{n_e}{2n_c}\,. \tag{3.24}$$

Since $n_c = 2.78\times10^{27}\,\mathrm{m}^{-3}$, $n_e$ up to the order of $n_e \approx 2.78\times10^{26}\,\mathrm{m}^{-3}$ can be measured without breaking the assumption of $\frac{n_e}{n_c} \ll 1$. A rewrite of Equation 3.23 results in

$$\Delta\phi = -\frac{\omega}{2cn_c}\int n_e dl = -\frac{e^2}{2\varepsilon_0 m_e c\omega}\int n_e dl\,, \tag{3.25}$$

or in terms of the wavelength, $\lambda$, of the interferometer

$$\Delta\phi = -\frac{e^2\lambda}{4\varepsilon_0 m_e c^2}\int n_e dl\,. \tag{3.26}$$

Note the dependance on the wavelength $\lambda$: the phase changes more for longer wavelengths.

Next an expression for the change in phase due to the light passing through a neutral gas must be derived. At this time it is worth pointing out that the change caused by ions in the medium can be neglected. This can be shown using 3 similar arguments:

1. When considering the effect of ions, $N^2$ will be given by $N^2 = 1-\frac{n_i}{n_c}$ in which $n_c = \frac{\omega^2 m_i \varepsilon_0}{e^2}$. Since the phase change is given as shown in Equation 3.20 and $N$ for ions will be on the order of 2000 times smaller than $N$ for electrons, the contribution due to ions can be neglected.

2. Ions do not have a significant polarizability compared to neutrals and free electrons and effects on the phase change will thus be small compared to those of neutrals and free electrons.

3. The electron density is proportional to the ion density. The neutral density is larger than the ion density and since the polarizability of ions is less than that of neutrals, the effect due to ions can be ignored.

The effect of ions on the polarizability $\alpha$ is negligible compared to free electrons and electrons bound in neutrals due to the comparatively large energy required for the remaining electrons in an ion to reach vibrational modes strong enough to change the polarizability noticeably.

Proceeding with finding an expression for the neutral contribution, starting with the Lorentz-Lorenz formula,

$$\frac{\varepsilon - 1}{\varepsilon + 2} = {}^{4\pi}/_{3}\alpha n_n \,, \tag{3.27}$$

$n_n$ is the number density of a neutral gas, where $\alpha$ is the mean polarizability, a tabulated property dependent on the gas species (see [64] for details on the polarizability of liquid and gaseous Hydrogen. See Nosov [63] for more general details on polarizability), and $\varepsilon$ is the permittivity. For non-magnetic materials $N$ and $\varepsilon$ are connected by the approximated Maxwell relation $N^2 \approx \varepsilon$ if the imaginary parts of $\varepsilon$ and $N$ are neglected [63]. The imaginary terms are loss terms which can be assumed to be negligible for under-dense gases. The resulting equation is

$$\frac{N^2 - 1}{N^2 + 2} = {}^{4}/_{3}\pi\alpha n_n \,. \tag{3.28}$$

Making the assumption that $N \approx 1$, which is justified by the fact that $N_{air} \approx N_{vacuum} \approx N_{dilutegas} \approx 1$,

$$N^2 - 1 = 4\pi \sum_i \alpha_i n_{n_i} \,, \tag{3.29}$$

where the summation is over all species in a mixture of gasses. Since PTX is mostly run on single-species gas, *e.g.,* Hydrogen, rewriting the equation for this case gives

$$N^2 = 1 + 4\pi\alpha n_n \rightarrow N = \sqrt{1 + 4\pi\alpha n_n}\,. \tag{3.30}$$

Performing a Taylor expansion (which can be done because of the above assumption of $N \approx 1$), the result is

$$N \approx 1 + 2\pi\alpha n_n\,. \tag{3.31}$$

Once more the relation $\Delta\phi = {}^{\omega}/_{c}\int(N-1)dl$ is employed, which when substituting in for the Taylor expansion of $N$ gives

$$\Delta\phi = \frac{2\pi\alpha\omega}{c}\int n_n dl = \frac{4\pi^2\alpha}{\lambda}\int n_n dl\,. \tag{3.32}$$

By combining Equation 3.26 and Equation 3.32, an expression for the change in phase as determined by both the neutral and the charged particles can be realized:

$$\Delta\phi = \frac{4\pi^2\alpha}{\lambda}\int n_n dl - \frac{e^2\lambda}{4\varepsilon_0 m_e c^2}\int n_e dl\,. \tag{3.33}$$

The mean polarizability $\alpha$ for a Hydrogen gas is $7.83\times10^{-31}\,\mathrm{m}^3$ [64], and so evaluating the constants in front of the integrals in Equation 3.33, again using a He-Ne $\lambda$ of 632.8 nm, gives

$$\Delta\phi \approx \left(4.88\times10^{-23}\,\mathrm{m}^2\int n_n dl\right) - \left(1.783\times10^{-21}\,\mathrm{m}^2\int n_e dl\right)\,. \tag{3.34}$$

Equation 3.34 directly gives the plasma density assuming that the plasma consists of a singly ionized Hydrogen gas so that $n_{ions} = n_e$. As can be seen from Equation 3.33, it is not possible to distinguish between $n_n$ and $n_e$ unless a laser with two different $\lambda$ lasing modes is used. Since $n_n$ goes as ${}^{1}/_{\lambda}$ and $n_e$ goes as $\lambda$, having two different

wavelengths passing through the same spot (and later separated by a prism in order to go to their respective detectors) will allow the unambiguous determination of $n_n$ and $n_e$. In the case of the PTX, this is an upgrade that could be implemented in the future based on the experiences of other 2 color interferometry setups like the one presented by Weber [65] in "A high sensitivity two-color interferometer for pulsed power plasmas." At present, the fact that there is also a sign difference between the two densities allows certain estimates as to the amount of neutral gas in the chamber to be made: As the plasma (which is assumed to be fully ionized) is accelerated downstream, it will collide with any neutral gas in the chamber and form a shockwave. As the front of this shockwave travels in front of the interferometer scene beams, the resulting line integrated densities shows a negative density (in PTX, Equation 3.34 has been multiplied by $-1$ to flip the signs so that the quantity of interest, *i.e.,* the electron density, shows up as a positive quantity) corresponding to the neutral gas being pushed in front of the plasma, followed by a much larger in magnitude positive density profile caused by the plasma passing the scene beam. By assuming that there is a very weak interaction between the neutral and charged particles across the shock boundary, and again assuming that the plasma is fully ionized, it can be reasoned that as soon as the signal swings positive, the measurement gives the electron density directly. To illustrate this, note the negative line-integrated density on Figure 3.21 between $t = 9\,\mu$s and $t = 11\,\mu$s.

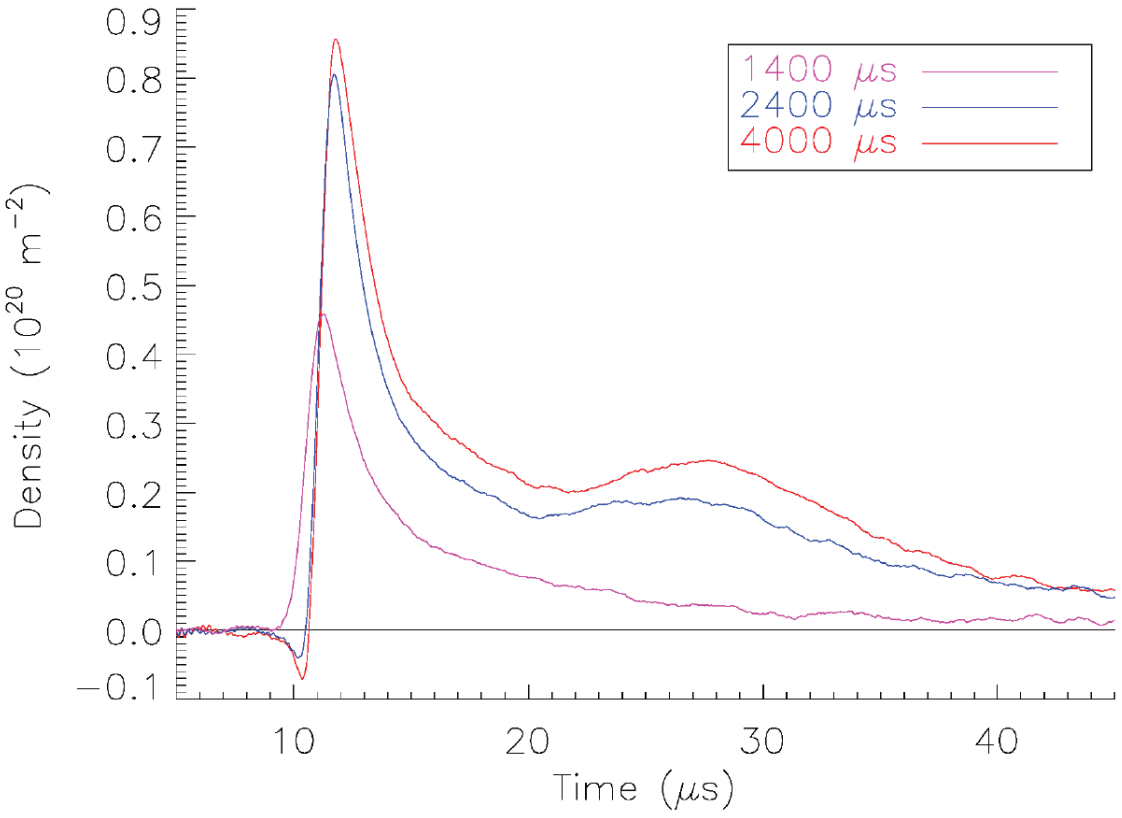


**Figure 3.21**: Interferometry density profiles as a function of delay times, taken from [1]. [The negative dip in the density is believed to be caused by the neutral particles being pushed in front of the plasmoid on a shock wave. The various plots shows how the density depended on the puff time.]

### 3.7.2 Bias System Pearson Probe

In order to properly quantify the characteristics of the bias magnetic field during experimentation, it is important to measure the current in the bias windings. This is done by using a Pearson Electronics current monitor Model 101, Figure 3.22. This particular model was chosen based on the expected bias circuit characteristics. The voltage output from the probe is proportional to the current that passes through the center of the probe according to $I = V_{output} \times 100\,\mathrm{A/V}$. The manner in which the

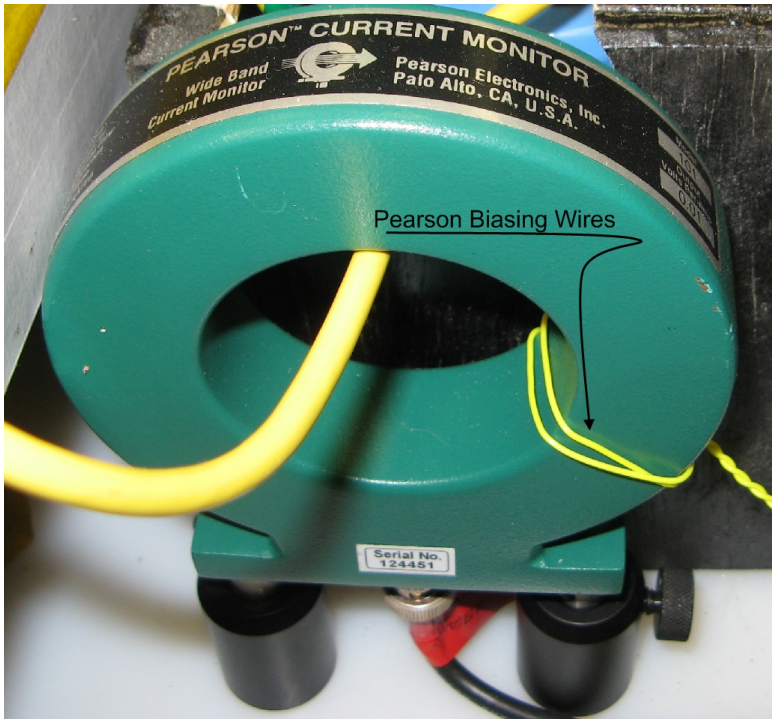


**Figure 3.22**: Pearson probe used to measure the bias system current. [Note the use of biasing wires on the probe to avoid saturation of the probe core.]

Pearson probe is designed makes it very applicable for this type of use. It is shielded from noise and is also totally shielded from the circuit on which it measures since it is not in physical contact with the test subject wire. This makes it safer for use around a high voltage system than a more direct approach. The probe can measure a maximum of 50000 A before experiencing a critical failure, but the main limiting factor for use on the bias system is its "current time product" of 2.5 A s. In pulsed measurements, the current time product is often the limiting factor and it should be noted that the specified 2.5 A s can only be achieved if a "core-reset bias" is applied. This is done by passing a low current in a wire wrapped around the probe as seen in Figure 3.22. For this usage, two loops and a current of 0.295 A is appropriate and necessary as

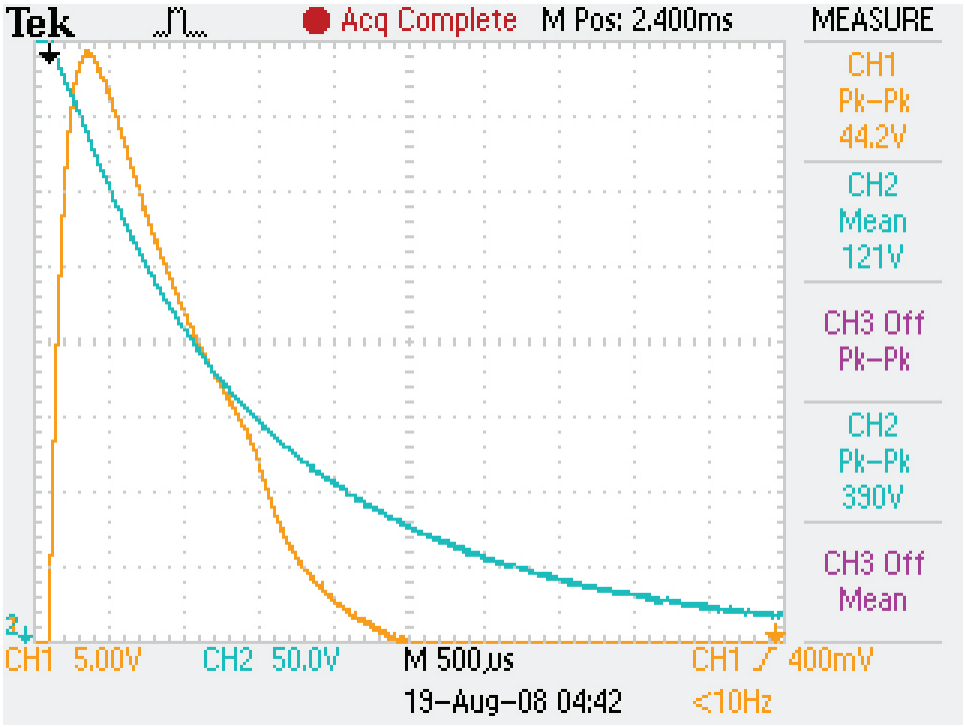


**Figure 3.23**: Saturated Pearson current probe signal. [The orange, "Ch1" plot shows an example of a saturated Pearson probe current signal. The probe was pre-biased as per the manufacturers recommendation, however the current time product of the captured event exceeds the probe's maximal specification and as such is driven into saturation. The point at which the probe transitions into saturation is relatively easy to spot as a discontinuity around 1500 $\mu$s. The teal colored "Ch2" plot shows the voltage across the capacitor bank. As seen on the oscilloscope screen shot, the y-axis is in units of volts.]

discussed in the "Bias application note" [66] on how to achieve full dynamic range during a pulse measurement. With proper biasing of the Pearson core, the current time product can effectively become larger than the specified 2.5 A s while the effect on the probe sensitivity due to this biasing is kept to less than 1 % [66]. Saturation occurs if the time integral of the current pulse exceeds the current time rating of the probe. This will force the core of the Pearson probe into saturation. When saturated, the probe output signal goes to 0 V in a discontinuous fashion, independently of the

actual current the probe measures. An example of a current trace where the probe is driven into saturation is shown in Figure 3.23. It should be noted that as long as the saturation occurs *after* the peak current, the indicated peak value will still be correct. This is important in this case since the peak value is the most interesting parameter during a discharge in the bias coil. In the figure, the total area under the current curve (with the readings converted to Amperes) was 5.70 A s, and as seen on the curve, the probe transitions from unsaturated to saturated around 1500 $\mu$s where the curve goes through a discontinuity.

### 3.7.3 Bias System Voltage Divider Probe

To safely measure the voltage drop across the bias capacitor bank during a discharge event, an insulated voltage divider was built so as to avoid accidental exposure to high voltages. The divider box was made using high-voltage certified components and has a divider ratio of approximately 400 when going into a 1 M$\Omega$ input impedance data acquisition terminal. The large divider ratio offers added protection to the DAQ in the event that a high voltage spike is coupled from the main coil into the bias coil and back down to the capacitor bank.

### 3.7.4 Propellant Reservoir (Plenum) Pressure Sensor

A propellant pressure reservoir section was implemented to reduce fluctuation in plenum pressure and to introduce a bleed-valve that can be used when it is desired to reduce the plenum pressure. The reservoir consists of a section of metal vacuum

pipe with appropriate fittings on it. (See Figure 3.6 to compare the reservoir in relation to the plenum volume.)

### 3.7.5 $\dot{\mathbf{B}}$ Probes

A $\dot{\mathbf{B}}$ probe measures the time derivative of a magnetic field by induction in $N$ loops of wire wrapped around a non-conducting, non-permeable core [67]. In the case where the magnetic field surrounding the probe is spatially uniform, the voltage induced in the probe can be expressed approximately as

$$V(t) = NA\dot{\mathbf{B}}\,, \tag{3.35}$$

where $N$ is the number of loops of wire, $A$ is the area of each loop and $\dot{\mathbf{B}}$ is the average time derivative of the magnetic field passing through the probe. During calibration, the $NA$ factor of each probe is determined using a Helmholtz coil to provide the spatially uniform magnetic field, a Wavetek model 278 0.01 to 12 MHz signal generator to introduce a time-variability in the magnetic field and a Pearson model 150 current monitor to measure the current. The Helmholtz coil used is described in [68]. By measuring the voltage output of the $\dot{\mathbf{B}}$ probe as well as the output of the current monitor using an oscilloscope, the calibration constant $NA$ can be arrived at as outlined below. Using the signal generator to drive the Helmholtz coil with a sinusoidal current of frequency $f$, the time derivative of the field near the center of the Helmholtz coil can be written as $\dot{\mathbf{B}} = \pm 2\pi f C_H I$, where $f$ is the frequency of the current driven into the Helmholtz coil, $C_H$ is a constant dependant on the size and

design of the Helmholtz coil (see below) and $I$ is the current being driven into the coil. Using this expression in Equation 3.35 results in $V_{\dot{\mathbf{B}}} = \pm 2\pi f C_H N_{turns} A I$ (here $N_{turns}$ is the number of turns). The ratio of field strength to current, $C_H$ for the coil used is $1.243\,^{\text{Gauss}}/_{\text{A}}$. The voltage output from the current monitor is related to current by $V_{Pearson} = C_P I$. $C_P$ for a Pearson model 150 monitor is $0.25\,^{\text{V}}/_{\text{A}}$ if the monitor is connected to a $50\,\Omega$ input impedance. Dividing the Pearson monitor voltage by the $\dot{\mathbf{B}}$ voltage results in

$$\frac{V_{\dot{\mathbf{B}}}}{V_{Pearson}} = \pm \frac{2\pi f C_H N_{turns} A}{C_P}\,, \tag{3.36}$$

and solving for $N_{turns}A$ gives

$$NA = \frac{C_P}{2\pi f C_H} \frac{V_{\dot{\mathbf{B}}}}{VPearson}\,. \tag{3.37}$$

The $\dot{\mathbf{B}}$ probes used were a modified version of the probes used by Fimognari [1]. The modification consisted of replacing the probe connection wires with finer gauge (see Figure 3.24, twisted wires and in the mounting process, the probes were mounted parallel to the Pyrex tube surface, as opposed to previously where the probes were mounted horizontally. These changes were necessary in order to allow room for the bias coil wires. The probes were re-calibrated after installation of the new probe wires and the calibration results are given in Table A.1 where probe number 1 is located at the throat of the Pyrex tube.

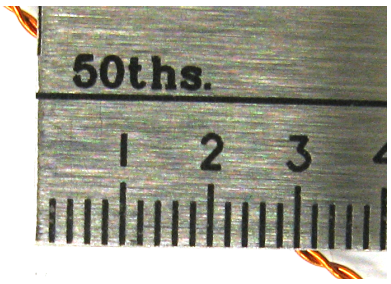


**Figure 3.24**: Close up of fine gauge $\dot{\mathbf{B}}$ probe wire. [The minor scale on the ruler is in $^1/_{50}$ in. The wire is approximately 0.01 in in diameter and can be seen going under the ruler around the 0.3 in mark.]

### 3.7.6 Φ-loop Probes

A Φ-loop is a single loop of wire wrapped around the Pyrex tube. The voltage developed due to induction in the loop depends on the time rate of change of the magnetic flux through the loop, $|V_{FL}| = \dot{\Phi}$. This means that for a vacuum shot, *i.e.,* when PTX is fired without injecting propellant, the voltage developed across a Φ-loop probe will be $V_{FL} = \pi r_l^2 \overline{\dot{B}_z}$, where $r_l$ is the radius of the flux loop. If gas is injected, a plasma shot, the expression for the flux loop voltage becomes

$$V_{FL} = \pi r_l^2 \overline{\dot{B}_z} - \Delta\dot{\Phi}\,. \tag{3.38}$$

## 3.8 Chamber Volume and Plenum Volume Calibration

In PTX it is important for the injected propellant mass to be well determined. The propellant mass injected into the system depends on the puff valve characteristics with respect to the open time or puff time ($\tau_{open}$), the plenum volume ($V_{plenum}$), the plenum pressure ($P_{plenum}$) and the propellant species. In order to determine the

puff valve characteristics and the plenum volume, it is first necessary to accurately determine the volume of the vacuum chamber ($V_{chamber}$) which is taken to be the combined volume of the Pyrex section, the steel chamber and any ports or attachments prior to the turbo pump gate valve.

### 3.8.1 Chamber Volume

The chamber volume was determined by using a calibrated capillary leak standard (Laco Technologies, model CM225.0-21008, S/N 2059) factory calibrated at 25 $^{\circ}$C and 1.0 atm with a temperature coefficient of 0.2 $\frac{\%}{^{\circ}C}$ and the leak rate was given as $4.79 \times 10^{-2} \pm 4.1\% \frac{atm\ cm^3}{s}$ into vacuum. When leaking into the vacuum chamber, the data collected for the calculations are all taken at pressures less than 1 Torr, *i.e.,* data collection is stopped before the vacuum pressure becomes significant relative to atmospheric pressure. This was done to motivate the necessary assumption that the leak rate is constant from vacuum up to the pressure where data collection is stopped. The procedure for determining the vacuum chamber volume was as follows:

1. Monitor ambient pressure and temperature during the test
2. Pump down the vacuum chamber to below the sensitivity range of the computer monitored sensor
3. Open the calibrated leak valve
4. Let the vacuum system come to equilibrium where the leak rate is balanced by the vacuum pump system
5. Start the data acquisition system to log the vacuum pressure and ambient pressure to a file
6. Close the gate valve between the vacuum pumps and the chamber

7. When the vacuum pressure has leaked up to the max range of the vacuum gauge (1 Torr), the data logging is stopped and the gate valve is opened, allowing the chamber to be evacuated.

The above steps were repeated several times for each session and multiple sessions were completed on different days. Before the chamber volume could be determined, correction factors due to temperature and ambient pressure were determined with

$$Q_{Tcor} = \frac{Q_{cal} C_T \left[T - T_{cal}\right]}{100\%} \tag{3.39}$$

and

$$Q_{Pcor} = K \left(P_{ambient}^2 - P_2^2\right) , \tag{3.40}$$

where the leak constant $K$ is given by $Q_{cal} = K\left(P_1^2 - P_2^2\right)$ with $P_1 = 1\,\text{atm}$ and $P_2 = 0$ (since it was factory calibrated leaking into vacuum) resulting in $Q_{cal} = K$, *but this only holds true if the pressures are in units of atmosphere, atm.* The final flow rate of the leak thus ends up as

$$Q_{cor} = \left(Q_{cal} P_{ambient}^2\right) + Q_{Tcor} , \tag{3.41}$$

where $P_{ambient}$ must be in units of $atm$.

Now that the corrected flow rate is known, the chamber volume can be calculated by using

$$V_{chamber}\,\text{cm}^3 = \frac{Q_{cor}\left(\frac{\text{atm cm}^3}{\text{s}}\right)\Delta t\,(\text{s})}{\Delta P\,(\text{atm})} , \tag{3.42}$$

where $\Delta P$ is the increase in pressure inside the vacuum chamber and $\Delta t$ is the time (in seconds) it took for the pressure change to occur.

**Table 3.2**: Results of the chamber volume data reduction

| Data Set | $\overline{Volume}$ (l) | Estimated Error (l) | $\overline{P_{ambient}}$ (atm) | $T_{ambient}$ (°C) |
|---|---|---|---|---|
| 21 Nov 2007 - 1 | 13.00 | 0.58 | 1.00 | 26 |
| 21 Nov 2007 - 2 | 13.02 | 0.59 | 1.00 | 26 |
| 23 Nov 2007 - 1 | 12.83 | 0.54 | 1.01 | 22 |
| 26 Nov 2007 - 1 | 12.87 | 0.57 | 1.00 | 22 |
| 26 Nov 2007 - 2 | 12.87 | 0.58 | 1.00 | 23 |
| **Average** | **12.92** | **0.57** | | |

The temperature of the room was measured on the surface of the calibrated leak intake filter using an IR thermometer and was found to be constant during the duration of each leak test. As such, the temperature correction factor was only calculated once for each set of data. Since the ambient pressure was continuously monitored along with the vacuum pressure, the pressure correction factor was calculated for each set of $\Delta P$ to give the "instantaneous" chamber volume. Later, all the "instantaneous" volumes were averaged and a standard deviation was calculated based on those averages. This was done for each set of data. The results from all data sets were then averaged to produce the final number for chamber volume along with the estimated uncertainty of the mean of all the sets (taken at different days).

The results of the various data sets are summarized in Table 3.2 while the complete data tables and correction factors for each test set can be found in Table A.2 through Table A.11.

It should be noted that the ambient pressure was measured with a gauge sensor calibrated with respect to 0 (by pulling a vacuum on it) and pressures at the local

airport (with the assumption that the weather macro cells have a constant pressure over the distances between the airport and the lab). After calibration, the transducer could be considered to work as an absolute gauge, and it tested to be in agreement with the airport readings to four significant digits of psia on several occasions.

### 3.8.2 Plenum Volume

With the chamber volume known, the plenum volume could be determined by puffing gas into vacuum at a PDG controlled puff time, $\tau_{open}$, with a measured plenum pressure and a measured vacuum pressure after the puff. The gas was allowed to come to an equilibrium after each puff, so the process can be assumed to be isothermal and the volumes involved are both constant so the plenum volume is directly related to the known parameters by the ratio shown in Equation 3.43.

$$V_{plenum} = \frac{V_{chamber} P_{chamber}}{P_{plenum}} \,. \tag{3.43}$$

It is important to note that all the pressures in Equation 3.43 are absolute pressures.

The plenum-pressure gauge is an Omega pressure transducer with a range of 0 to 50 psig. This transducer was calibrated using a dead-weight calibrator from 0 to 50 psig in steps of 5 psig (see Figure 3.25). It was then converted to an absolute pressure using a separate sensor to measure the ambient absolute pressure measurements. The conversion was made on a per sample basis.

For each value of $\tau_{open}$, 20 readings were taken, with each reading being an average of no less than 100 samples from the data acquisition system. The plenum

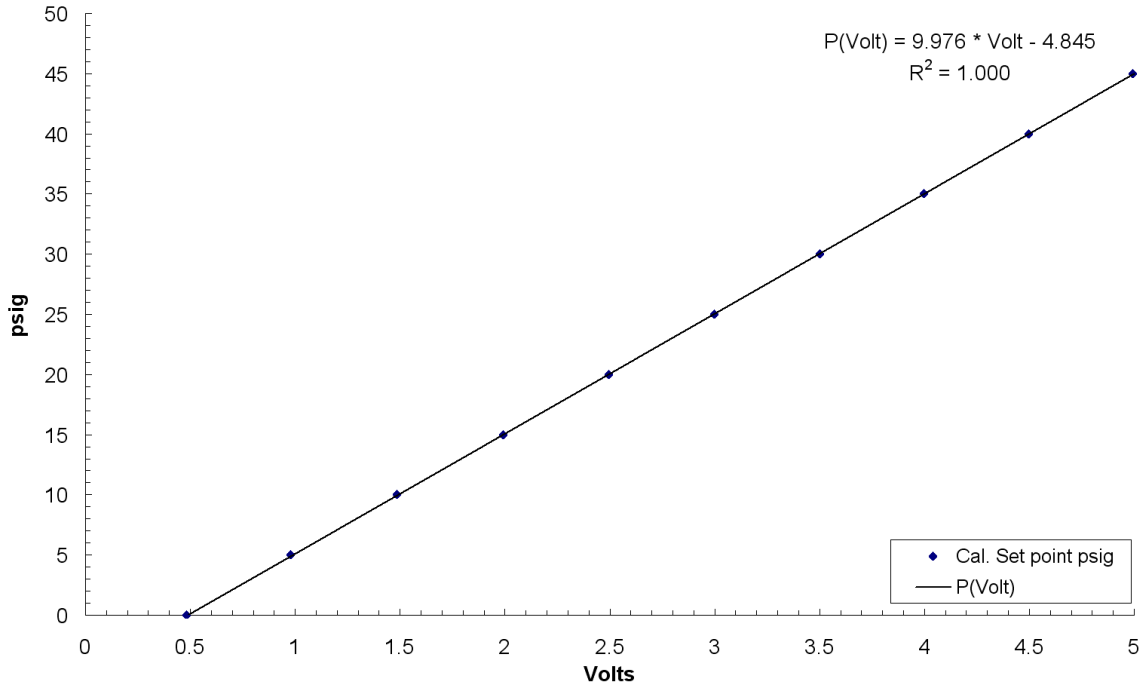


**Figure 3.25**: Plenum pressure calibration curve. [The calibration curve for the plenum transducer was determined based on data-points at 0 through 50 psig. Note that the horizontal uncertainty bars are present but invisible due to the scale of the axis. The largest uncertainty was $\pm 1.128$ mV.]

volume was calculated for each reading by using the zero-offset to get the corrected pressure for the first reading, and the difference between the current reading and the previous reading for all other points. The resulting volumes were then averaged and the standard deviation was calculated. This process was repeated for various values of $\tau_{open}$ with the range of values depending on the propellant-species being used. The "plenum volume versus $\tau_{open}$" for Hydrogen, Argon and Nitrogen are shown in Figures 3.26, 3.27 and 3.28 respectively, along with proper curve fits and uncertainty bars.

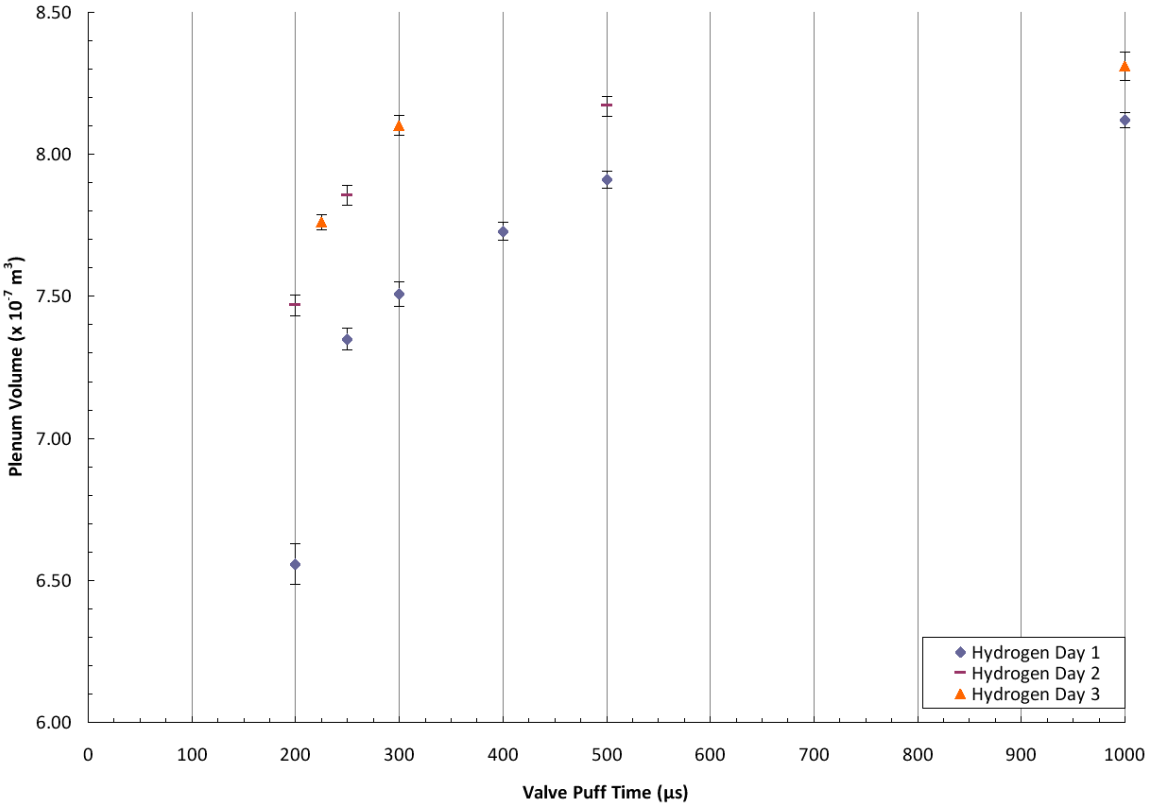


**Figure 3.26**: Hydrogen plenum volume curve. [Plenum volume versus valve puff time using Hydrogen. Note that the apparent error within each days data set is small but that the difference from one day to another is substantial.]

For the case of Hydrogen it was observed that the uncertainty in the determined plenum volume was low within the same data set (day), but there was relatively large deviations when compared to data points of Hydrogen from other days. This indicates that there is some unaccounted effect at play that varies between days. There are a number of things that could be ascribed to the observed day to day differences, including varying degrees of outgassing from the internal parts of the vacuum system (such as the Epoxy in the plenum), different temperatures, leaks (during the equilibrating time), inaccurate pressure readings, *etc.* The day to day repeatability was not

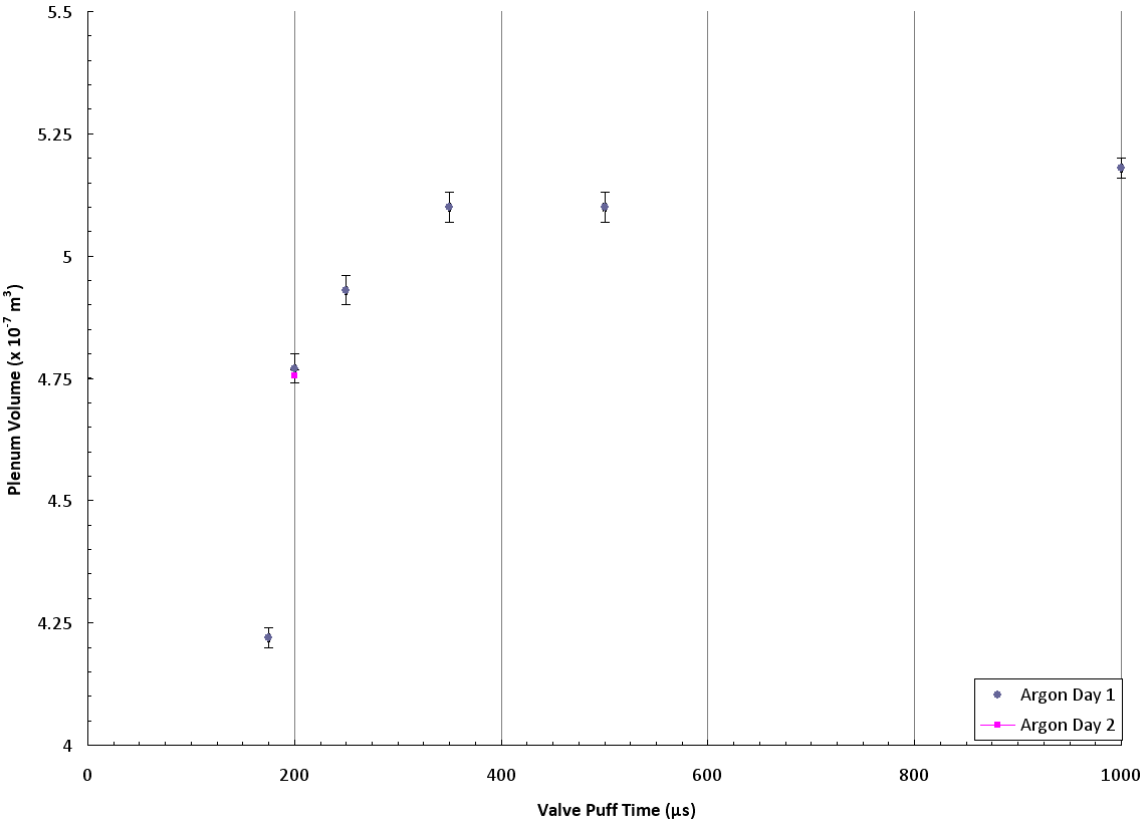


**Figure 3.27**: Argon plenum volume curve. [Only one setting was checked on day 2 for Argon and it was in strong agreement with the results obtained at a previous day for that setting.]

thoroughly investigated for Argon (only one setting was repeated on a different day, this point overlaps almost perfectly with the corresponding setting of the previous day) and not at all for Nitrogen. The main reason for a lack of repeated data for Argon and Nitrogen was time and resource constraints.

It was observed that part of the problem with this approach for determining the plenum volume is that the reference volume (the vacuum chamber) volume is much larger than the plenum volume ($10^1$ l versus $10^{-4}$ l). As such, even when filling the plenum to a high pressure (as high as 40 psi for the second day Argon test), the

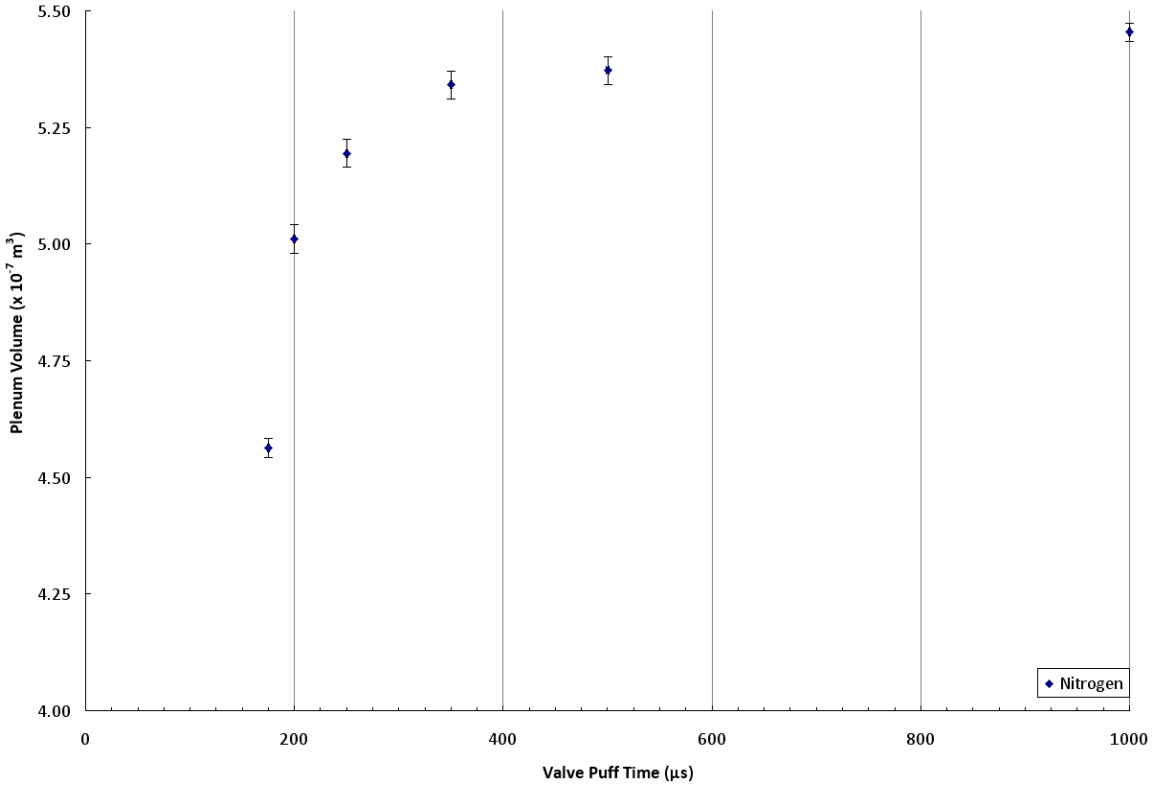


**Figure 3.28**: Nitrogen plenum volume curve. [Data for Nitrogen was only collected during one. As can be seen the curve exhibits the expected asymptotic dependency on the valve open (puff) time.]

resulting pressure change in the volume is low (80 mTorr range per puff for the Argon second day test). Since the change in pressure is very low, the system is inherently very sensitive to noise in the readings, any leak in the system and other factors like temperature. It is also more difficult to control the environmental parameters when using the vacuum system due to the number of flanges, probes, ports and accessories attached to it, and it would most likely be beneficial to use a smaller and more simplistic (*i.e.,* a section of pipe akin to the one used as a pressure reservoir) arrangement as the control volume.

A possible approach to more accurately determining the plenum volume would be to use a much smaller control volume. (This brings up the challenge of accurately determining the exact control volume value which would need a different calibrated leak standard with a slower leak rate.) Furthermore it might be beneficial to use positive pressures when calibrating the plenum volume and use existing ambient pressure as the 0 baseline *or* use an absolute pressure gauge. This would remove the need for measuring and compensating for the ambient pressure, and more conventional and accessible pressure gauges can be used to measure the increase in pressure as the plenum volume equilibrates with the control volume. Very high resolution pressure measurements can be achieved with standard off the shelf 1 psi gauges where each volt on the transducer output corresponds to 0.2 psi, especially when coupled with adjustable input range 12-bit DAQ systems already available in the lab. There are, however, at least two possible concerns with this approach in that the plenum valve and plenum volume might act differently under vacuum to the point where it will change the times it takes to vent all the propellant into the vacuum chamber. This effect can at least in part be minimized in the current setup where the existence of a fill valve allows the puff-valve to be left open for a much longer time, thus allowing all the gas to escape into the vacuum system. The other concern is that if the control volume is more comparable to the plenum volume and the puff valve is closed after partial equilibrium has been achieved, then it will not be possible to determine the plenum volume unless both the plenum pressure and the control volume pressure can be determined both before and after the puff. Due to the nature of the plenum volume, it is not possible to directly measure the plenum pressure unless it is connected

to the pressure reservoir. (Adding any known conventional pressure sensor to the plenum cavity would immediately increase the plenum volume by a factor of several hundreds.) This can be worked around by leaving the puff valve open after the puff, guaranteeing that the control volume equilibrates with the plenum volume. Once the plenum volume has been determined and the assembly put back on the vacuum chamber, a second set of tests can be run to determine approximate times needed to fully vent all propellant in the plenum.

# CHAPTER 4

# RESULTS AND ANALYSIS

*There is one thing even more vital to science than intelligent methods; and that is, the sincere desire to find out the truth, whatever it may be.*

—Charles Pierce

## 4.1 Overview

This chapter will provide an overview of the various processes and modifications attempted during the experimental phase as well as an analytical approach to explaining the observed behavior. Since the bias coil design on which this thesis was based turned out to be ineffective, the majority of the results presented will be analytical in nature, and the focus will be on interpreting and explaining these results and how they matched observed quantities in the lab. Although the current design iteration failed to increase the performance and efficiency of PTX, this does not constitute a scientific failure and the data and experience gathered during this phase of PTX have already proven valuable in guiding the near future design direction of PTX. At the very end of this chapter, a section has been included with some preliminary work on a possible alternate bias coil design which is believed to address the short-

comings of the current design and offer an overall better compromise between bias field coverage area and main coil field interference.

## 4.2 Troubleshooting

When the bias coil design was changed from an external DC system to an internal pulsed system, the implications of including inductors directly under the main coil was considered. The focus at the time was on how well the main field would couple with the bias coil and how much voltage would be inductively transferred from the main coil to the bias coil. The excluding properties of an inductor were largely assumed to be negligible due to the (forced) inclusion of large gaps between the turns in the coil which it was argued would be enough to allow most of the field to diffuse through between the windings. At the time of the design, the lab did not have access to a full version of QuickField™ and therefore a transient magnetic analysis was not performed on the setup prior to construction and implementation.

After installing the new bias coil wires onto the experiment, arcing was observed and located to be from one loop in the bias setup to the neighboring loop. The insulation in the first implementation consisted of Teflon-coated mylar with a voltage rating of 1200 V. This indicates that for some loops, the voltage differential between them is at least on the order of 2400 V. This further suggests a coupling from the main coil into (parts of) the bias coils of at least $^{2400}/_{50000} = 0.048$, or 4.8 %. This would be the absolute minimal coupling required for the arcing to occur; however, it is very likely higher than this. During the process of locating the source of the arcing (evident by a popping sound), it was noticed that leaving the bias coil wires uncon-

nected, or hanging in air, would force the developed potential towards infinity. This is because the energy coupled into the bias coil *has* to go somewhere and thus the induced voltage in the secondary coil (the bias windings) will increase until breakdown occurs at some point. In order to deal with the problem, additional insulation was used in the form of a plastic reinforced fiber-glass sleeving. The fiber-glass sleeving is by itself rated for 7000 V and as such the probable potential standoff value from one wire to the next will be a total of 16400 V when counting all the layers. This was found (empirically) to be sufficient for cases where the end wires on the bias coil were shorted together. Using this, a likely upper bound on the coupling can be determined as $^{16400}/_{50000} = 0.328$ or 32.8 %. It then follows that with a fixed resistance in the windings, a current will be induced in the bias wires dependant on the energy coupled from the main coil. Using Ohm's law, this current can be expected to fall inside of 3.33 kA and 228 kA using 0.072 Ω as the resistance (see Section 3.3 for details). These numbers will obviously be tempered by the available energy in the main capacitor bank, since no amount of coupling can transfer more energy into the bias coil than exists at the source. Since the coupling efficiency between the bias windings and the main coil is strongly dependant on the local geometric relationship between the two coil surfaces, the given ranges for coupling and induced current are worst case scenarios, but it seems reasonable to expect the coupling to be capable of driving an overall bias coil current of at least several kA as limited by the available energy in the main coil. Later on in this chapter, the significance of having even a relatively small current induced in the bias windings will be discussed as it prevents meaningful data from being obtained by the $\dot{\mathbf{B}}$ probes.

It was observed that the $\dot{\mathbf{B}}$ and Φ-loop probes did not give signals as observed in previous stages of the experiment. The signal levels observed were either very low or too close to zero to make any useful observations possible. In an iterative process, divider boxes then attenuators then mixer boxes and lastly the analog integrating circuits were taken out of the pre-DAQ system. After all external circuitry had been removed, a weak signal was finally observed on the Φ-loop probes, but the signal from the $\dot{\mathbf{B}}$ probes was still too weak to be useful. In the previous PTX setup, it was necessary to use both divider boxes dividing the incoming signal by a factor of 4 to 12 (depending on the probe location on the Pyrex tube) combined with further down-scaling in the mixer boxes and with attenuators to get the signal down to a level compatible with the DAQ system. During the process of removing more and more external circuitry from the setup, cables and probes were measured and checked to make sure that the cause of the weak signals was not due to faulty wiring or unconnected probes.

It should be noted that it is possible, albeit seemingly unlikely, that the wires for all the $\dot{\mathbf{B}}$ probes have been short-circuited at a point between the DAQ and the probe solder pads. If so, this consistent damage must have occurred after calibration and then most likely in the mounting phase. To give structural support and mitigate the risk of damaging the $\dot{\mathbf{B}}$ probes during installation of the bias wires and the mylar sleeve, an epoxy based putty was used. The putty does not fully enclose the $\dot{\mathbf{B}}$ probes but gives significant support to avoid any unintentional movement of the probe or the attached wires. Even so, due to the use of the fine gauge wires, seen in Figure 3.24, a short is still a possible explanation.

Having eliminated external (and internal) hardware as best as possible as the cause for the weak to non-existent probe readings, other explanations were sought after with the aid of a QuickField™ license. (QuickField™ is a commercial Finite Element Analysis (FEA) package which can be used to analyze thermal, electromagnetic and stress design simulations.) It was hypothesized that the presence of the bias coils suppresses field reversal inside the main coil volume, thereby inhibiting plasmoid formation. A validation license of QuickField™ was acquired for a period of 2 weeks, to set up and run several extensive transient models as detailed in the following section, in order to verify the hypothesis.

## 4.3 QuickField™ Transient Analysis

Existing PTX QuickField™ model files were used as a baseline for the new mechanical layout shown in Figure 4.1 and Figure 4.2. The old files were created in a previous version of QuickField™ in which only the magnetostatic solver was licensed. The mesh size was changed to allow for the capturing of skin depth effects in the main coil, drastically increasing processing time. However it was a necessary step for the transient analysis since a lower mesh density caused unstable solutions manifesting as magnetic field strengths growing towards infinity around sharp geometric boundary regions.

The mechanical model used was also modified to include the bias coil system. Due to the nature of the coil (sparse windings, few turns) the bias coil was modeled as individual loops connected in series (*i.e.,* the current is the same in each loop). The loops making up the bias coil were further divided up in 2 groups, the 2 x-point

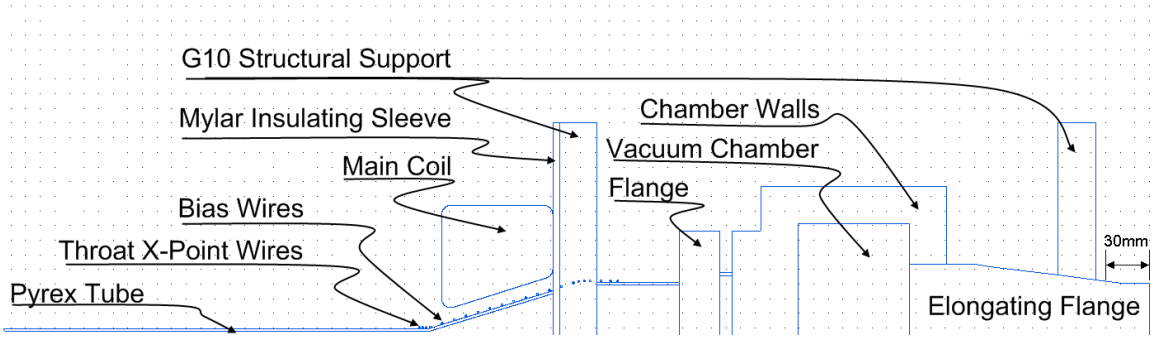


**Figure 4.1**: Overview of the QuickField™ model used. [The dot-grid in the figure has a spacing of 10 mm. The model assumes symmetry around the horizontal axis (the bottom of the figure). Except for the bias wires and the main coil, all other components in the model were assigned a permeability of 1 and a conductivity of 0 and were thus not affecting the results of the problems. These components were only included to show the physical dimensions of the experiment main components.]

sections at either end, and the main bias group, both seen in Figure 4.2. This allows the two groups to be defined with opposing current directions, approximating the real setup where the x-point sections are made by sharply reversing the loop direction of the wire at the transition point between the groups.

A series of test cases was run to test the hypothesis that the bias coils inhibit field reversal. Initially, magnetostatic (constant current) cases were studied. Such cases take very little computational time to run and they are therefore a good way to verify the problem model and setup. In addition the static cases will show the solution the transient cases would approach if time was taken to infinity. The next cases studied were transient cases of the magnetic bias field and how it propagates in the absence of the main coil field. These results were used to determine the initial field conditions present in the main coil volume at the time of onset of the main coil fields. Once these conditions were determined, a detailed transient analysis in which

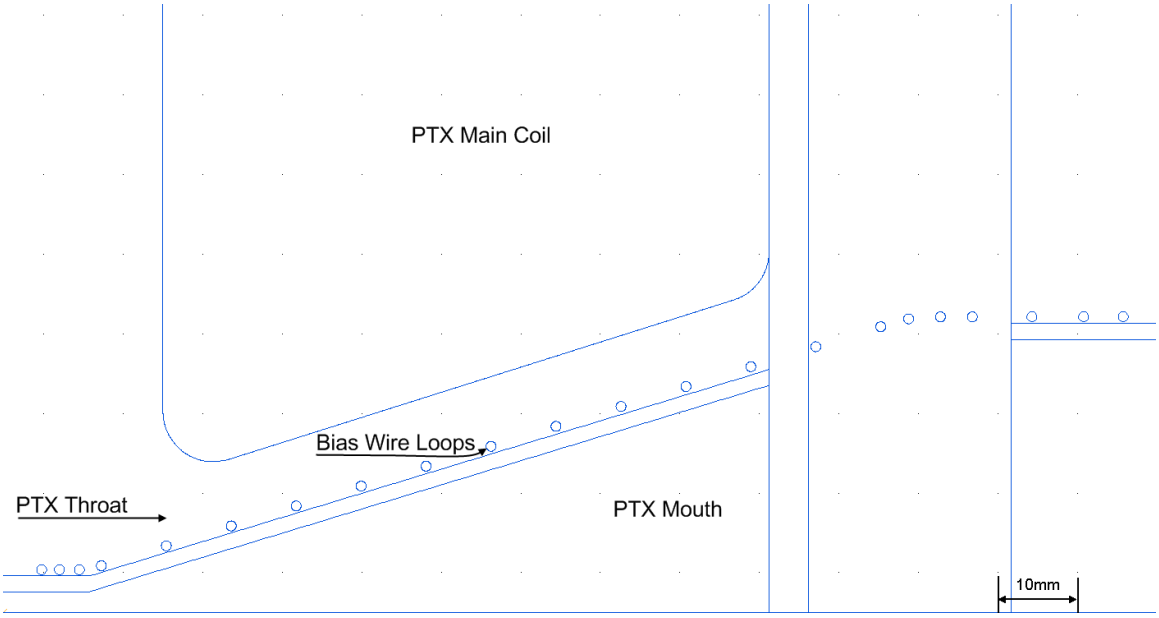


**Figure 4.2**: Closeup view of QuickField™ model of PTX near the coils.

the main coil fires both with and without the presence of the bias field were solved. Based on observations of the results of the above outlined test cases (discussed in more detail in the following paragraphs), a secondary set of cases was solved using a lower bias coil current to better distinguish between the effects of a conducting metal under the main coil, and the effects of competing and supporting magnetic field lines. After analyzing the results of the reduced current models, it was realized that the current design was fundamentally flawed and the first steps of an alternate design were tested in QuickField™ in which the pulsed bias coils were moved outside of the main coil volume. These cases were also initially run as static cases before solving for the initial conditions and finally doing the full transient analysis. The details of these test cases and the analysis of them are given in the following several sections.

Solutions were generated for both DC and transient cases both with the main and/or the bias coil(s) active. For the transient analysis, the bias coil current was set constant (assuming the transient effects of the slowly varying bias current would be secondary effects and could be ignored) while the main PTX current was modeled as an exponentially decaying sine wave with frequency and damping characteristics similar to a PTX discharge at a bank voltage of 35 kV. (By mistake the frequency of the damped current in the model was set to 200 kHz instead of 500 kHz; however, the analysis is still applicable since the lower frequency would compound the problems such that the herein given solutions are representative of a "worst case scenarios.") To further improve the simulation results, the transient analysis where both coils were active at the same time was run in a two step process to accurately set up the initial conditions existing at the time when the main coil fires (*i.e.,* that the bias coil current has peaked and will be mostly constant for the duration of the PTX main discharge). This was done in QuickField™ by using the same physical model and mesh file for two separate problems. The first problem was a transient analysis with only the bias field activated (with a constant current) and allowed to run from $t = 0\,\mu$s to $t = 200\,\mu$s which is approximately the time it takes the bias circuit to reach its peak discharge current. The time steps used for this initial phase were large ($25\,\mu$s) and only two of the time steps were saved ($100\,\mu$s and $200\,\mu$s), but the results are believed to be accurate as they show the fields moving towards the results obtained by running a magnetostatic problem with just the bias coils activated. The results for the last time step were used as the initial conditions to start the second problem which was set up to run from 0 to $10\,\mu$s relative to $200\,\mu$s, with a step size of 10 ns and output time in

100 ns increments. The finely spaced time-steps were used to capture the sinusoidal nature of the main discharge current with great detail and the frequent saving of the results allowed for a detailed study of how the transient field behaves as it goes from maxima through nulls and on to the minima points on the sinusoidal current wave.

Starting out, 2 DC cases where run, 1 with just the bias coil active and one with both the coils active. 50 kA was used as the (static) current for the main coil. The DC simulation in Figure 4.3 indicates what the field geometries would approach if the current was kept constant for an infinite time. Comparing the DC case with only the bias coils active as seen in Figure 4.4, to the bias transient case at the 200 $\mu$s time step as seen in Figure 4.5, it can be seen that the transient field is in the process of soaking into the main coil, approaching what the DC case shows.

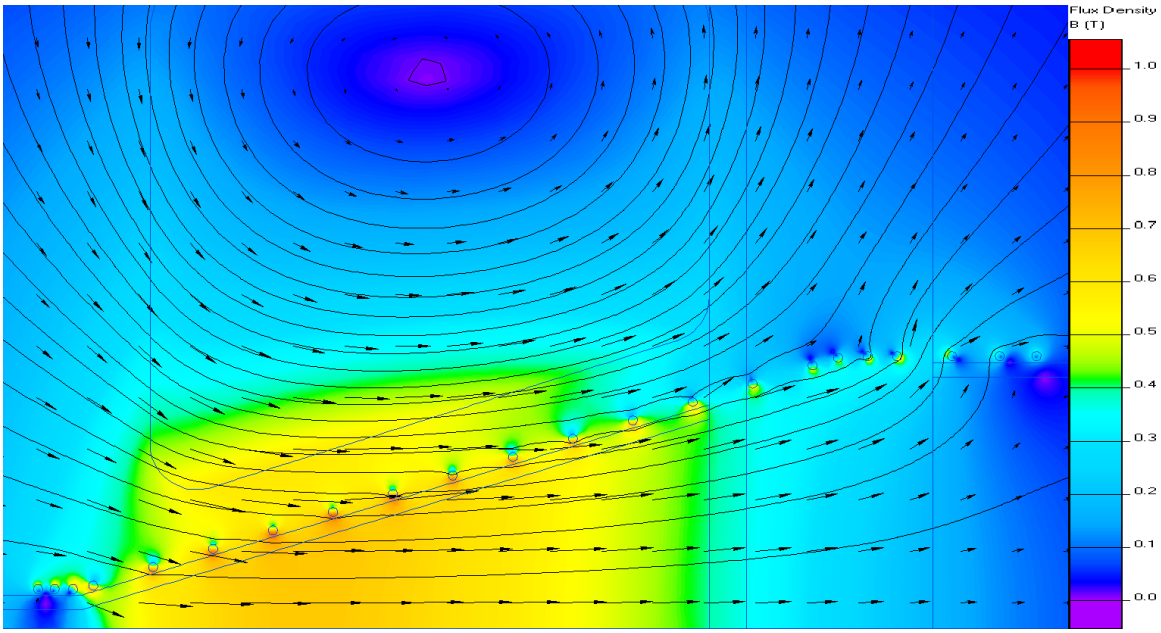


**Figure 4.3**: Magnetostatic results with a static bias and main coil current. [The color map shows the magnetic flux density as per the legend on the right and the vector arrows shows the direction of the magnetic flux. For this simulation, the current in the x-point sections were -1 kA, the current in the bias section was 1 kA and in the main coil it was 50 kA. The maximal field strength was 0.922 T.]

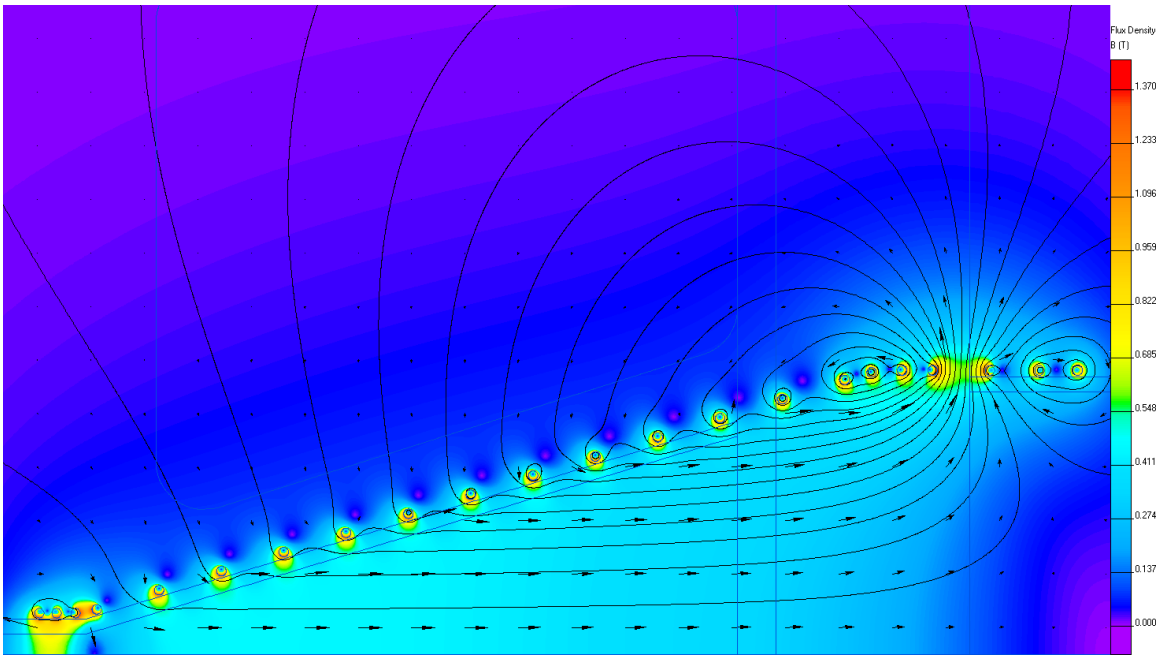


**Figure 4.4**: Magnetostatic results with a static bias coil current. [The color map shows the magnetic flux density as per the legend on the right and the vector arrows shows the direction of the magnetic flux. For this simulation, the current in the x-point sections were -3 kA and the current in the bias section was 3 kA. The maximal field strength was 1.37 T.]

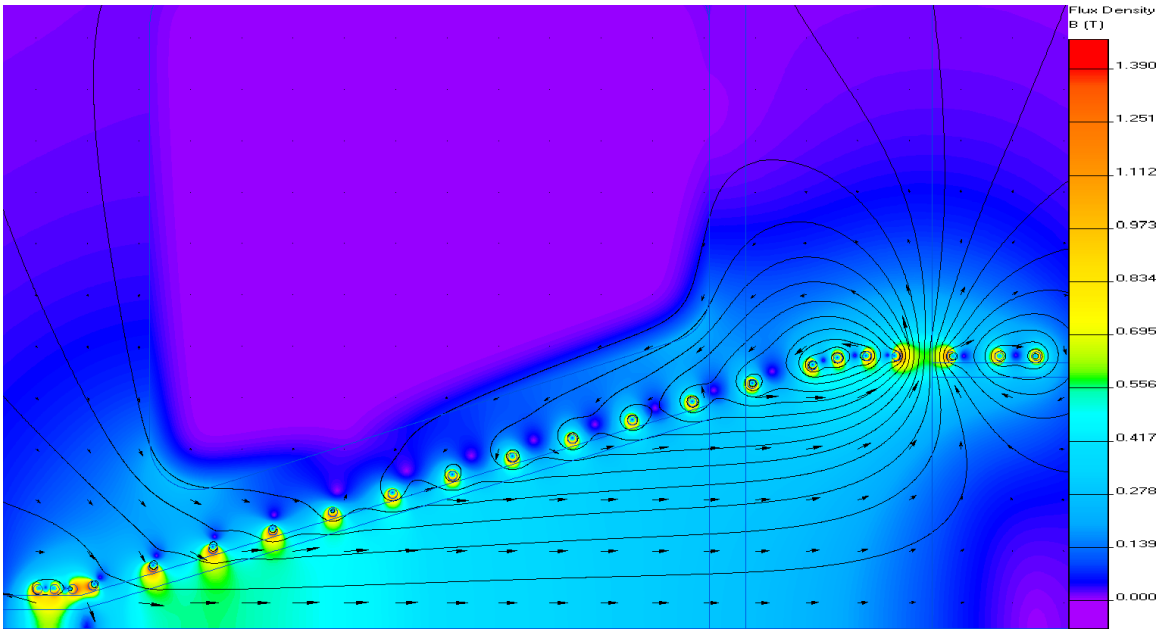


**Figure 4.5**: Transient results with a static bias coil current. [Results of a transient analysis at time $t = 200\,\mu$s. As can be seen, the magnetic field has started to soak into the material of the main coil as was seen in the DC cases. The maximal field strength was 1.37 T and the bias and x-point coil currents in this analysis also, was $\pm 3$ kA respectively.]

Next, a transient analysis in which the bias field current had been set to 0 A was run to determine how the presence of the bias coil wires affect the sinusoidally dependent magnetic field. In a transient (or AC) problem, the material properties of the conductors become essential to the solution. For all the transient problems, the material properties used for the coils were $59.6 \times 10^6\, S \times m^{-1}$ for the copper bias windings and $37.8 \times 10^6\, S \times m^{-1}$ for the aluminum main coil [52]. As it turned out, the mesh size used during this simulation introduced chaotic field lines in the immediate vicinity of the main coil current zero crossings Figure 4.10. The collapsing field lines in the FEA are visible as a myriad of chaotic field lines inside of the main coil. The most likely culprit of this phenomenon is numerical truncation errors combined with a finite mesh size. Of considerable interest is the fact that the presence of the bias wires when no current flows in the wires seems to have only a minuscule effect on the main magnetic field. In fact, when studying Figures 4.6, 4.7, 4.8 and 4.9 in which there is *no current in the bias coil wires*, the main field both soaks through the bias windings and into the Pyrex tube *and* reverse direction when the current in the main coil reverses direction. With the current mesh density and running the simulation up to 10 $\mu$s, the model requires a wall clock time of 3 days using an AMD Opteron dual core computer with 2 GB of memory.

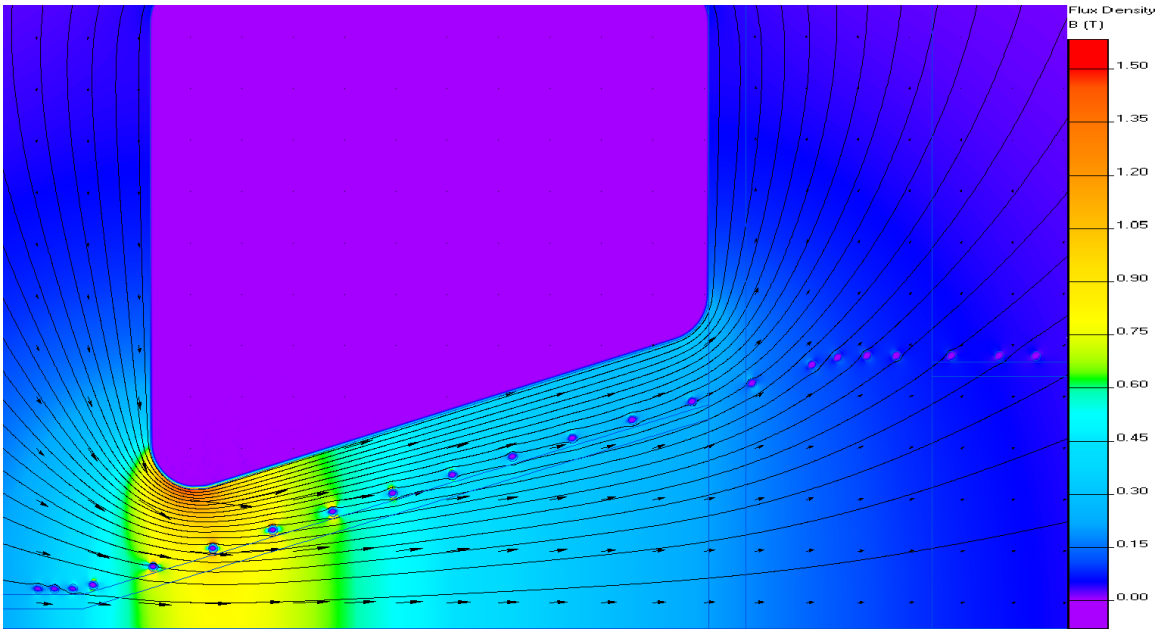


**Figure 4.6**: Transient results of the main coil at the first peak at $1\,\mu$s. [ The results of a transient analysis with only the main coil active at time $t = 1\,\mu$s. As can be seen, the magnetic field seemingly has no trouble penetrating the bias windings and the field topology is only locally affected close to the bias wires.]

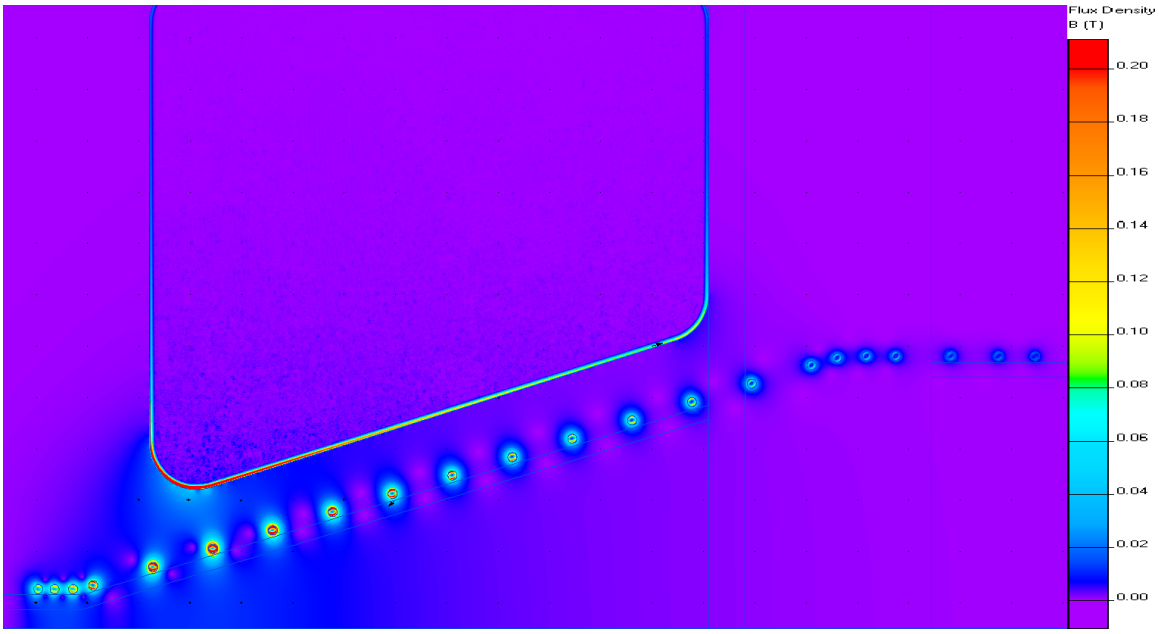


**Figure 4.7**: Transient results of the main coil at the first zero crossing at $2\,\mu$s. [Results of a transient analysis with only the main coil active at the first zero crossing at time $t = 2\,\mu$s. As can be seen, there are some indication of collapsing field lines inside the main coil.]

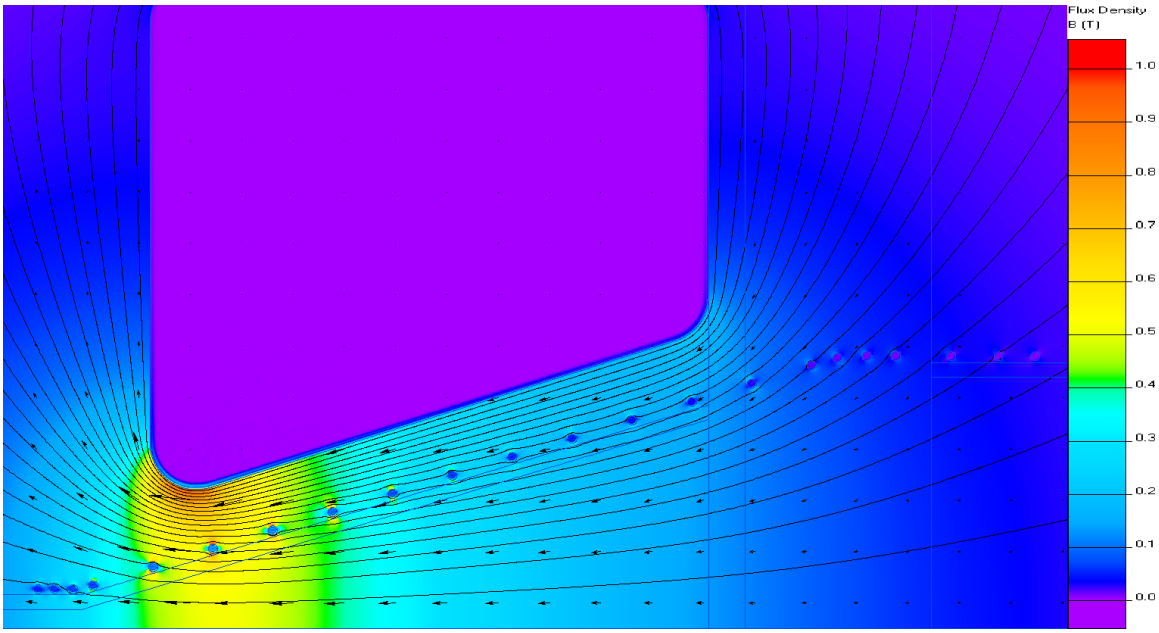


**Figure 4.8**: Transient results of the main coil at the first negative peak at $3\,\mu$s. [Results of a transient analysis with only the main coil active at the first negative peak at time $t = 3\,\mu$s. As can be seen, the field has reversed direction inside of the Pyrex tube, a necessary condition for the formation of a plasmoid.]

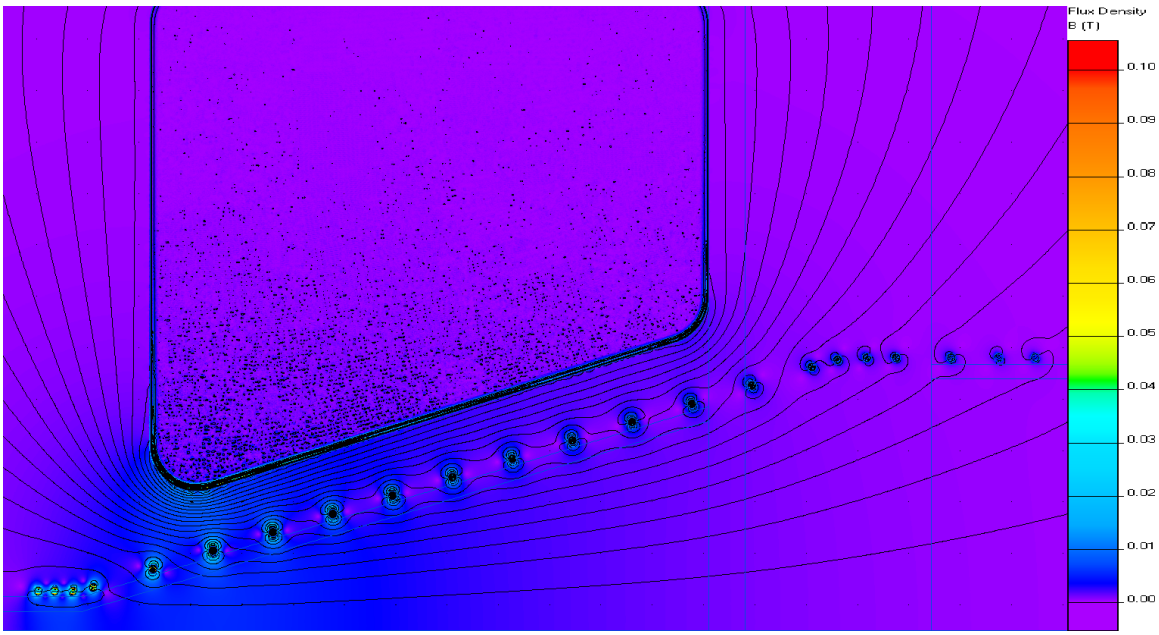


**Figure 4.9**: Transient results of the main coil at the second zero crossing at $4\,\mu$s. [Collapsing fields at the zero crossing at $t = 4\,\mu$s is even more apparent at this time step.]

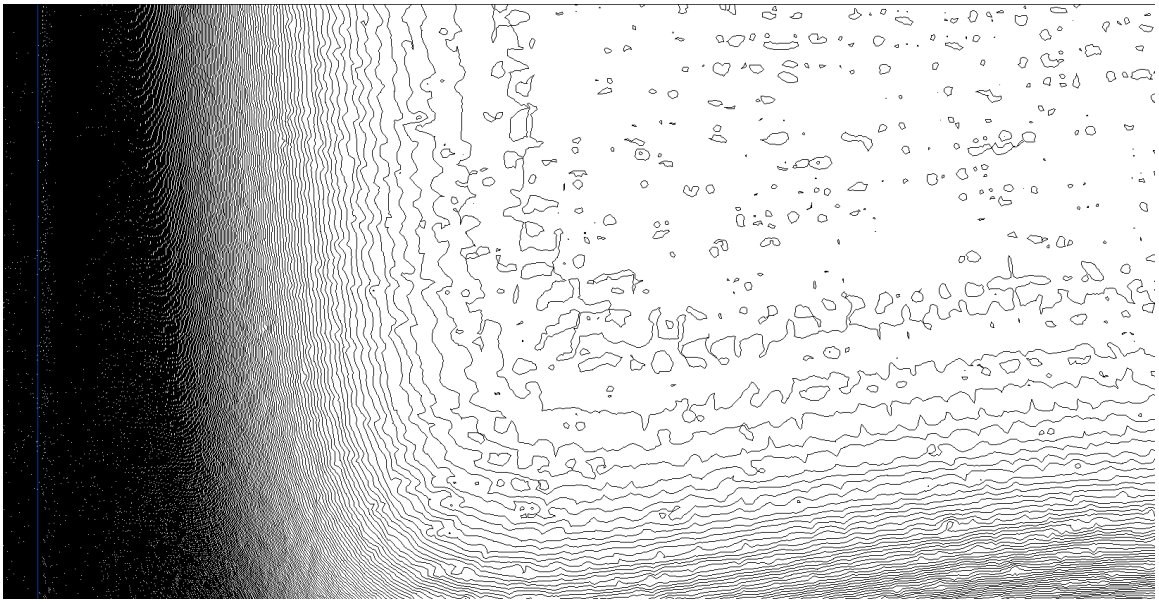

**Figure 4.10**: Extreme close-up of the collapsing fields at $4\,\mu$s. [Along the left side the blue line of the left edge of the main coil can be seen. The black lines represent magnetic field lines. Note the chaotic structure of the field lines as no current is flowing to uphold the fields.]

When looking at the results of the transient analysis with both the bias and the main coils active as seen in Figures 4.11, 4.12, 4.13, 4.14 and 4.15, it was observed that the combination of current carrying copper bias wires and the fields they generate, severely affects the penetration –depth and –strength of the main magnetic field. This is in contrast to the behavior when no current flows in the bias windings. As can be seen in the time step figures (Figures 4.11, 4.12, 4.13, 4.14 and 4.15), the magnetic field strength in the area close to the bias wires is damped. In fact the field strength is close to zero on the order of interest for a significant amount of time for each period of the sinusoidal signal. Now considering that the $\dot{\mathbf{B}}$ probes are located very close to the bias loop wires, and considering that they are constructed to pick up changes in magnetic fields and sized to be sensitive to very strong fields, the modeling results give a plausible and convincing reason for why the observed $\dot{\mathbf{B}}$ signals were so weak as to be almost impossible to distinguish from noise. As for the weak Φ-loop signals, these are supported by observations as well since the current carrying bias wires severely limit the flux inside the Pyrex tube (which is the area of interest). In fact, as the main coil changes direction to oppose the "static" bias field, the flux and strength inside the Pyrex tube drops to almost zero, although the field inside the Pyrex tube never quite changes direction. In addition to a reduced field flux inside the Pyrex tube, this lack of field reversal inside the Pyrex tube effectively makes it impossible to create any plasmoids as the rapid field reversal is a requirement in the tearing and formation process of a plasmoid. As such, the QuickField™ transient model results strongly indicate that the current setup will never be able to produce plasmoids.

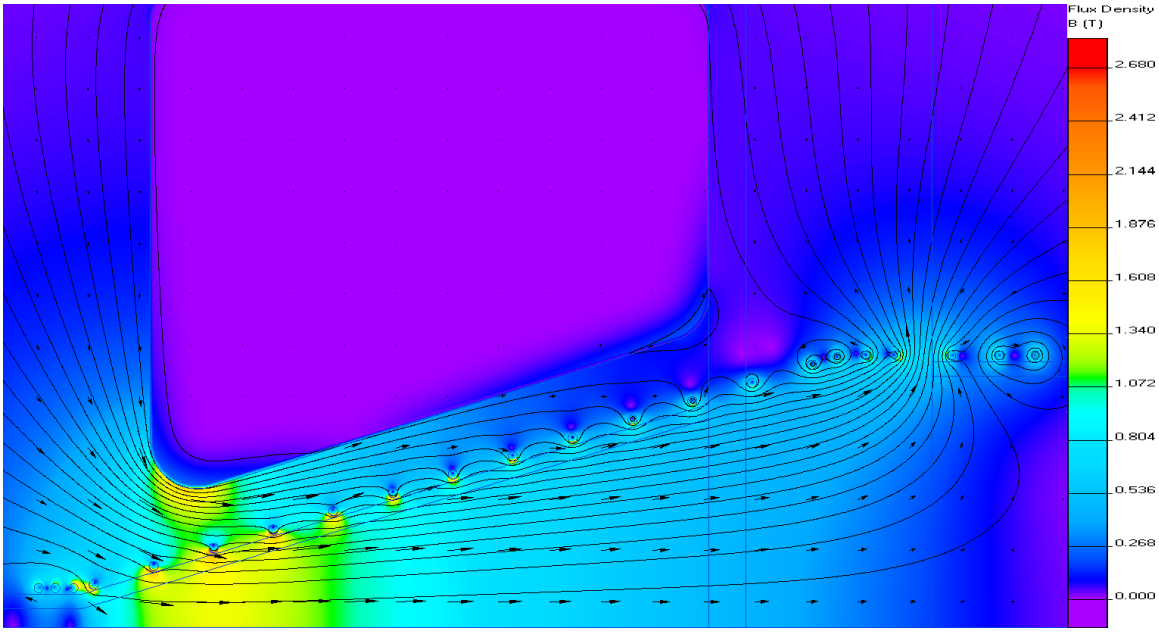


**Figure 4.11**: Transient analysis of both coils, 1 $\mu$s. [Transient analysis, first maxima of the main coil at 1 $\mu$s. Note the direction of the field inside the Pyrex tube.]

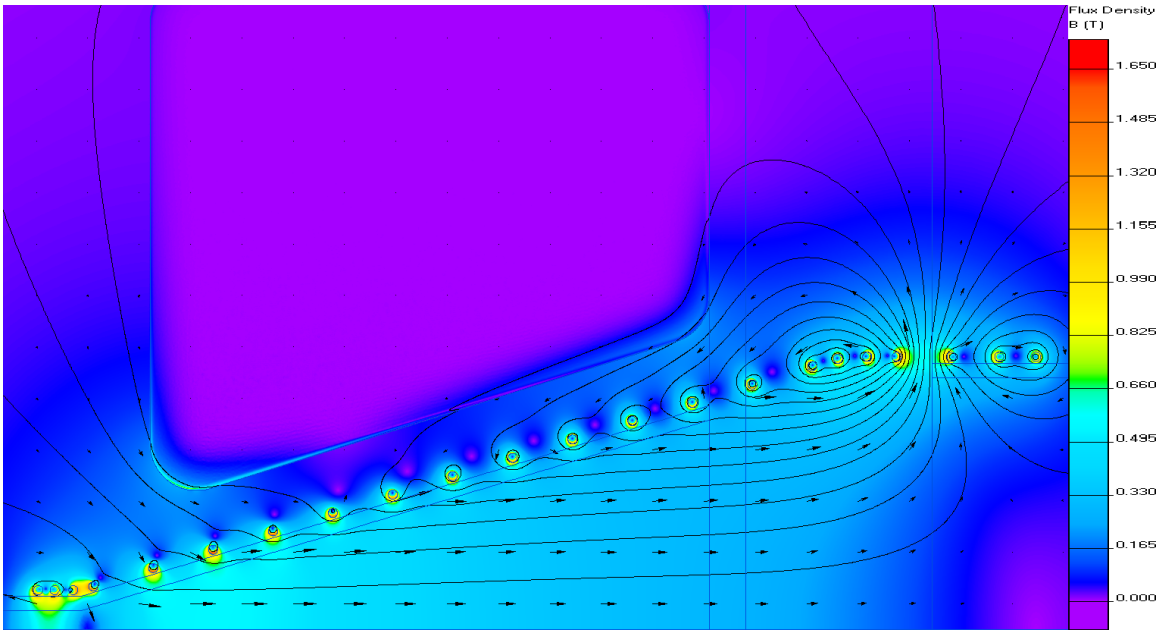


**Figure 4.12**: Transient analysis of both coils, 2 $\mu$s. [Transient analysis, first zero crossing of the main coil at 2 $\mu$s.]

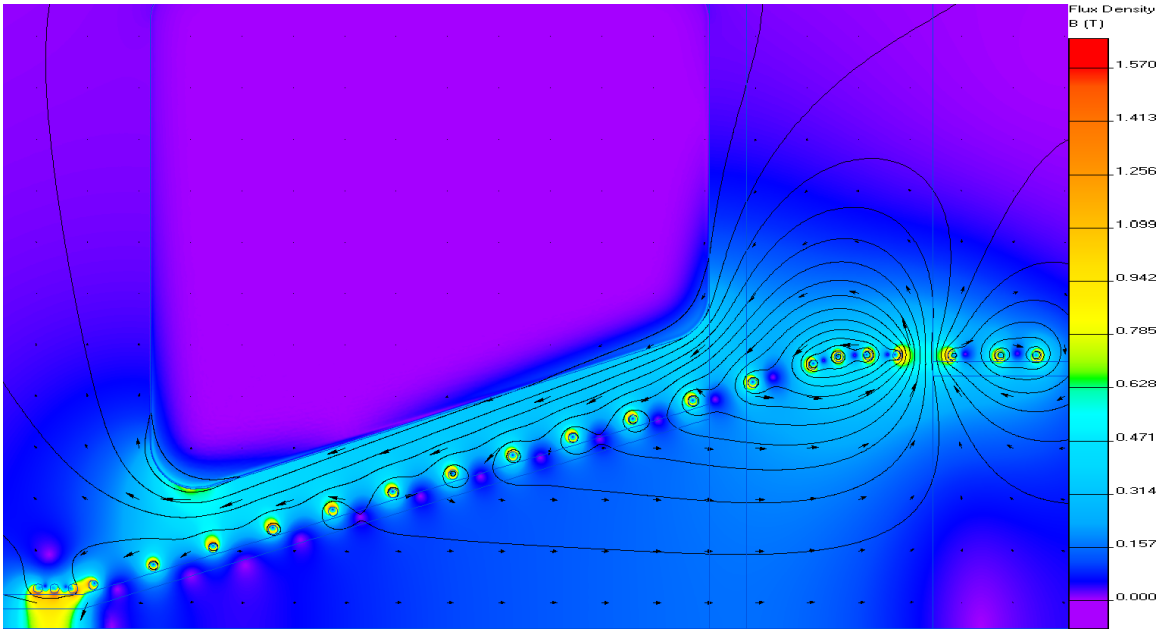


**Figure 4.13**: Transient analysis of both coils, 3 $\mu$s. [Transient analysis, first minima of the main coil at 3 $\mu$s. Note that the direction of the field inside the Pyrex tube did *not* reverse. The lack of field reversal as the main coil completes one period of oscillation effectively prevents the formation of a plasmoid.]

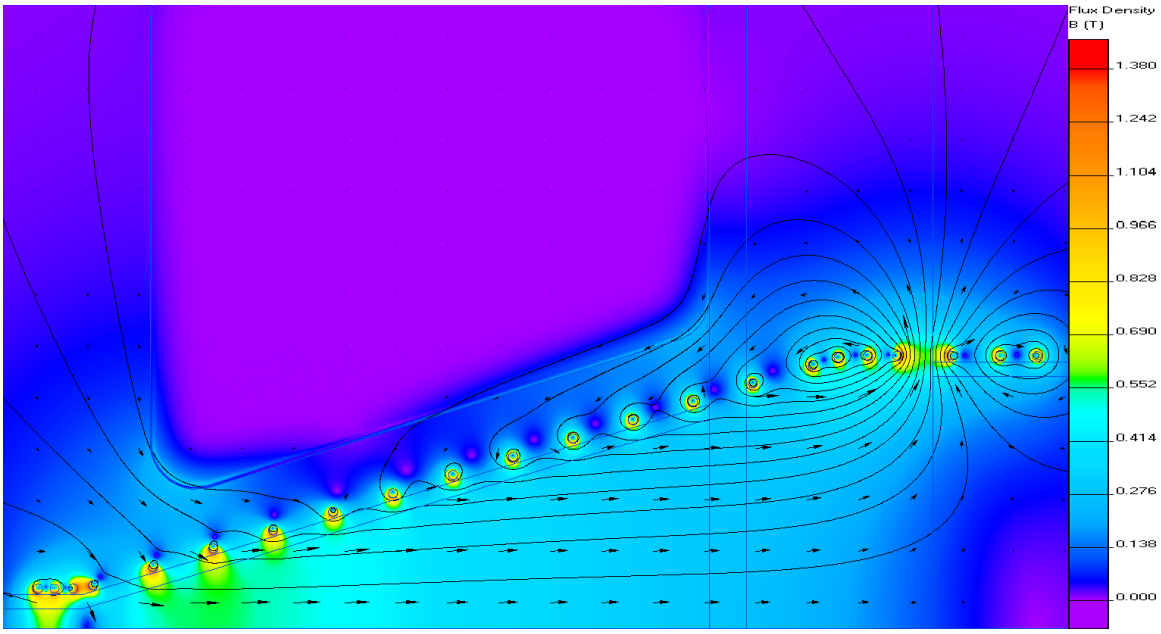


**Figure 4.14**: Transient analysis of both coils, second zero crossing of the main coil at 4 $\mu$s.

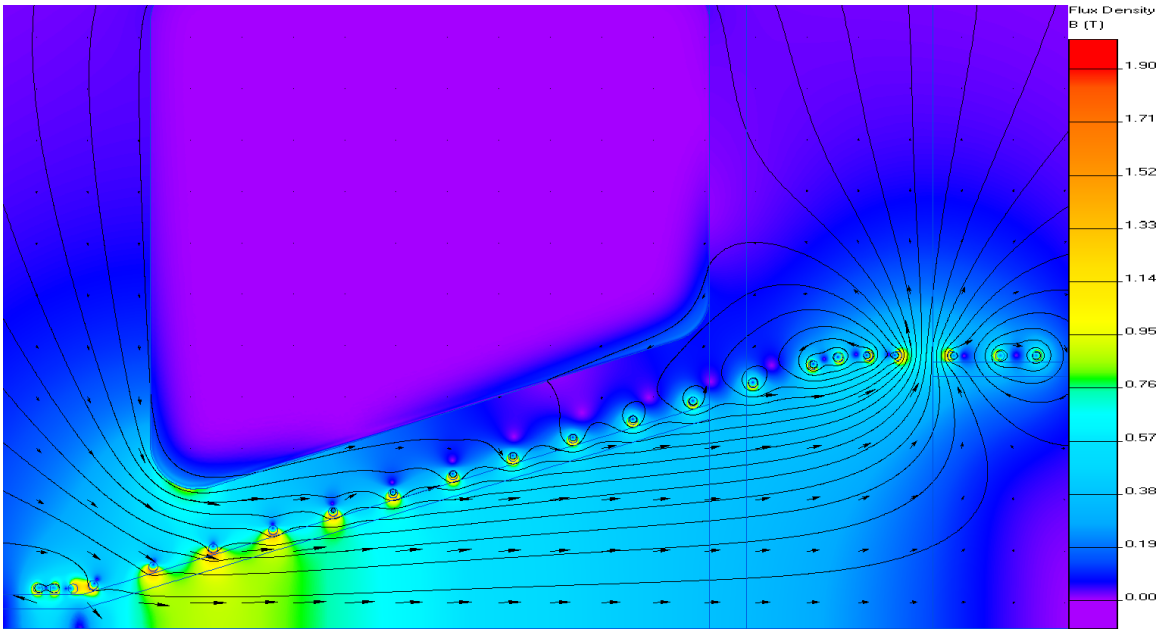


**Figure 4.15**: Transient analysis of both coils, second maxima of the main coil at 5 $\mu$s.

It was realized that the problem with the reduced field and flux inside the Pyrex tube was likely to be a combination of the presence of the metal wires and their associated fields. To test this further, the same problem setup as outlined above was run, but with a strongly reduced current in the x-point and bias coils. Instead of running the model with 3000 A in the bias system, the current was reduced to 750 A to see if conditions would be more favorable for plasmoid formation. As seen in the time step figures (Figures 4.16, 4.17, 4.18 and 4.19), using 750 A as the bias current, the bias field is now much weaker and as expected, the main field is now strong enough to reverse the direction of the field inside the Pyrex tube. However, compared to the un-modified PTX, the fields in the area of interest are much weaker

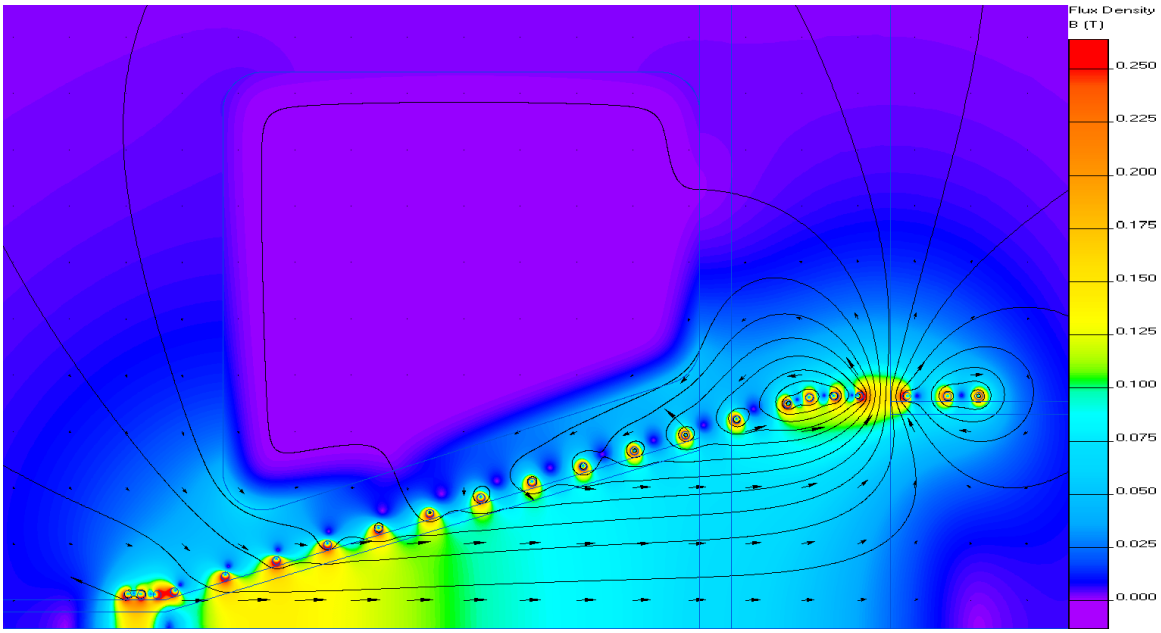


**Figure 4.16**: Transient analysis of both coils for 750 A bias current at 0 $\mu$s. [The maximum field very close to the bias wires reached 0.347 T, but across the region of interest, it ranged from only 0.050 T to 0.150 T.]

in the throat region, as seen in Figure 4.20 where the fields inside the Pyrex tube in the throat area are in the neighborhood of 1 T.

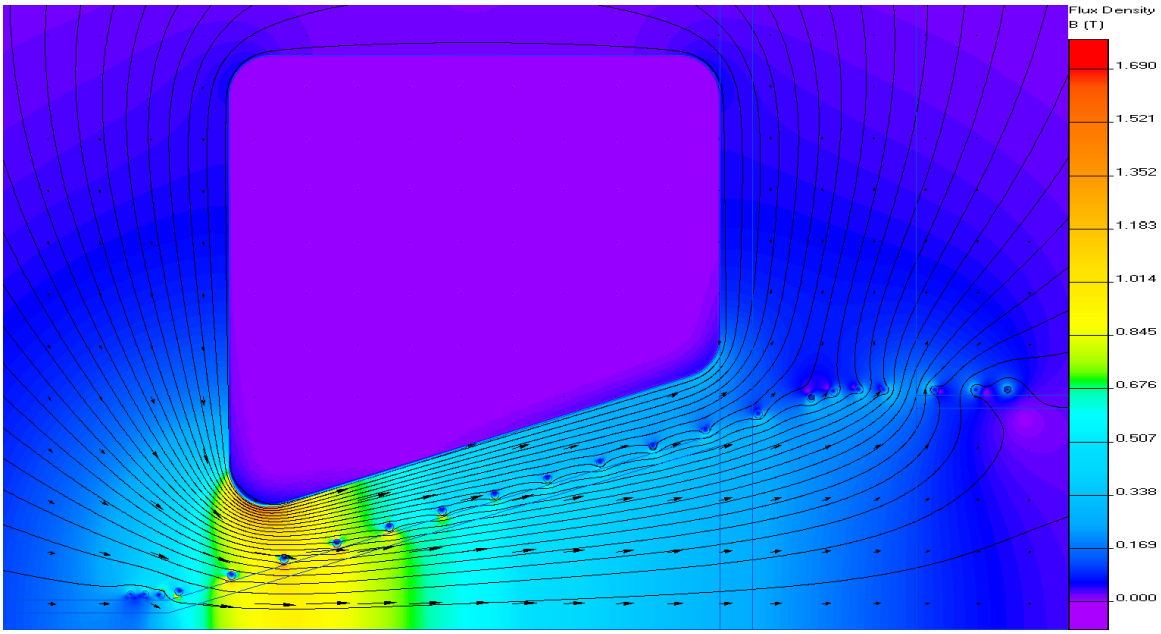


**Figure 4.17**: Transient analysis with a bias current of 750 A at the first main coil maxima at 1 $\mu$s. [As seen, the field inside the Pyrex tube reaches levels of approximately 1 T.]

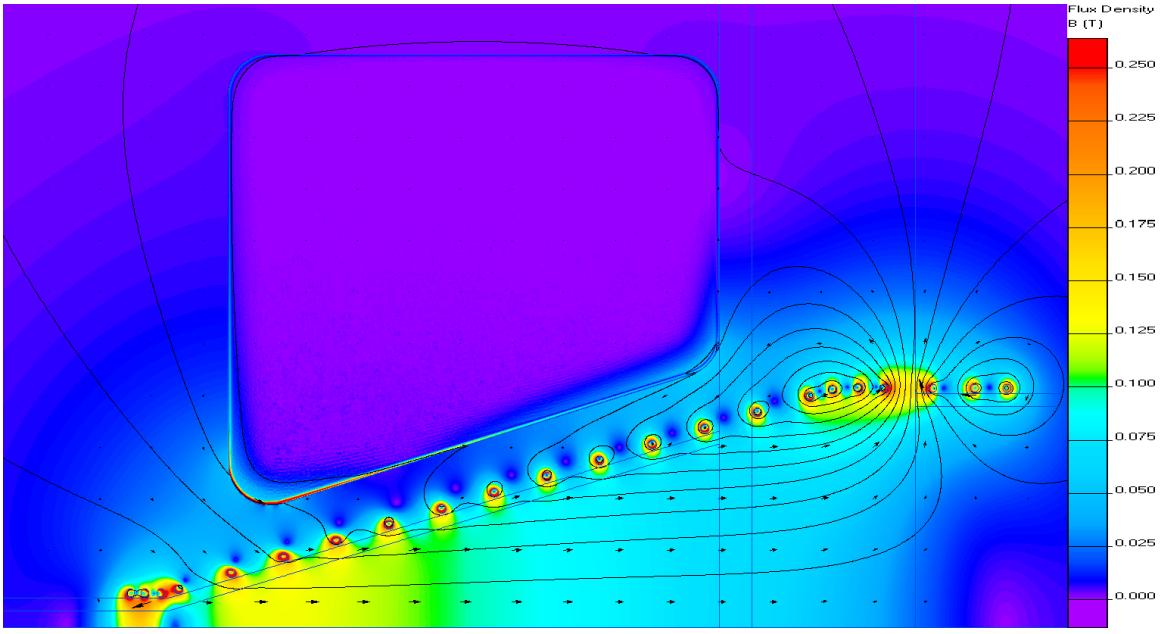


**Figure 4.18**: Transient analysis with a bias current of 750 A at the first zero crossing at 2 $\mu$s. [The field is very weak and compares well with the conditions at 0 $\mu$s.]

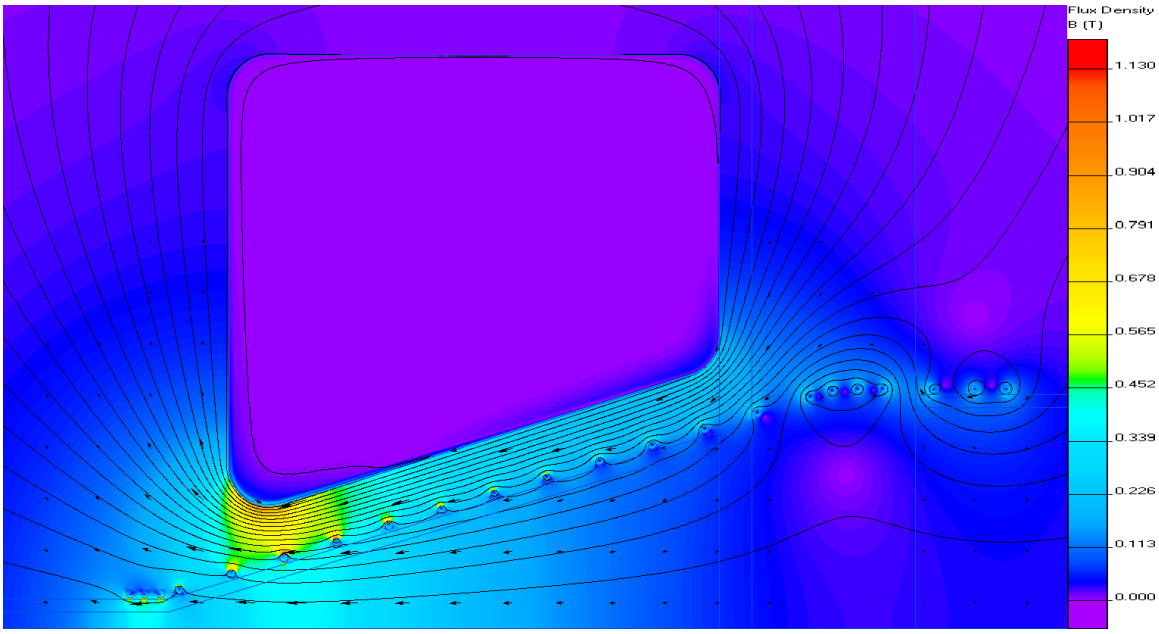


**Figure 4.19**: Transient analysis with a bias current of 750 A at the first main coil minima at 3 $\mu$s. [As evidenced in the figure, a significant amount of the main field is opposed by the bias field current. The net result inside the Pyrex tube is a reversed field of approximately twice (0.300 T) the strength (in the opposite direction) compared to the situation at 0 $\mu$s and 2 $\mu$s.]

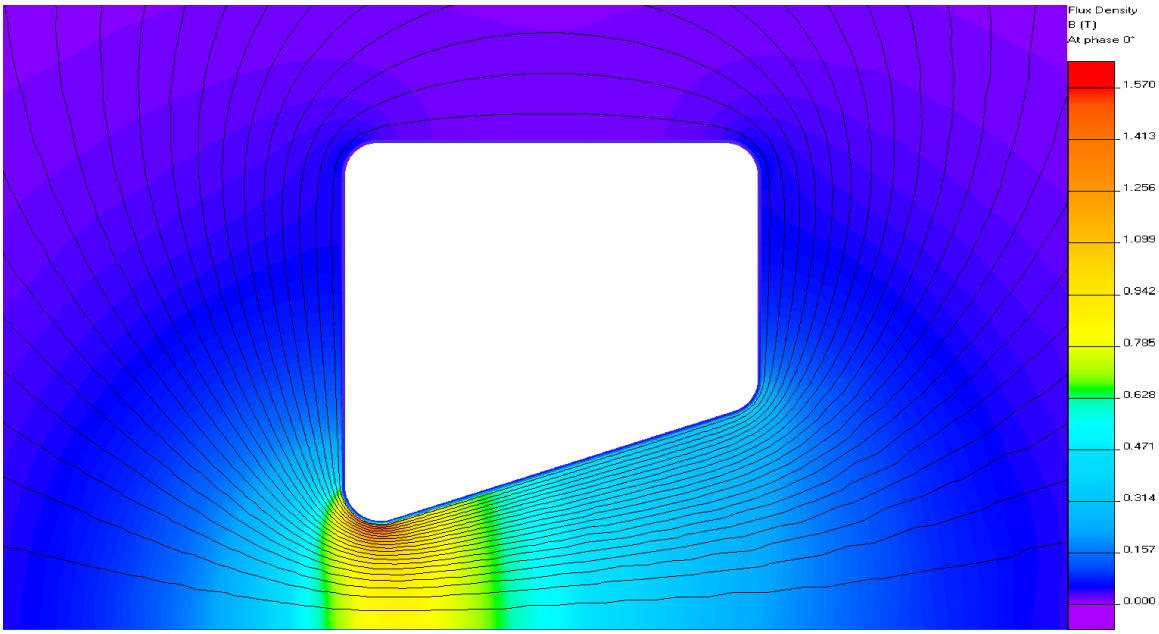


**Figure 4.20**: Analysis of a scenario with only the main coil present. [The inside of the main coil was neglected in this static analysis.]

## 4.4 Effects of the Main-to-bias Coupling on Diagnostic and Periphery Systems

As can be seen in all the presented analysis results in which there was a current present in the bias windings, the local field topology in the immediate vicinity of the bias wires is severely affected. Even in the cases of no current in the bias field, minor perturbations in the local field geometry would make any $\dot{\mathbf{B}}$ readings near impossible to interpret in a meaningful way. As described in Section 4.2, there will be an induced current, strongly dependant on the time-varying main coil field and the position of the bias wire. This would further complicate any $\dot{\mathbf{B}}$ analysis to the point of ludicrous, and that is before trying to take into consideration any effects that might be introduced by the bias driver circuitry. The bias driver circuitry would at times reinforce and at times work against the induced currents and the net result basically makes the current design and position of $\dot{\mathbf{B}}$ probes worthless. If the $\dot{\mathbf{B}}$ probes had been mounted inside the Pyrex tube on a scanning probe arm that could be accurately moved and positioned, then it is likely that the probes would yield data that could be accurately interpreted in terms of local (plasmoid or plasma) characteristics. However this is of no consolidation for the Φ-loop probes. In order to attain the most valuable information from the Φ-loop probes, a combination of Φ-loop data and $\dot{\mathbf{B}}$ data is required to form an "excluded flux array" [1].

## 4.5 Possible Future Improvements

From the QuickField™ analytical results, it seems clear that the current design for incorporating a bias field into PTX will be ineffective. It is equally clear that it severely hamstrings the necessary magnetic diagnostics, leading to virtually useless data. As such, it is obvious that the current design was a step back and not a step forward as was initially hoped. Over the course of the experimentation on the current setup, several observations were made as to how the design could be improved, from co-winding the bias and the main coil to better placement and integration of the magnetic diagnostics to increased main coil inductance (to reduce energy lost in parasitic inductance). These enhancements already exist in the PT-1 experiment [69], where the main coil and the bias coil are co-wound and co-planar. The PT-1 setup is very likely the best way of incorporating a bias field for a plasmoid thruster and the design is patented by the National Aeronautics and Space Administration (NASA) [69]. While permission to construct a replica of the PT-1 for research purposes would not be impossible to get, material budget constraints as well as time constraints makes such a route difficult.

As such, to make the most of the currently available experiment (the PTX) and resources, a compromise is possible by once again moving the bias coils outside of the main coil just like in the DC bias setup, and applying a high current pulse to the coils. Drawbacks are mainly the fact that a solenoid is very good at producing a strong magnetic field inside of itself, but not very good at projecting it outside. Further, it will no longer be possible to have x-points in a sensible location. If x-point coils are

included, they would be so far away from the PTX main coil that they would most likely not be very beneficial. Positioning the coils outside the main coil drastically reduces the coupling from the main coil into the solenoids as evidenced during the initial trials using normal solenoid "magnetic" wire on the low voltage DC system. Arcing was not observed in this configuration, although there were indications of potential voltage reversal on this setup. The DC case used hundreds of loops of wire while the new proposed pulsed system would use an order of magnitude fewer loops. Since the total energy coupled into the bias solenoid depends on the number of turns, this should further mitigate the problem. As such, the expected life of the SCR and the bias capacitor bank will increase and the risk of damage to the bias control system will decrease.

During the final two days with the QuickField™ licence, an improvised setup such as the one described above was simulated in the same fashion as the current setup. The chief difference was in the way the coils were modeled in this case. Since the bias coils in this setup are located outside the main coil, they need to consist of many loops of wire to at least in part compensate for the drop in field strength in the area of interest. The bias coil located at the throat of the main coil was approximated as a solid block sized to approximately correspond to 30 turns, 3 layers tall by 10 wires wide. The current assigned to this block in the first simulation (see Figure 4.21, magnetostatic with only the bias turned on) was 30 turns $\times$ 2000 $^{A}/_{turn}$, but this was moderated and changed to a lower value of 1000 $^{A}/_{turn}$ for the rest of the simulation to ensure that the simulated current levels would be possible to attain in the lab. The bias coil located at the mouth of the main coil was approximated as

a solid block equivalent to 10 turns arranged as a single row of wires. This coil was limited to a single row due to space constraints near the G10 support of the main coil where the clearance between the G10 and the Pyrex tube does not readily allow for more than one layer of wire. The current assigned to this block for the first test was $3000\,{}^{\mathrm{A}}/_{\mathrm{turn}}$ which was changed to be identical ($1000\,{}^{\mathrm{A}}/_{\mathrm{turn}}$) with the other block for all the other simulations on the assumption that both blocks will be powered by the same pulsed system and as such the current will be identical in all the windings. As a check of the model setup, a magnetostatic case was also run in which the main coil was active and the bias coils were not. The results of this analysis can be seen in Figure B.1.

The next step of the analysis was to solve a transient problem involving just the bias coils, assuming for the sake of easy comparison with the current system that this new pulsed system also reaches its peak after 200 $\mu$s. The magnetic field topology after 200 $\mu$s is shown in Figure 4.22. Notice how the color map has been adjusted to give a higher resolution of colors in the area of interest, causing massive saturation underneath the coils (which is not an area of immediate interest). For reference, the maximal field strength under the bias coils were given as 0.935 T by QuickField™.

The final analysis done in the time available with the QuickField™ license was to run a transient case with both the bias and the main coils active and using the 200 $\mu$s time step result from the "bias only" analysis as the initial conditions. The results of this analysis, starting with the initial conditions shown in Figure 4.22 and proceeding with 1 $\mu$s steps are shown in Figures 4.23, 4.24 and 4.25. After the time ran out on the license, it was noticed that the setup for this problem contained two

errors. The first and most important error is located in the leftmost bias coil. It was incorrectly specified with a conductivity value of $59.6\,S \times m^{-1}$ instead of the correct copper conductivity of $59.6{\times}10^{6}\,S \times m^{-1}$. As such, the main coil field easily penetrates that block and the overall topology will be quantitatively incorrect (but still useful in a qualitative manner). The other error that is present in the model is a block line cutting the throat bias solenoid (far right block) into 2 separate parts. As can be seen in the figures, this line caused QuickField™ to model that block as 2 separate blocks placed very close together, causing some disturbance in the local field lines. Even though the results from these analysis cannot be taken to be exactly replicating the actual real magnetic field topology to the smallest level of detail, the results are still good as a design guide in a qualitative manner.

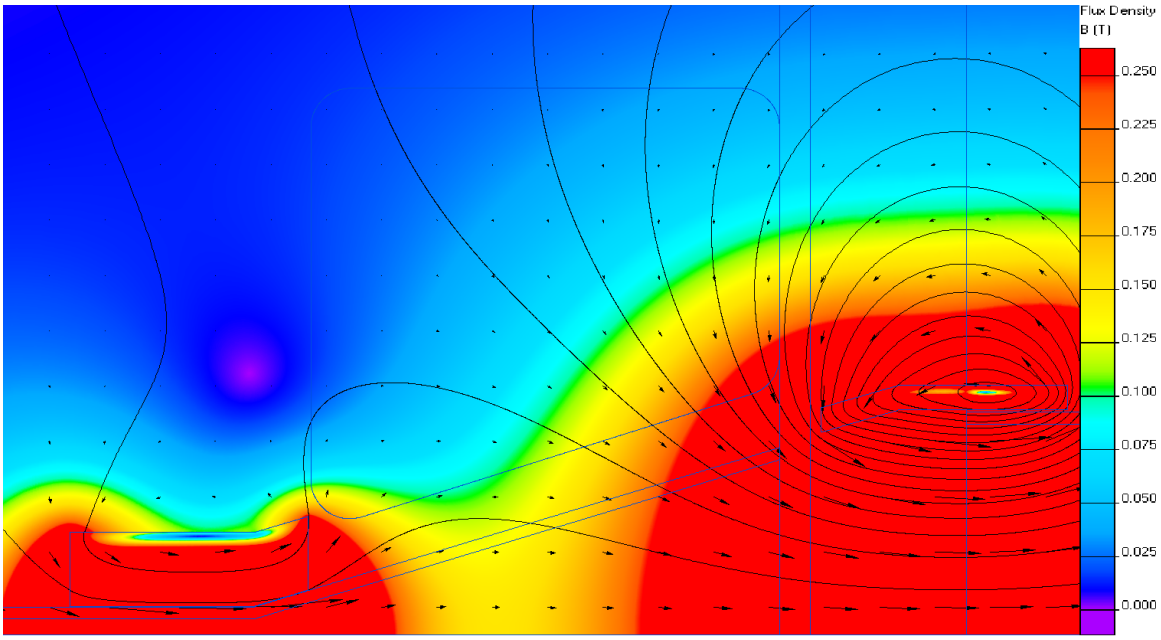


**Figure 4.21**: Simulation of proposed pulsed external bias field: DC with only the bias coils. [Only the bias coils are energized in this analysis. The color scale was set to a maximum of 0.250 T in order to increase the color resolution in the region of interest. The max field strength inside the left most bias coil (by the throat of the main coil) was 1.75 T with 2000 A in the simulated 30 turns. The field strength in the area of interest ranges from slightly over 0.250 T down to approximately 0.125 T midway between the two bias coils.]

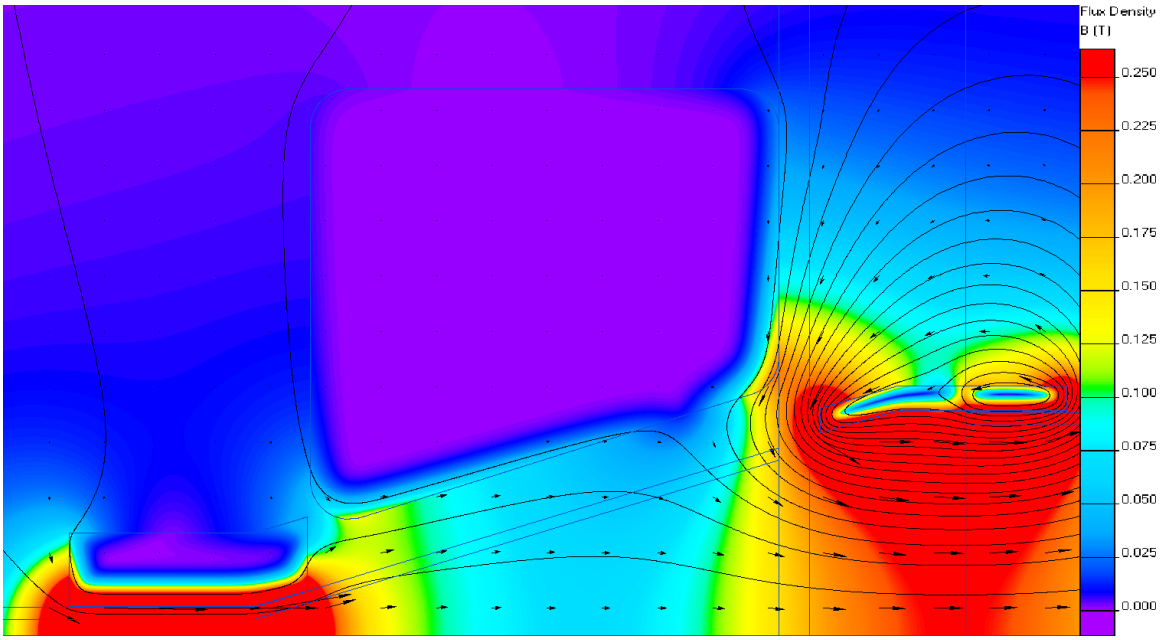


**Figure 4.22**: Simulation of proposed pulsed external bias field at 200 $\mu$s with only the bias coils. [The transient results at 200 $\mu$s used as the initial conditions for the more detailed transient analysis in which the main coil starts to oscillate. The color legend was adjusted to give greater fidelity to the region of interest, inside the Pyrex tube. As a result, the area under and immediately surrounding the bias solenoids are saturated. The maximal field under the solenoid was 0.935 T.]

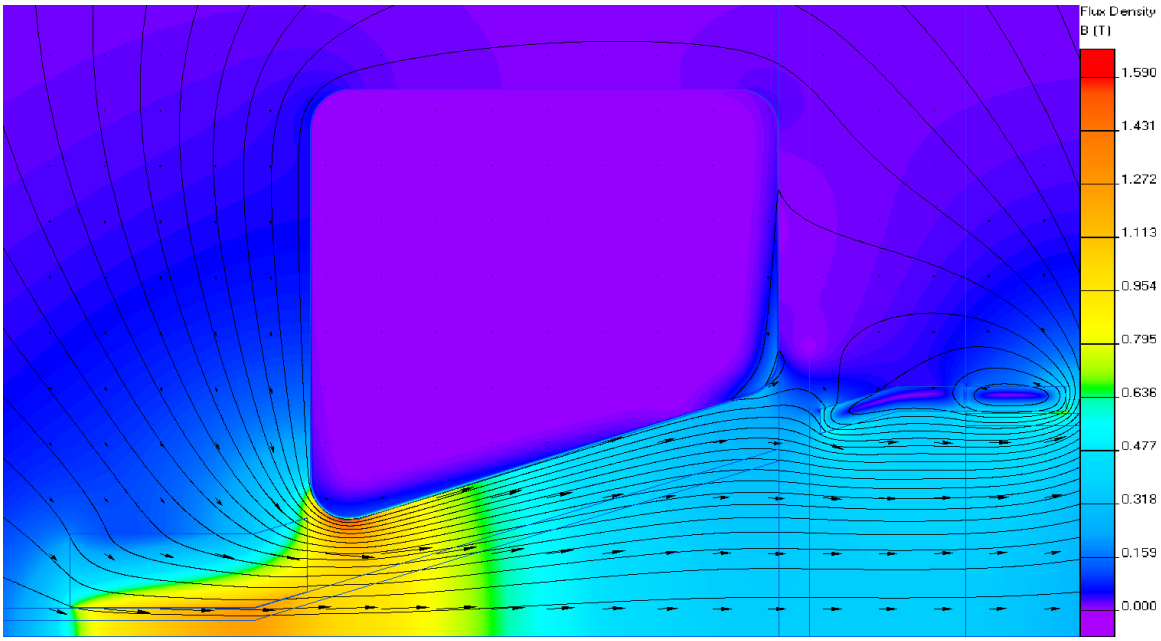


**Figure 4.23**: Simulation of proposed pulsed external bias field at 1 $\mu$s with all coils. [The transient results at 1 $\mu$s (or effectively 201 $\mu$s) when both the main coil and the bias coils are active. As can be seen by the main field soaking into the leftmost bias coil, the conductivity is incorrect. Note also how the bias field had time to soak into the main coil during the initial 200 $\mu$s.]

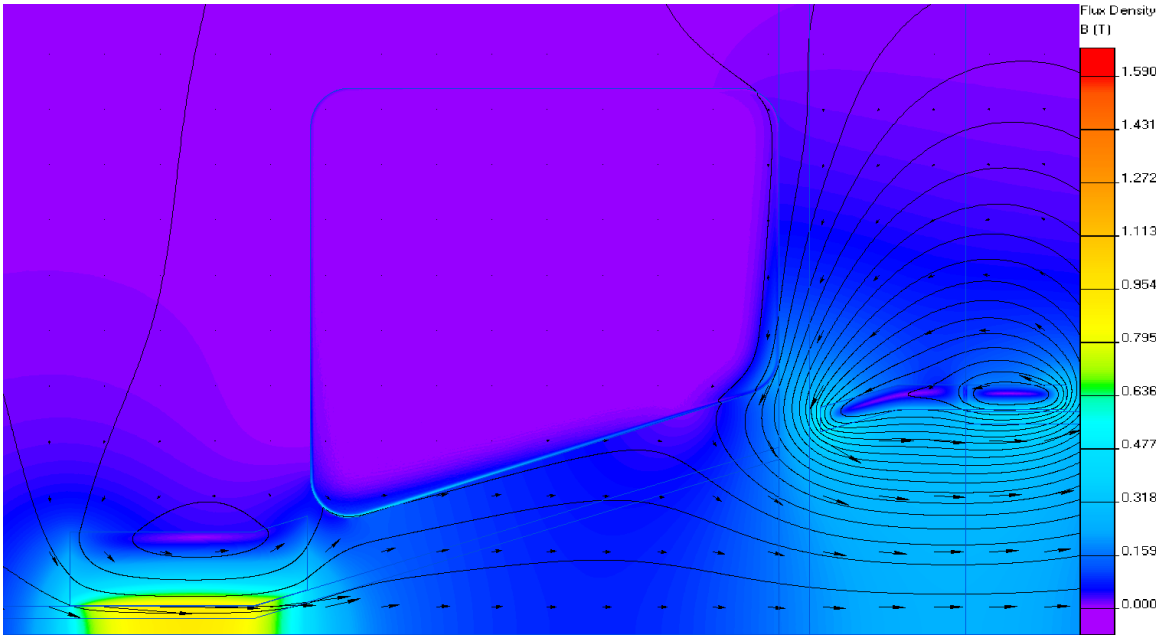


**Figure 4.24**: Simulation of proposed pulsed external bias field at 2 $\mu$s with all coils. [This is the first zero crossing of the main coil and as a result the fields are generally weak.]

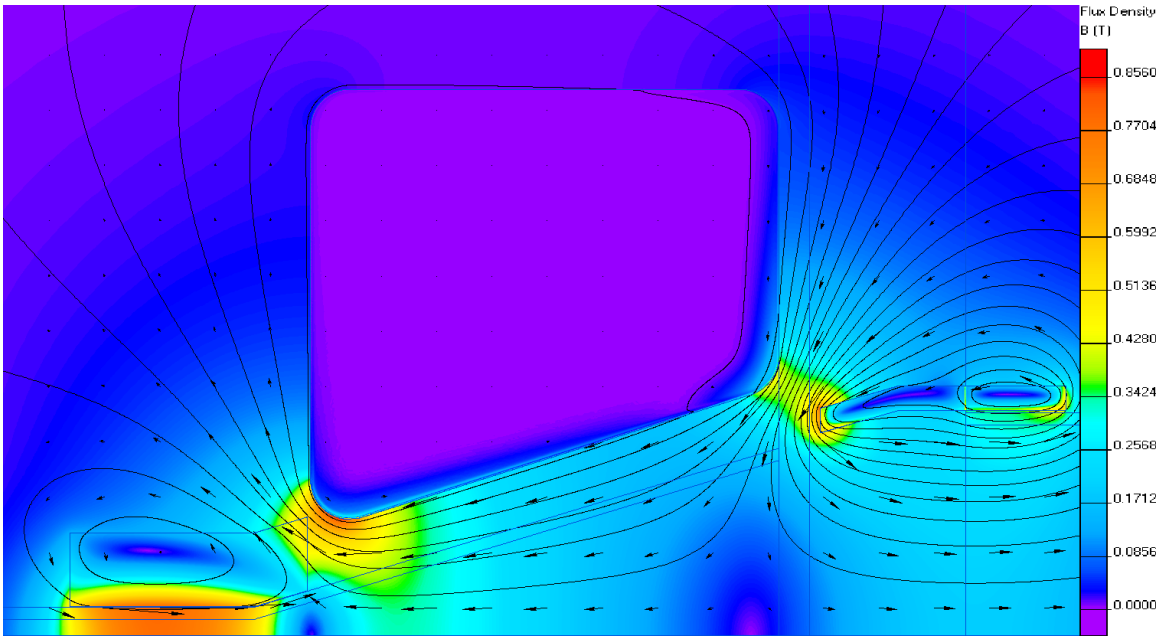


**Figure 4.25**: Simulation of proposed pulsed external bias field at 3 $\mu$s with all coils. [This is the first minima of the main coil and as can be seen the field direction in the Pyrex tube has now fully changed direction, one of the conditions required for a plasmoid to form. There are two points between the bias and main coil towards the symmetry axis where the field strength is very low (indicated by dark blue to purple). This could help plasmoid formation in a similar manner to the way the previous design's x-points.]

# CHAPTER 5

# CONCLUSIONS

*In all science, error precedes the truth, and it is better it should go first than last.*

—Hugh Walpole

## 5.1 Overview

This chapter contains concluding remarks on the work on including an internal bias field on the PTX setup. Recommendations are included for design and implementation of an effective bias field system.

## 5.2 Conclusions

The Plasmoid Thruster Experiment (PTX) is a plasma propulsion device used to study inductively coupled, electromagnetic, pulsed plasma acceleration. An RLC capacitor bank drives approximately 50 kA current through a conical theta pinch coil. In the original design, a partially ionized gas trapped the magnetic field inside the coil volume during the first or second half cycle of the ringing circuit. This field is referred to as the bias field. Field reversal from the main coil leads to a resistive tearing at the boundary between antiparallel field lines separating the bias and main

coil fields, forming a closed field line magnetic topology with confined plasma, referred to as a plasmoid. The plasmoid is accelerated by a magnetic field pressure gradient generated by the main coil field. The internal resistance in the circuit causes the peak magnetic field strength to decrease every half cycle. Consequently, the acceleration by the main coil, which is proportional to the square of the magnetic field generated by the main coil is compromised.

This decrease in performance motivated the current work, which was to separate the bias field from the main coil, so that plasmoid formation and acceleration could occur on the first or second half cycle of the main bank circuit. The approach chosen was to make as few changes to the existing hardware as possible, both to minimize cost and to facilitate comparison with the previous experimental iteration. As a result, a bias coil was wound inside the main coil around the Pyrex tube. A separate capacitor bank with a much longer ringing period was used to drive the bias coil, and the peak current and number of turns gave a quasi-steady field strength of the same order as the peak field generated by the conical theta pinch coil, as desired.

While seemingly a good idea, wrapping the bias field coil on the Pyrex tube directly under the main coil had the severe disadvantage of impeding the main magnetic fields to the extent where the conditions required for successful plasmoid creation and acceleration become threatened. Even if the current supplied to the bias field is reduced drastically to allow for field reversal, the problem of disrupted diagnostics remains. The sought after advantages of a strong bias field in the area where such a field would have the greatest impact are rendered invaluable by these facts. As such, the original objectives of improving on the PTX design have failed. This is not to say

that valuable insight on the workings of PTX was not made. Through this work it is now apparent that the PTX design is close to reaching its limits when it comes to magnetic pre-biasing, and in fact has been superseded by other designs such as PT-1. Even so, PTX might still offer scientific value in several ways over the coming months and years.

## 5.3 Future Work

Since better designs exist for incorporating a dedicated magnetic bias field, it is unlikely that PTX can contribute much in the area of improved bias field arrangements. However, there is still much that can be learned about the formation and life of plasmoids and related FRC configurations. There are two immediate options for PTX:

–In one, the current bias coils are removed and replaced by bias coils outside of the main coil area as previously discussed. In this scenario, the effects of such a magnetic field during the formation of a plasmoid configuration can be studied, as was originally intended with the current design. As seen in Section 4.5 the preliminary work on such a design has been started. It combines the advantages of the high peak currents of a pulsed system with the position of the DC system which did not prevent magnetic field reversal. The field geometry inside the Pyrex tube, however, is changed by these bias field solenoids, but the effects should be far smoother and less dramatic and could probably be treated analytically by subtracting a vacuum baseline profile from the plasma profile. The tradeoff will be that the magnetic field in the region of interest is not as great as it was with the bias coil directly underneath the main coil. However by nature of a pulsed system, it is possible to compensate

somewhat for this by increasing the pulse voltage and drive an even higher current through the coil. In addition, the field strength can be increased by increasing the number of turns in the coils, up to a certain point. The optimal tradeoff between number of turns and increased voltage (*i.e.,* increased current) depends on the rate of growth of the resistance in the extra wire needed for the turns. Things to keep in mind if this approach is followed include voltage coupling between the main and the bias coil (keep the number of turns low to decrease this problem and use extra insulation on the coil wires to prevent arcing) and tuning the bias circuit parameters to behave as a critically damped circuit with a pulse time that is large compared to the main discharge event of PTX.

–In the other, the bias system can be removed in its entirety, bringing the experiment back to its original configuration. At that point, a 3-D magnetic probe array could be translated inside of the Pyrex coil region and probe the magnetic properties of plasmoids as they are formed without a dedicated magnetic bias field. This could potentially bring more detailed knowledge of the composition and evolution of plasmoids produced by the PTX. A natural step after such measurements have been made would be to in the short term replace the current 17.5° with the 8.5° coil currently kept in storage. The study of internal magnetic fields could then be repeated, bringing with it more information on how to optimize coil angles to produce FRC configurations. Another natural step following this would be to add back in the bias coils outside of the main coil area and attempt to repeat the analysis.

# APPENDICES

# APPENDIX A

## TABLES OF DATA

*The scientific theory I like best is that the rings of Saturn are composed entirely of lost airline luggage.*

—Mark Russell

**Table A.1**: $\dot{\mathbf{B}}$ calibration data. [Compared to [1], the calibration values are lower. This was a result of the choice to use $V_{p-p}$ on the scope instead of $V_{rms}$. Taking that into consideration, the values compared well with each other. Set 1 and Set 2 represent taking the $\dot{\mathbf{B}}$ probe out of the Helmholtz coil and re-positioning it before taking the readings again. This was done to test the sensitivity of the mounting process on the repeatability of the calibration.]

| Probe # | Average $NA$, set 1 $10\times10^{-6}\,m^2$ | std dev, set 1 $m^2$ | Average $NA$, set 2 $10\times10^{-6}\,m^2$ | std dev, set 2 $m^2$ |
|---|---|---|---|---|
| 1 | 81.27 | 383.69E-9 | 81.20 | 380.46E-9 |
| 2 | 82.50 | 1.79E-6 | 81.87 | 1.75E-6 |
| 3 | 83.79 | 2.37E-6 | 84.62 | 1.71E-6 |
| 4 | 84.38 | 895.72E-9 | 85.15 | 853.76E-9 |
| 5 | 87.58 | 4.41E-6 | 92.76 | 490.96E-9 |
| 6 | 90.00 | 1.67E-6 | 90.33 | 1.38E-6 |
| 7 | 101.65 | 3.00E-6 | 104.44 | 1.94E-6 |

**Table A.2**: Data set 1 from 21 Nov 2007

| **Chamber** (mTorr) | **ΔP** (mTorr) | **Δt** (s) | **Ambient** (atm) | **Instant. Vol.** (l) |
|---|---|---|---|---|
| 71.192 | - | - | 1.0023 | - |
| 99.757 | 28.56 | 9.955 | 1.0020 | 12.774 |
| 127.471 | 27.71 | 9.969 | 1.0026 | 13.185 |
| 155.157 | 27.69 | 9.958 | 1.0026 | 13.183 |
| 183.722 | 28.56 | 9.963 | 1.0023 | 12.784 |
| 211.847 | 28.13 | 9.883 | 1.0023 | 12.879 |
| 239.561 | 27.71 | 10.047 | 1.0023 | 13.288 |
| 268.565 | 29.00 | 9.958 | 1.0026 | 12.584 |
| 296.251 | 27.69 | 9.958 | 1.0023 | 13.183 |
| 324.376 | 28.13 | 9.964 | 1.0026 | 12.985 |
| 352.529 | 28.15 | 9.974 | 1.0023 | 12.985 |
| 380.215 | 27.69 | 9.951 | 1.0023 | 13.174 |
| 408.780 | 28.56 | 9.976 | 1.0026 | 12.800 |
| 436.905 | 28.13 | 9.961 | 1.0026 | 12.981 |
| 464.619 | 27.71 | 9.968 | 1.0020 | 13.183 |
| 492.744 | 28.13 | 9.927 | 1.0023 | 12.937 |
| 521.309 | 28.56 | 10.008 | 1.0026 | 12.842 |
| 548.556 | 27.25 | 9.968 | 1.0023 | 13.409 |
| 576.709 | 28.15 | 9.957 | 1.0023 | 12.963 |
| 605.274 | 28.56 | 9.972 | 1.0026 | 12.795 |
| 633.399 | 28.13 | 9.966 | 1.0023 | 12.987 |
| 661.085 | 27.69 | 9.961 | 1.0023 | 13.187 |
| 689.677 | 28.59 | 9.974 | 1.0020 | 12.786 |
| 716.924 | 27.25 | 9.959 | 1.0026 | 13.397 |
| 745.489 | 28.56 | 9.963 | 1.0026 | 12.784 |
| 774.054 | 28.56 | 9.963 | 1.0023 | 12.784 |
| 801.767 | 27.71 | 9.963 | 1.0023 | 13.177 |
| 829.892 | 28.13 | 9.952 | 1.0026 | 12.969 |
| 858.018 | 28.13 | 9.973 | 1.0023 | 12.997 |
| 886.143 | 28.13 | 9.963 | 1.0023 | 12.984 |
| 913.857 | 27.71 | 9.964 | 1.0023 | 13.178 |
| 941.982 | 28.13 | 9.960 | 1.0023 | 12.980 |
| **-** | **28.09** | **9.96** | **1.0024** | **13.004** |

**Table A.3**: Constants and correction factors for data set 1 from 21 Nov 2007

| **Constants and Ambient Conditions** | | |
|---|---|---|
| Calibration Q | 4.79E-02 | $\left(\frac{atm\ cc}{s}\right)$ |
| Calibration Q | 3.64E+01 | $\left(\frac{mTorr\ liter}{s}\right)$ |
| Ambient Temp | 26 | (°C) |
| $T_{Cal}$ | 25 | (°C) |
| $C_T$ | 0.2 | $\left(\frac{\%}{^\circ C}\right)$ |
| Mean Airport P | 30.0167 | (in Hg) |
| Airport P | 1.0031 | (atm) |
| **Correction Calculations** | | |
| $Q_{TemptCorr}$ | 0.0001 | $\left(\frac{mTorr\ liter}{s}\right)$ |
| $Q_{PressCorr}$ | 1.005 | unitless |
| $Q_{Corrected}$ | 4.823E-02 | $\left(\frac{atm\ cc}{s}\right)$ |

**Table A.4**: Data set 2 from 21 Nov 2007

| **Chamber** (mTorr) | **ΔP** (mTorr) | **Δt** (s) | **Ambient** (atm) | **Instant. Vol.** (l) |
|---|---|---|---|---|
| 63.722 | - | - | 1.0020 | - |
| 91.408 | 27.69 | 9.968 | 1.0020 | 13.196 |
| 120.000 | 28.59 | 9.977 | 1.0023 | 12.789 |
| 147.686 | 27.69 | 9.963 | 1.0023 | 13.189 |
| 175.811 | 28.13 | 9.971 | 1.0023 | 12.994 |
| 204.376 | 28.56 | 9.951 | 1.0023 | 12.768 |
| 232.090 | 27.71 | 9.955 | 1.0023 | 13.166 |
| 260.215 | 28.13 | 9.944 | 1.0023 | 12.959 |
| 288.780 | 28.56 | 9.994 | 1.0026 | 12.823 |
| 316.027 | 27.25 | 9.973 | 1.0026 | 13.416 |
| 344.619 | 28.59 | 9.928 | 1.0026 | 12.726 |
| 372.744 | 28.13 | 9.977 | 1.0023 | 13.002 |
| 399.991 | 27.25 | 9.968 | 1.0023 | 13.409 |
| 428.995 | 29.00 | 9.948 | 1.0023 | 12.571 |
| 457.148 | 28.15 | 9.988 | 1.0023 | 13.003 |
| 484.395 | 27.25 | 9.954 | 1.0023 | 13.390 |
| 512.959 | 28.56 | 9.905 | 1.0023 | 12.709 |
| 541.085 | 28.13 | 10.006 | 1.0023 | 13.039 |
| 569.238 | 28.15 | 9.986 | 1.0026 | 13.001 |
| 597.363 | 28.13 | 9.967 | 1.0026 | 12.988 |
| 625.049 | 27.69 | 9.968 | 1.0023 | 13.196 |
| 653.175 | 28.13 | 9.942 | 1.0023 | 12.956 |
| 681.328 | 28.15 | 9.983 | 1.0026 | 12.997 |
| 709.892 | 28.56 | 9.973 | 1.0023 | 12.796 |
| 737.139 | 27.25 | 9.967 | 1.0026 | 13.407 |
| 765.704 | 28.56 | 9.962 | 1.0023 | 12.782 |
| 793.857 | 28.15 | 9.971 | 1.0026 | 12.981 |
| 821.543 | 27.69 | 9.955 | 1.0023 | 13.179 |
| 849.668 | 28.13 | 9.974 | 1.0026 | 12.998 |
| 877.794 | 28.13 | 9.939 | 1.0023 | 12.952 |
| 905.946 | 28.15 | 9.983 | 1.0023 | 12.997 |
| 934.511 | 28.56 | 9.957 | 1.0023 | 12.776 |
| 961.758 | 27.25 | 9.958 | 1.0023 | 13.395 |
| **-** | **28.06** | **9.964** | **1.0024** | **13.017** |

**Table A.5**: Constants and correction factors for data set 2 from 21 Nov 2007

| **Constants and Ambient Conditions** | | |
|---|---|---|
| Calibration Q | 4.79E-02 | $\left(\frac{atm\ cc}{s}\right)$ |
| Calibration Q | 3.64E+01 | $\left(\frac{mTorr\ liter}{s}\right)$ |
| Ambient Temp | 26 | (°C) |
| $T_{Cal}$ | 25 | (°C) |
| $C_T$ | 0.2 | $\left(\frac{\%}{^\circ C}\right)$ |
| Mean Airport P | 30.0167 | (in Hg) |
| Airport P | 1.0031 | (atm) |
| **Correction Calculations** | | |
| $Q_{TemptCorr}$ | 0.0001 | $\left(\frac{mTorr\ liter}{s}\right)$ |
| $Q_{PressCorr}$ | 1.005 | unitless |
| $Q_{Corrected}$ | 4.823E-02 | $\left(\frac{atm\ cc}{s}\right)$ |

**Table A.6**: Data set 1 from 23 Nov 2007

| **Chamber** (mTorr) | **ΔP** (mTorr) | **Δt** (s) | **Ambient** (atm) | **Instant. Vol.** (l) |
|---|---|---|---|---|
| 64.16 | - | - | 1.0138 | - |
| 93.17 | 29.00 | 9.955 | 1.0138 | 12.769 |
| 122.20 | 29.03 | 9.980 | 1.0141 | 12.789 |
| 151.20 | 29.00 | 9.941 | 1.0138 | 12.751 |
| 180.21 | 29.00 | 9.986 | 1.0135 | 12.809 |
| 209.21 | 29.00 | 9.962 | 1.0141 | 12.778 |
| 237.80 | 28.59 | 9.972 | 1.0141 | 12.975 |
| 266.81 | 29.00 | 9.967 | 1.0138 | 12.785 |
| 295.81 | 29.00 | 9.956 | 1.0141 | 12.770 |
| 324.82 | 29.00 | 9.952 | 1.0138 | 12.765 |
| 353.85 | 29.03 | 9.956 | 1.0141 | 12.758 |
| 382.85 | 29.00 | 9.975 | 1.0138 | 12.795 |
| 411.86 | 29.00 | 9.990 | 1.0138 | 12.814 |
| 440.42 | 28.56 | 9.950 | 1.0138 | 12.959 |
| 469.45 | 29.03 | 9.889 | 1.0141 | 12.672 |
| 498.02 | 28.56 | 10.044 | 1.0135 | 13.081 |
| 527.02 | 29.00 | 9.944 | 1.0141 | 12.755 |
| 556.03 | 29.00 | 9.973 | 1.0138 | 12.792 |
| 585.50 | 29.47 | 9.979 | 1.0138 | 12.597 |
| 614.06 | 28.56 | 9.958 | 1.0138 | 12.969 |
| 642.63 | 28.56 | 9.965 | 1.0138 | 12.979 |
| 671.63 | 29.00 | 9.939 | 1.0138 | 12.749 |
| 700.66 | 29.03 | 9.990 | 1.0138 | 12.802 |
| 729.23 | 28.56 | 9.965 | 1.0138 | 12.979 |
| 757.79 | 28.56 | 9.966 | 1.0141 | 12.980 |
| 787.24 | 29.44 | 9.966 | 1.0138 | 12.592 |
| 816.27 | 29.03 | 9.952 | 1.0138 | 12.753 |
| 844.39 | 28.13 | 9.977 | 1.0138 | 13.197 |
| 873.84 | 29.44 | 9.947 | 1.0138 | 12.568 |
| 902.87 | 29.03 | 9.987 | 1.0138 | 12.798 |
| 931.00 | 28.13 | 9.966 | 1.0138 | 13.183 |
| 960.00 | 29.00 | 9.961 | 1.0141 | 12.777 |
| **-** | **28.90** | **9.965** | **1.0139** | **12.830** |

**Table A.7**: Constants and correction factors for data set 1 from 23 Nov 2007

| **Constants and Ambient Conditions** | | |
|---|---|---|
| Calibration Q | 4.79E-02 | $\left(\frac{atm\ cc}{s}\right)$ |
| Calibration Q | 3.64E+01 | $\left(\frac{mTorr\ liter}{s}\right)$ |
| Ambient Temp | 22 | (°C) |
| $T_{Cal}$ | 25 | (°C) |
| $C_T$ | 0.2 | $\left(\frac{\%}{^\circ C}\right)$ |
| mean Airport P | 30.3300 | (in Hg) |
| Airport P | 1.0135 | (atm) |
| **Correction Calculations** | | |
| $Q_{TemptCorr}$ | -0.0003 | $\left(\frac{mTorr\ liter}{s}\right)$ |
| $Q_{PressCorr}$ | 1.028 | unitless |
| $Q_{Corrected}$ | 4.895E-02 | $\left(\frac{atm\ cc}{s}\right)$ |

**Table A.8**: Data set 1 from 26 Nov 2007

| **Chamber** (mTorr) | **ΔP** (mTorr) | **Δt** (s) | **Ambient** (atm) | **Instant. Vol.** (l) |
|---|---|---|---|---|
| 59.767 | - | - | 1.0002 | - |
| 87.892 | 28.13 | 10.006 | 1.0002 | 12.875 |
| 116.045 | 28.15 | 9.940 | 1.0002 | 12.778 |
| 144.170 | 28.13 | 9.990 | 1.0002 | 12.855 |
| 172.735 | 28.56 | 9.955 | 1.0002 | 12.613 |
| 200.861 | 28.13 | 9.964 | 1.0002 | 12.821 |
| 228.574 | 27.71 | 9.958 | 1.0002 | 13.004 |
| 256.699 | 28.13 | 9.969 | 1.0002 | 12.828 |
| 285.264 | 28.56 | 9.969 | 1.0002 | 12.630 |
| 312.950 | 27.69 | 9.928 | 0.9998 | 12.978 |
| 341.103 | 28.15 | 9.994 | 1.0002 | 12.847 |
| 368.350 | 27.25 | 9.960 | 1.0002 | 13.229 |
| 396.915 | 28.56 | 9.965 | 1.0002 | 12.625 |
| 424.601 | 27.69 | 9.955 | 1.0002 | 13.013 |
| 452.754 | 28.15 | 9.966 | 1.0002 | 12.811 |
| 480.879 | 28.13 | 9.976 | 1.0002 | 12.837 |
| 508.565 | 27.69 | 9.956 | 0.9998 | 13.014 |
| 537.569 | 29.00 | 9.972 | 0.9998 | 12.443 |
| 565.283 | 27.71 | 9.972 | 1.0002 | 13.022 |
| 592.969 | 27.69 | 9.951 | 1.0002 | 13.008 |
| 621.094 | 28.13 | 9.952 | 1.0002 | 12.806 |
| 649.219 | 28.13 | 9.985 | 0.9998 | 12.848 |
| 676.933 | 27.71 | 9.946 | 1.0002 | 12.988 |
| 705.058 | 28.13 | 9.985 | 0.9998 | 12.848 |
| 733.623 | 28.56 | 9.965 | 1.0002 | 12.625 |
| 760.870 | 27.25 | 9.960 | 0.9998 | 13.229 |
| 789.023 | 28.15 | 9.969 | 0.9998 | 12.815 |
| 817.148 | 28.13 | 9.959 | 0.9998 | 12.815 |
| 844.834 | 27.69 | 9.953 | 1.0002 | 13.010 |
| 873.399 | 28.56 | 9.979 | 1.0002 | 12.643 |
| 901.112 | 27.71 | 9.959 | 1.0002 | 13.005 |
| 928.798 | 27.69 | 9.964 | 0.9998 | 13.025 |
| 956.924 | 28.13 | 9.97 | 0.9998 | 12.829 |
| **-** | **28.04** | **9.965** | **1.0001** | **12.866** |

**Table A.9**: Constants and correction factors for data set 1 from 26 Nov 2007

| **Constants and Ambient Conditions** | | |
|---|---|---|
| Calibration Q | 4.79E-02 | $\left(\frac{atm\ cc}{s}\right)$ |
| Calibration Q | 3.64E+01 | $\left(\frac{mTorr\ liter}{s}\right)$ |
| Ambient Temp | 22 | (°C) |
| $T_{Cal}$ | 25 | (°C) |
| $C_T$ | 0.2 | $\left(\frac{\%}{^\circ C}\right)$ |
| mean Airport P | 29.9200 | (in Hg) |
| Airport P | 0.9998 | (atm) |
| **Correction Calculations** | | |
| $Q_{TemptCorr}$ | -0.0003 | $\left(\frac{mTorr\ liter}{s}\right)$ |
| $Q_{PressCorr}$ | 1.000 | unitless |
| $Q_{Corrected}$ | 4.762E-02 | $\left(\frac{atm\ cc}{s}\right)$ |

**Table A.10**: Data set 2 from 26 Nov 2007

| **Chamber** (mTorr) | **ΔP** (mTorr) | **Δt** (s) | **Ambient** (atm) | **Instant. Vol.** (l) |
|---|---|---|---|---|
| 55.811 | - | - | 0.9998 | - |
| 83.937 | 28.13 | 9.959 | 0.9998 | 12.829 |
| 112.529 | 28.59 | 9.964 | 0.9995 | 12.625 |
| 139.776 | 27.25 | 9.965 | 0.9998 | 13.250 |
| 168.341 | 28.56 | 9.966 | 0.9995 | 12.640 |
| 196.466 | 28.13 | 9.965 | 0.9995 | 12.836 |
| 224.152 | 27.69 | 9.966 | 0.9995 | 13.041 |
| 252.744 | 28.59 | 9.962 | 0.9995 | 12.623 |
| 281.309 | 28.56 | 9.971 | 0.9995 | 12.646 |
| 308.556 | 27.25 | 9.962 | 0.9992 | 13.246 |
| 337.121 | 28.56 | 9.956 | 0.9995 | 12.627 |
| 365.274 | 28.15 | 9.951 | 0.9995 | 12.806 |
| 392.959 | 27.69 | 9.986 | 0.9995 | 13.068 |
| 421.524 | 28.56 | 9.971 | 0.9995 | 12.646 |
| 449.210 | 27.69 | 9.960 | 0.9998 | 13.034 |
| 476.924 | 27.71 | 9.910 | 0.9992 | 12.955 |
| 505.049 | 28.13 | 10.024 | 0.9995 | 12.912 |
| 533.614 | 28.56 | 9.955 | 0.9995 | 12.626 |
| 561.300 | 27.69 | 9.964 | 0.9995 | 13.039 |
| 589.013 | 27.71 | 9.968 | 0.9995 | 13.031 |
| 617.578 | 28.56 | 9.954 | 1.0002 | 12.625 |
| 645.264 | 27.69 | 9.959 | 0.9995 | 13.032 |
| 673.390 | 28.13 | 9.975 | 0.9995 | 12.849 |
| 701.543 | 28.15 | 9.959 | 0.9995 | 12.816 |
| 729.668 | 28.13 | 9.970 | 0.9998 | 12.843 |
| 757.354 | 27.69 | 9.965 | 0.9998 | 13.040 |
| 785.919 | 28.56 | 9.956 | 0.9995 | 12.627 |
| 813.193 | 27.27 | 9.961 | 0.9995 | 13.232 |
| 841.318 | 28.13 | 9.976 | 0.9995 | 12.850 |
| 869.444 | 28.13 | 9.941 | 0.9998 | 12.805 |
| 897.569 | 28.13 | 9.972 | 0.9995 | 12.845 |
| 925.283 | 27.71 | 9.941 | 0.9995 | 12.996 |
| 953.408 | 28.13 | 10.006 | 0.9995 | 12.889 |
| **-** | **28.05** | **9.964** | **0.9996** | **12.873** |

**Table A.11**: Constants and correction factors for data set 2 from 26 Nov 2007

| **Constants and Ambient Conditions** | | |
|---|---|---|
| Calibration Q | 4.79E-02 | $\left(\frac{atm\ cc}{s}\right)$ |
| Calibration Q | 3.64E+01 | $\left(\frac{mTorr\ liter}{s}\right)$ |
| Ambient Temp | 23 | (°C) |
| $T_{Cal}$ | 25 | (°C) |
| $C_T$ | 0.2 | $\left(\frac{\%}{^{\circ}C}\right)$ |
| mean Airport P | 29.9200 | (in Hg) |
| Airport P | 0.9998 | (atm) |
| **Correction Calculations** | | |
| $Q_{TemptCorr}$ | -0.0002 | $\left(\frac{mTorr\ liter}{s}\right)$ |
| $Q_{PressCorr}$ | 0.999 | unitless |
| $Q_{Corrected}$ | 4.767E-02 | $\left(\frac{atm\ cc}{s}\right)$ |

# APPENDIX B

## FIGURES AND GRAPHS

*In seeking wisdom thou art wise; in imagining that thou hast attained it - thou art a fool.*

—Lord Chesterfield

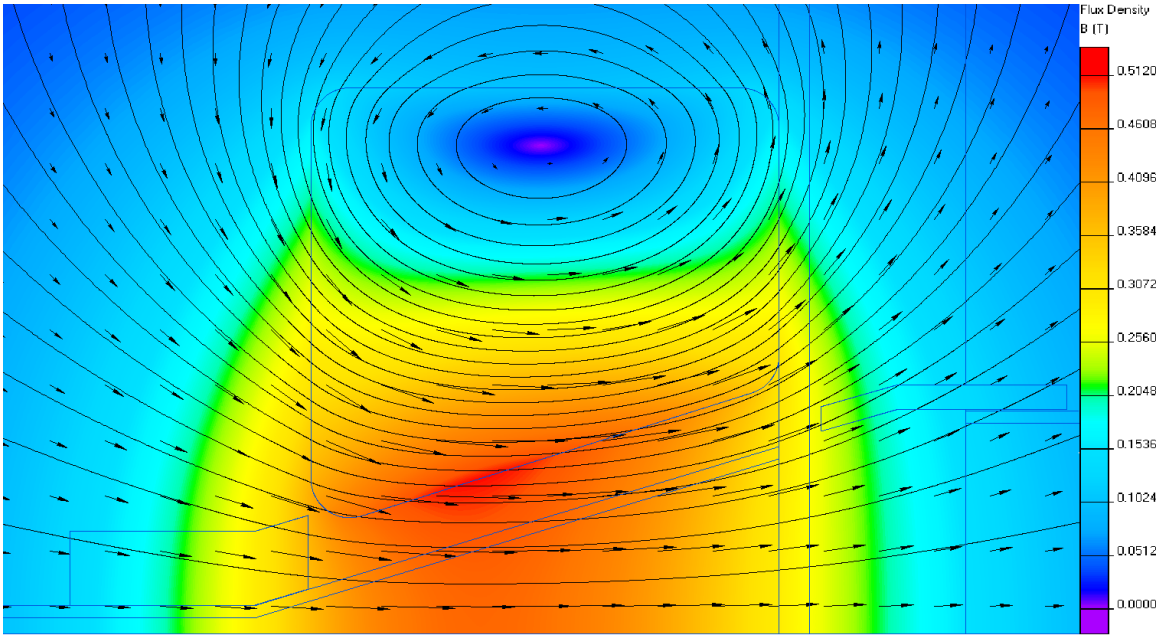


**Figure B.1**: Simulation of proposed pulsed, external bias field setup: DC with only the main coil active. [(50000 A) in the magnetostatic case. The maximal field strength was given by QuickField™ to be 0.512 T in this setup.]

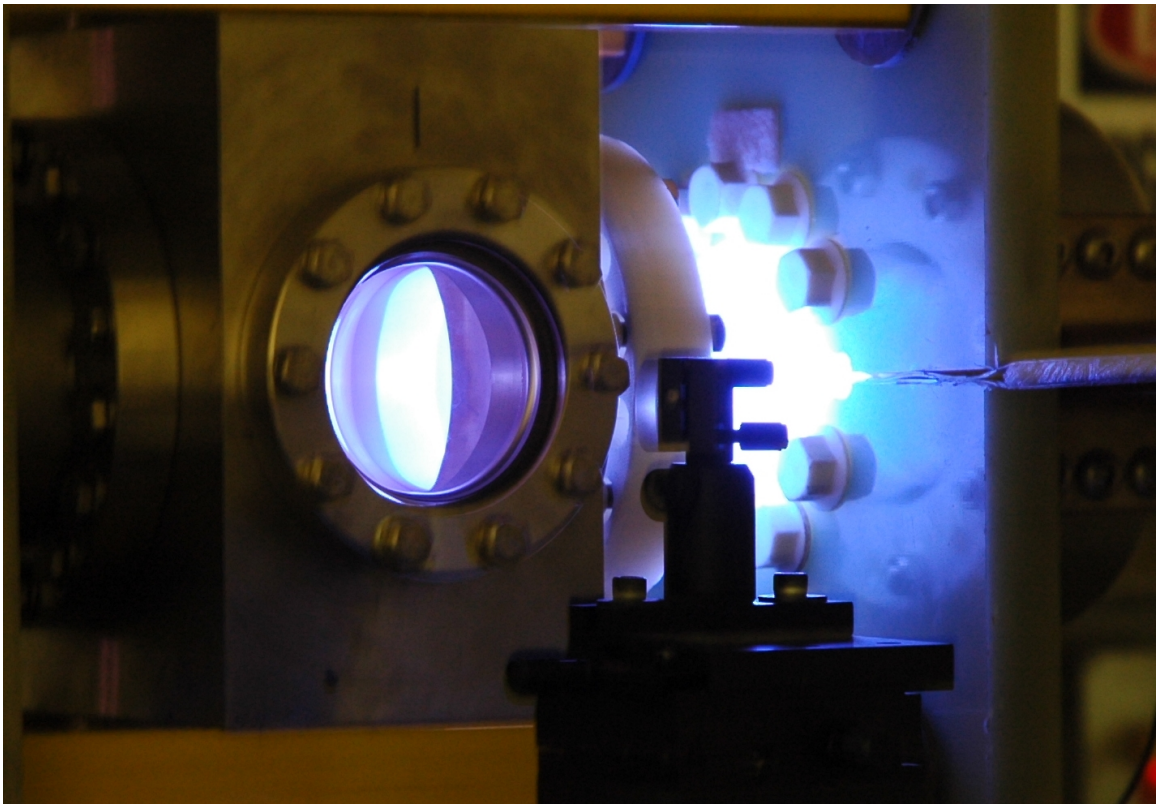

**Figure B.2**: A photograph of a plasma shot using Argon propellant. [Note that it is not possible to determine if a plasmoid was formed or if this was just a plasma shot based on this photo alone.]

## REFERENCES


[1] Peter Fimognari. *A Magnetic and Interferometric Study of a Plasma Formed in a Conical-Theta Pinch*. PhD Dissertation, UAHuntsville, 2007.

[2] E.Y. Choueiri. A critical history of electric propulsion: The first 50 years (1906 - 1956). *Journal of Propulsion and Power*, 20(2):193–203, 2004.

[3] Robert G. Jahn. *Physics of Electric Propulsion*. McGraw-Hill Series in Missile and Space Technology, 1968.

[4] Alexey V. Arefiev and Boris N. Breizman. Theoretical components of the VASIMR plasma propulsion concept. *Physics of Plasmas*, 11(5):2942–29–49, 2004.

[5] Jeff D. Filliben. Electric propulsion for spacecraft applications. Technical Report CPTR 96-64, The Johns Hopkins University, December 1996.

[6] Jeff D. Filliben. Electric thruster systems. Technical Report CPTR 97-65, Chemical Propulsion Information Agency, June 1997.

[7] Robert G. Jahn and Edgar Y. Choueiri. Electric propulsion. In *Encyclopedia of Physical Science and Technology*, volume 5, pages 125–141. Academic Press, 3rd edition, 2002.

[8] Smirnov A. Raitses Y. and Fisch N.J. Cylindrical hall thrusters. In *37th AIAA Plasmadynamics and Lasers Conference*, 2006.

[9] E.Y. Choueiri and J.K. Ziemer. Quasi-steady magnetoplasmadynamic thruster performance database. *Journal of Propulsion and Power*, 17(4):520–529, 2001.

[10] Thomas E. Markusic, Y. C. Francis Thio, and Jason T. Cassibry. Design of a high-energy, two-stage pulsed plasma thruster. In *38th AIAA Joint Propulsion Conference*, Indianapolis, Indiana, 2002.

[11] Jeremy H. Corpening and Ivana Hrbud. Preliminary design and analysis of the Purdue University pulsed inductive thruster or pupit, July 9-12 2006.

[12] Adam Martin and Richard Eskridge. Electrical coupling efficiency of inductive plasma accelerators. *Journal of Physics D: Applied Physics*, 38:4168–4179, 2005.

[13] Thomas L. Owens. A pulsed-compression-ring circuit for high-efficiency electric propulsion. *Rev. Sci. Instrum.*, 79(3), 2008.

[14] J. T. Cassibry. Comparison of directly and inductively coupled pulsed electromagnetic thrusters. *IEEE Transactions on Plasma Science*, 36(5):2180 – 2188, 2008.

[15] R. H. Lovberg and C.L. Dailey. Large inductive thruster performance measurement. *AIAA Journal*, 20(7):971–977, 1981.

[16] R.H. Lovberg and C.L. Dailey. Pit mark v design. In *Conference on Advanced SEI Technologies*, Cleveland, Ohio, 1991.

[17] E.Y. Choueiri and Kurt A. Polzin. Faraday acceleration with radio-frequency assisted discharge (FARAD). In *40th AIAA/ASME/SAE/ASEE Joint Propulsion Conference and Exhibit*, Fort Lauderdale, Florida, 2004. AIAA.

[18] E.Y. Choueiri and Kurt A. Polzin. Faraday acceleration with radio-frequency assisted discharge. *Journal of Propulsion and Power*, 22(3):611–619, 2006.

[19] J. T. Slough. Multi-megawatt propulsion based on a compact toroid thruster. In *International Electric Propulsion Conference*, Princeton, New Jersey, 2005.

[20] J. T. Slough and George Votroubek. Magnetically Accelerated Plasmoid (map) Propulsion. In *42nd AIAA/ASME/SAE/ASEE Joint Propulsion Conference and Exhibit*, Sacramento, California, 2006.

[21] M. Tuszewski. Field reversed configurations. *Nuclear Fusion*, 28(11):2033 – 2092, 1988.

[22] Richard D. Milroy. Reconnection during the formation of field reversed configurations. *Washington DC American Geophysical Union Geophysical Monograph Series*, 1984.

[23] David Kirtley, Daniel L. Brown, and Alec D. Gallimore. Details on an annular field reversed configuration plasma device for spacecraft propulsion. In *International Electric Propulsion Conference*, pages 1–9, Princeton, New Jersey, 2005.

[24] K. A. Polzin. Scaling and systems considerations in pulsed inductive plasma thrusters. *IEEE Transactions on Plasma Science*, 36(5):2189 – 2198, 2008.

[25] R. Bruce Pittman and Paul M. Koloc. The Plasmak solution: The answer for space power and propulsion. *Proceedings of the 24th Intersociety: Energy Conversion Engineering Conference*, pages 501–505, 1989.

[26] A. B. Kukushkin and V. A. Rantsev-Kartinov. On the plasma-focus-produced spheromak for the d-3he-fusion-based jet propulsion. In *Proceedings of the 1995 16th IEEE/NPSS Symposium on Fusion Engineering*, volume 2, pages 1490–1493, Champaign, Illinois, 1995. IEEE.

[27] T. Carter, M. Yamada, H. Ji, S. Hsu, R. Kulsrud, H. Himura, and S. Zaharia. Studies of magnetic reconnection in a laboratory plasma, June 1-4 1998.

[28] Y.C.F. Thio, E. Panarella, R.C. Kirpatrick, C.E. Knapp, and F.J. Yysocki. Magnetized target fusion in a spheroidal geometry with standoff drivers, 1999.

[29] X. Wang, A. Bhattacharjee, and Z.W. Ma. Scaling of collisionless forced reconnection. *Physical Review Letters*, 87(26), 2001.

[30] John Slough. Pulsed high density fusion, February 25-27 2002.

[31] B. W. Stallard, E.B. Hooper, S. Woodruff, R. H. Bulmer, D. N. Hill, H. S. McLean, R. D. Wood, and SSPX Team. Magnetic helicity balance in the sustained spheromak plasma experiment. *Physics of Plasmas*, 10(7):2912–2924, 2003.

[32] B. A. Nelson, T.R. Jarboe, W. T. Hamp, V. A. Izzo, R. G. O'Neill, A. J. Redd, P. E. Sieck, R. J. Smith, G. L. Sutphin, and J. S. Wrobel. Overview of the helicity injected torus program. *IEEE Transactions on Plasma Science*, 2005.

[33] J. T. Cassibry and R. J. Cortez. Sizing of plasma driven magnetoinertial fusion systems using a self-similar converging shock model, 2008.

[34] Ian J. E. Jordan. Electric propulsion: Which one for my spacecraft?, December 6 2000.

[35] Ivana Hrbud. Alternate direct-drive option for electric propulsion. *Journal of Propulsion and Power*, 23(4):845–853, 2007.

[36] H. Bostick Winston and R. Wells Daniel. Azimuthal magnetic field in the conical theta pinch, 1963.

[37] R. Wells Daniel. Observation of plasma vortex rings, 1962.

[38] E. A. Valsamakis, R. L. Small, and W. H. Bostick. Magnetic field probe measurements of plasma inside a conical theta-pinch, September 11-13 1967.

[39] E. A. Valsamakis, R. L. Small, and W. H. Bostick. Observation of plasma vortices and their magnetic fields inside a conical theta-pinch. *Technical Notes*, pages 1161–1163, 1968.

[40] R. H. Lovberg and C. L. Dailey. A pit primer. *Technical Report 005, RLD Associates*, 1994.

[41] Pavlos G. Mikellides, Nalin Ratnayake, and Brian England. Modeling of plasma thrusters, 2006.

[42] Jeremy H. Corpening, Ding Li, Ivana Hrbud, and Charles Merkle. Computational analysis of a pulsed inductive thruster, July 8-11 2007.

[43] Pavlos G. Mikellides and Chris Neilly. Modeling and performance analysis of the pulsed inductvie thruster. *Journal of Propulsion and Power*, 23(1):51–58, 2007.

[44] Pavlos G. Mikellides and Nalin Ratnayake. Modeling of the pulsed inductive thruster operating with ammonia propellant. *Journal of Propulsion and Power*, 23(4):854–862, 2007.

[45] K. A. Polzin and E. Y. Choueiri. Design rules for high-performance FARAD thrusters, October 31-November 4 2005.

[46] K. A. Polzin and E. Y. Choueiri. Performance optimization criteria for pulsed inductive plasma acceleration. *IEEE Transactions on Plasma Science*, 34(3):945 – 953, 2006.

[47] C.L. Dailey and R. H. Lovberg. Large diameter inductive plasma thrusters, October 30-November 1 1979.

[48] A. L. Hoffman and J. T. Slough. Inductive field-reversed configuration accelerator for tokamak fueling. *IEEE Transactions on Plasma Science*, 22(6), 1999.

[49] J. W. Mather. Investigation of the high-energy acceleration mode in the coaxial gun. *The Physics of Fluids Supplement*, 7(11):S28–S34, 1964.

[50] D. R. Wells, J. Davidson, L. G. Phadke, J. G. Hirschberg, P. E. Ziajka, and J. Tunstall. High-temperature, high-density plasma production by vortex-ring compression. *Physical Review Letters*, 41(3):166, 1978. Copyright (C) 2008 The American Physical Society Please report any problems to prola@aps.org PRL.

[51] J. T. Cassibry and S. T. Wu. Comparison of directly and inductively coupled pulsed electromagnetic thrusters. In *36th AIAA Plasmadynamics and Lasers Conference*, Toronto, Ontario, Canada, 2005.

[52] Robert C. Weast. *CRC Handbook of Chemistry and Physics*. CRC Press, Cleveland, Ohio, 56th edition, 1976.

[53] David M. Harrison. Mach-Zehnder interferometer, August 17 2005. www.upscale.toronto.edu/GeneralInterest/Harrison/MachZehnder/MachZehnder.html.

[54] Daniel Mader. Illustration of a classic Mach-Zehnder interferometry setup, 2005. Graphics taken with permission from the "Wikimedia Commons" a freely licensed media file repository. The image is covered by the GNU Free Documentation License which grants permission for reuse in printed media. http://en.wikipedia.org/wiki/Image:Mach-zender-interferometer.png.

[55] C. J. Buchenauer and A. R. Jacobson. Quadrature interferometer for plasma density measurements. *Review of Scientific Instruments*, 48(7):769–774, 1977.

[56] F. Darde. Picture of an Acousto-Optic Modulator, used with permission, 2008. Used with permission given by Franck Darde, Sales & Marketing Director in personal communication. Image located at www.acoustooptic.com/constitution-bragg-cell.html.

[57] AA-Opto-Electronic. Basic principles of acousto-optic theory, on which acousto-optic devices are based on, 2008. http://www.acoustooptic.com/index.html.

[58] A. R. Jacobson. Heterodyne quadrature interferometer for simultaneous measurements of plasma density along several chords. *Review of Scientific Instruments*, 49(5):673–674, 1978.

[59] B. V. Weber and D. D. Hinshelwood. He–ne interferometer for density measurements in plasma opening switch experiments. *Review of Scientific Instruments*, 63(10):5199–5201, 1992.

[60] Coherence™. Indigo DUV technical specifications and data sheet, 2008. www.coherent.com/downloads/Indigo_DUV.pdf#page=1.

[61] D. Kumar and P. M. Bellan. Heterodyne interferometery with unequal path lengths. *Review of Scientific Instruments*, 77, 2006.

[62] M. Taylor. The Appleton-Hartree formula and dispersion curves for the propagation of electromagnetic waves through an ionized medium in the presence of an external magnetic field. *Proceedings of the Physical Society*, 46:245–264, 1933.

[63] Victor V. Nosov. Refractive index of any gaseous mixtures in Lorentz-Lorenz spectroscopy. *13th Symposium and School on High-Resolution Molecular Spectroscopy*, 4063(1):79–89, 2000.

[64] D. E. Diller. Refractive index of gaseous and liquid hydrogen. *Journal of Chemical Physics*, 49(7):3096–3105, 1968.

[65] B. V. Weber and S. F. Fulghum. A high sensitivity two-color interferometer for pulsed power plasmas. *Review of Scientific Instruments*, 68(2):1227–1232, 1997.

[66] William Nagel. Pearson Electronics INC Bias notes, August 14 2002.

[67] I.H. Hutchinson. *Principles of Plasma Diagnostics*. Cambridge University Press, New York, 1987.

[68] Syri Koelfgen. *Magnetic Field and Quadruple Langmuir Probe Measurements in the Plume of the Plasmoid Thruster Experiment*. PhD Dissertation, UAHuntsville, 2005.

[69] Richard H. Eskridge, Peter J. Fimognari, Adam K. Martin, and Michael H. Lee. Design and construction of the PT-1 prototype plasmoid thruster. In Mohamed S. El-Genk, editor, *Space Technology and Applications International Forum (STAIF-2006)*, volume 813, pages 474–483. AIP, 2006.